CHALLENGES IN TWO-FLUID MODELING APPLIED TO LARGE-SCALE BUBBLE PLUMES

by

Anna Haley

Submitted in partial fulfillment of the requirements
for the degree of Master of Applied Science

at

Dalhousie University
Halifax, Nova Scotia
August 2017

© Copyright by Anna Haley, 2017

For Lora Buttercup

Table of Contents

List of Tables

List of Figures

Abstract

Large-scale bubble plumes of sour gas from underwater wells pose many environmental health and safety concerns. The prediction of the physical extent of the release and the amount of dissolution into the surrounding ocean water is important for emergency preparedness planning. The two-fluid model has been used in multiphase applications for bubbly flow, and could be applicable for modeling scenarios such as the plume region of an underwater gas well blowout.

A customized two-fluid model was implemented in `OpenFOAM` to account for mass transfer processes. Two separate hydrodynamic studies were performed. It was concluded that the model is likely only applicable in scenarios where the parameters of the model can be tuned to experimental data. Extrapolation of a tuned model to significantly different geometries, larger scales, or more complicated scenarios could pose significant challenges.

List of Abbreviations and Symbols Used

	Latin Characters	Units
A_i	Interfacial Bubble Area	$[m^2]$
a_i	Interfacial Area Concentration	$[m^{-1}]$
c_p	Specific Heat Capacity	$[J/(kg \cdot K)]$
d	Bubble Diameter	[m]
$D_{i,j}$	Diffusion Coefficient	$[m^2/s]$
g	Acceleration due to Gravity	$[m/s^2]$
he	Internal Energy/Enthalpy	[J/kg]
H	Henry's Law Coefficient	[−]
H	Specific Enthalpy	[J/kg]
I	Identity tensor	
k	Turbulent Kinetic Energy	$[m^2/s^2]$
k	Flux Limiter Coefficient	[-]
k_m	Volumetric Mass Transfer Coefficient	$[s^{-1}]$
k_h	Volumetric Heat Transfer Coefficient	$[kg/(m \cdot s^2 \cdot K)]$
K	Kinetic Energy	[J/kg]
L	Characteristic Length	[m]
m	Mass	[kg]
P	Pressure	[Pa]
P_{rgh}	Modified Pressure	[Pa]
$\dot{Q}$	Heat Flux	$[J/(s \cdot m^2)]$
r_d	Bubble Radius	[m]
r	Ratio between Upwind and Downwind Gradients	[-]
R	Stress Rate Tensor	$[N/(m^2 \cdot s)]$
s	Hyperbolic Blending Scale Factor	[−]
$\overline{S}$	Compressible Mean Rate of Strain	[m/m/s]
S_f	Face Area Vector	$[m^2]$
Su	Explicit Source Term	varies
Sp	Implicit Source Term	varies
T	Temperature	[K]
$\vec{U}$	Velocity	[m/s]
V_b	Bubble Volume	$[m^3]$
V	Volume	$[m^3]$
X	Liquid Phase Mass Fraction	$[kg_{species}/kg_{gas}]$
Y	Gas Phase Mass Fraction	$[kg_{species}/kg_{gas}]$

	Greek Characters	Units
α	Phase (Volume) Fraction	$[m^3_{phase}/m^3_{total}]$
Δ	Grid-scale Filter Width	[m]
ϵ	Eddy Dissipation Rate	$[m^2/s^3]$
λ	Mean Free Path	[m]
μ	Dynamic Viscosity	$[Pa \cdot s]$
ν	Kinematic Viscosity	$[m^2/(s)]$
$\vec{\phi}$	Face-flux	$[m^3/s]$
$\overrightarrow{\phi(r)}$	TVD Limiter Function	[-]
ψ	Compressibility	$[kg/(m^2 \cdot Pa)]$
Ψ	Sphericity	$[-]$
κ	Interfacial Curvature	$[m^{-1}]$
ρ	Density	$[kg_{phase}/m^3_{phase}]$
σ	Surface Tension	[N/m]
	Dimensionless Numbers	
Bo	Bond Number	
Eo	Eötvös Number	
Ga	Galilei Number	
Kn	Knudsen Number	
Le	Lewis Number	
M	Morton Number	
Pe	Péclet Number	
Pr	Prandtl Number	
Re	Reynolds Number	
Sh	Sherwood Number	
Sc	Schmidt Number	
We	Weber Number	
	Subscripts	
c	Continuous Phase Property	
cr	Critical Property	
d	Dispersed Phase Property	
g	Gas Phase Property	
i	Phase or Species Property	
l	Liquid Phase Property	
r	Relative Property	
t	Turbulent Property	

Superscripts	
I	Interfacial Property
eff	Effective Property
t	Thermal Property, or Time

Abbreviations	
BIT	Bubble Induced Turbulence
CDOG	Comprehensive Deepwater Oil and Gas blowout model
CFD	Computational Fluid Dynamics
CM	Class Method
COMBOS3D	Complete Model for Blow-Out Simulations in 3-Dimensions
DIC	Diagonal-based Incomplete Cholesky
DPM	Discrete Particle Method
DQMOM	Direct Quadrature Method of Moments
FVM	Finite Volume Method
GAMG	Geometric-Algebraic Multi-Grid
IATE	Interfacial Area Transport Equation
JETLAG	Jet Lagrangian Integral Model
LES	Large Eddy Simulation
MOM	Method of Moments
MULES	Multi-dimensional Universal Limited Explicit Solver
OpenFOAM	Open-source Field Operation And Manipulation
PIMPLE	Pressure Implicit Method for Pressure-Linked Equations
PISO	Pressure Implicit Method with the Splitting of Operators
RANS	Reynolds Averaged Navier Stokes
RSTE	Reynolds Stress Transport Equation
SGS	Sub-Grid Scale
SIMPLER	Semi-Implicit Method for Pressure-Linked Equations-Revised
TVD	Total-Variation Diminishing

Acknowledgements

I would like to begin by acknowledging my supervisor, Dr. Jan Haelssig, who provided guidance and support throughout this degree. I would also like to thank my colleague Devin O'Malley, who always made himself available to answer my questions about `OpenFOAM`.

I am indebted to Julie O'Grady, Paula Colicchio, and Diana Orsini in the PEAS office for going out of their way on numerous occasions to help me with administrative matters.

My committee members Dr. Adam Donaldson and Dr. Darrel Doman were very helpful in their suggestions for keeping the focus of this thesis in check. Dr. Stephen Kuzak has been an enduring friend, and has helped me on numerous occasions by writing very effective letters of reference.

I would like to recognize ACENET for providing me with necessary computing resources. The financial support provided by NSERC, Encana Corporation, and Stantec Consulting Inc. is also gratefully acknowledged. The funding from the Dr. Robert Gillespie prize and the Nova Scotia Graduate Scholarship also contributed significantly to my happiness throughout this degree.

Finally, my husband Neil has been a total gem for the last few months and deserves an honorable mention.

Chapter 1

Introduction

The offshore oil and gas industry continues to improve its environmental and safety procedures. A common industry technique used to replace flaring and venting of waste gas streams is reinjection of the unwanted gas back into the reservoir. This practice serves to reduce greenhouse gas emissions while maintaining pressure in the reservoir. In order to plan for the safety of the workers and the environment, numerical modeling has been used to aid in the prediction of the surface concentration and extent of the gas, if an accidental release were to occur.

The waste gas is typically composed of hydrogen sulfide (H_2S) and carbon dioxide (CO_2), called "sour gas", which is highly toxic. H_2S can cause headaches and airway problems at low concentrations, olfactory paralysis at or above 100 ppm, and death in humans beyond 700 ppm. It is also potentially lethal to fish and other aquatic animals when dissolved into water at all concentrations (Chou, 2003).

In the event of a loss of containment, it is desirable to be able to predict the magnitude and extent of the gas release in order to assess the appropriate emergency response plan. An underwater well blowout can release a large quantity of gas very quickly due to the high pressure within the well, but the exact amount and its behaviour over time is unknown. Data from past blowouts is not available for analysis and, even if it were, could not necessarily be used to inform detailed predictive models directly.

To attempt to characterize this type of scenario, numerical modeling has been used. Generally, numerical models of underwater gas releases can be divided into three major categories: cone models, integral models, and computational fluid dynamics (CFD) models (Olsen and Skjetne, 2016a; Sridher, 2012).

Cone models are the simplest to implement, but are the most empirical and can therefore be the least valid. The simplest cone models rely on an assumed cone angle, from which average values of gas dissolution can be obtained. This has the potential to be an oversimplification of gas-jet dynamics because many important characteristics, such as bubble size and local velocity fluctuations, have an impact on the rate and magnitude of the dissolution as well as mixing and jet breakup.

Integral models are capable of capturing more of the flow characteristics. They have been written in both the Eulerian (stationary) and Lagrangian (moving) reference frames. Models which have been used in underwater gas blowout applications include DeepBlow (Johansen, 2000, 2003), CDOG (Yapa and Li, 1997), COMBOS3D (Yapa et al., 1999), JETLAG (Lee and Cheung, 1990), VDROP-J (Zhao et al., 2016), and others. Their main limitations are the empirical parameters they must incorporate, such as for the prediction of entrainment. An assumption must also be made about the location of the transition from pressure-driven to buoyancy-driven flow. These assumptions have been discussed by Dasanayaka and Yapa (2009), who determined that the empirical tuning can have a major impact on model predictions under varying conditions.

CFD models use fewer empirical tuning parameters, and should be able to more accurately predict the hydrodynamic behaviour of a jet or plume. Modeling of gas well blowouts using CFD is not currently as common in the literature, but it has been done by several groups in recent years (Olsen and Skjetne, 2016b; Pan et al., 2014; Socolofsky et al., 2016).

1.1 Finite Volume CFD

Solids, liquids and gases are typically considered to be continuua. In other words, they are treated as macroscopic materials in lieu of a collection of sub-atomic particles. Statistical mechanics can be used to describe the microscopic behaviour of nuclei and particles, while continuum mechanics is applied to describe the behaviour of all macroscopic materials. The applicability of either method is determined by the Knudsen number,

$$Kn = \frac{\lambda}{L} = \begin{cases} << 1, & \text{Mechanics of Continua} \\ >> 1, & \text{Statistical Mechanics} \end{cases} \tag{1.1}$$

Where λ is the mean free path of the particle, and L is the characteristic length-scale of the material.

Partial differential equations which capture mass, momentum, and energy conservation are used in continuum mechanics to find intrinsic and extrinsic properties of materials, such as mass, temperature and pressure, as well as mechanical properties such as displacement and momentum. Analytical solutions for the equations have not been found without major assumptions. Obtaining the true field of each property

would require the solution of the equations at all points in space and time. Since this is not possible without an analytical solution, computational methods break the domain up into discrete locations in space and time in order to obtain a system of algebraic equations, which can be solved to approximate the properties at those locations (LeVeque, 2002).

The finite volume method is the most commonly used numerical technique in computational fluid dynamics. The spatial discretization divides the domain up into finite regions defined by a mesh, referred to as control volumes or cells. If the solution will change with time, the time domain can also be divided into intervals, called time-steps. The solution of the properties, functions of space and time, can then be determined based on a relationship between the properties at neighbouring cells and previous times at each point.

There are several discretization methods available for the solution of the partial differential fluid transport equations. An example would be the simple case of the 1-D scalar transport equation of some property $f = f(x,t)$. The equation is,

$$\underbrace{\frac{\partial f}{\partial t}}_{\text{time dependance}} + \underbrace{\frac{\partial f\vec{U}}{dx}}_{\text{advection}} - \underbrace{\frac{d}{dx}\left(\Gamma\frac{\partial f}{\partial x}\right)}_{\text{diffusion}} = S \tag{1.2}$$

Where $\vec{U}$ is the velocity, Γ is a diffusion coefficient, and $S = g(f,x,t)$ are any source terms of the equation.

The equation is second-order in space and first-order in time. To maintain accuracy the spatial and temporal discretizations must be of the same order or above (Jasak, 1996). The mesh is usually taken to be a fixed size based in a cartesian coordinate system, but this is no longer universally the case with the increasing number of studies with adaptive mesh refinement and/or moving meshes.

To discretize the equation, a volume average of each property is taken over each control volume, which can then be stored at the cell centre of the current cell (P). The volume average usually assumes a linear profile between the edge property values which are found with the interpolation of the cell centre values. Higher order property profiles can also be selected. A 1-D mesh is given for reference in Figure 1.1.

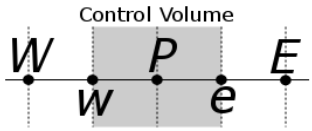

Figure 1.1: A 1-D finite volume mesh. The labels indicated the neighbouring points at the cell centres (uppercase) and the cell surfaces (lowercase).

Integrating equation 1.2 over a control volume gives,

$$\iiint_V \frac{\partial f}{\partial t} dV + \iiint_V \frac{\partial f \vec{U}}{dx} dV - \iiint_V \frac{d}{dx}\left(\Gamma \frac{\partial f}{\partial x}\right) dV = \iiint_V S dV \tag{1.3}$$

Which reduces to,

$$\int_x \frac{\partial f}{\partial t} \not{A} dx + \int_x \frac{\partial f \vec{U}}{dx} \not{A} dx - \int_x \frac{d}{dx}\left(\Gamma \frac{\partial f}{\partial x}\right) \not{A} dx = \int_x S \not{A} dx \tag{1.4}$$

The integration of the advection term involves the application of Gauss's theorem, which states that the volume integration of the divergence of a quantity (e.g. $\vec{F}$) is related to the flux across its boundary by,

$$\iiint_V \nabla \cdot \vec{F} dV = \oiint_S \vec{F} \cdot \hat{n} dS \tag{1.5}$$

Which can be applied to the advection term across the control volume in 1-D as,

$$\int_x \frac{\overrightarrow{dF}}{dx} dx = \sum_{faces} \vec{F}_{face} \cdot \hat{n} = \overrightarrow{F_e} - \overrightarrow{F_w} \tag{1.6}$$

The fluxes $\overrightarrow{F_e}$ and $\overrightarrow{F_w}$ can be approximated as the average between cell centre values. Both the velocity and the property values at the face would then be taken as the average between cell centre values. The diffusion term is integrated over the control volume similarly to the advection term, where

$$\vec{F} = \Gamma \frac{\partial f}{\partial x} = \Gamma \frac{\Delta f}{\Delta x} \tag{1.7}$$

A second order spatial discretization of the 1-D advection-diffusion equation on the

mesh is,

$$\frac{\partial f}{\partial t} = \frac{-1}{\Delta x}\left[\left[\frac{U_E f_E + U_P f_P}{2} - \frac{U_P f_P + U_W f_W}{2}\right] - \left[\Gamma_e \frac{f_E - f_P}{x_E - x_P} - \Gamma_w \frac{f_P - f_W}{x_P - x_W}\right] - S_{avg}\Delta x\right] \tag{1.8}$$

The spatial discretization of the advection term can incorporate the characteristics of the flow, for instance if the flow is primarily in one direction, an upwind scheme could be used in lieu of the symmetric scheme shown. The upwind-weighted schemes determine the direction of the flow using an upwind factor, and weight the value of the upstream property more heavily than the downstream. The incorporation of both schemes with a weighting factor which allows for one or the other scheme to be preferentially applied is the basis for the total variation diminishing (TVD) schemes.

The mesh arrangement can be staggered or co-located (Figure 1.2), which can have a major impact on the solution. In the co-located arrangement, all property values are stored at the cell center. In the staggered arrangement, the scalar properties (temperature, pressure, etc.) are stored at the cell centers, while the velocity is stored at the cell faces. This arrangement prevents "checkerboarding" of the pressure, as described in Patankar (1980). Keeping track of the variables and their locations in a staggered grid arrangement can be more difficult in practice, however. As a result, most finite volume codes employ the co-located arrangement along with interpolation methods that avoid the checkerboarding issue.

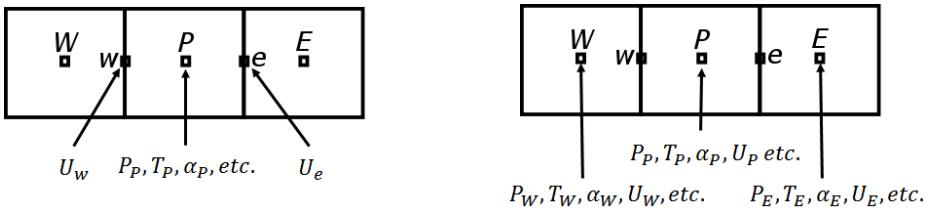

Figure 1.2: Staggered (left) and co-located (right) grid arrangements.

The time dependence is often dealt with by using either implicit (backward) or explicit (forward) Euler's method, but higher order schemes can also be used. Applying the forward Euler scheme gives the new value of the property $(t + \Delta t)$ at point P,

$$f_P^{t+\Delta t} = f_P^t - \frac{\Delta t}{\Delta x}\left[\left[U_e \frac{f_E + f_P}{2} - U_w \frac{f_P + f_W}{2}\right] - \left[\Gamma_e \frac{f_E - f_P}{x_E - x_P} - \Gamma_w \frac{f_P - f_W}{x_P - x_W}\right] - S_{avg}\Delta x\right]^t \tag{1.9}$$

The equations for mass, momentum and energy must always be closed; the linear relationship must be based on values of the property itself and its derivatives at different points in space and previous times, or other known quantities. If it is not closed, the system is underdetermined and cannot be solved.

To close the equations, most finite volume algorithms solve the equations in a segregated manner. In other words, the momentum, energy, and continuity equations are solved sequentially because the properties all rely on each other (Jasak, 1996). The equations are solved one after another with initial and boundary conditions, and their solutions are used as the new conditions for the next iteration. Once the solutions to the equations no longer change (to some pre-determined tolerance), the solution of each property in the domain at that time is considered to have been found. For transient simulations, the equations would then advance to the next time-step. Coupled solvers, which solve all the equations simultaneously, are also commonly used for a solution which is ostensibly more stable. In this thesis, a segregated finite volume method was used.

1.2 Two-phase CFD Modeling of Underwater Gas Well Blowouts

An underwater gas well blowout would usually result in the release of what is often a gas-liquid mixture into the underwater environment. For the purposes of this research, it is assumed that the inlet fluid would be pure gas. Initially the release is likely driven by the rapid expansion from a highly pressurized pipe into the relatively low pressure of the surrounding water. This highly transient behaviour is expected to be short-lived before reaching pseudo-steady state. Bubble breakup would probably occur immediately as the gas moves upward, eventually reducing the gas to smaller dispersed bubbles.

After the bubbles have reached a certain height, the pressure gradient may no longer be the dominant driving force, and buoyancy may take precedence. If so, the bubbles would slow down to their terminal velocity because of the drag force and dissolve more quickly into the surrounding water due to their increased area-to-volume ratio, increased residence time, and exposure of the gas bubbles to areas with low dissolved gas concentrations. Close to the surface of the ocean, surface conditions would determine the behaviour of the gas.

In general, underwater releases have been characterized by three distinct regions, as shown in Figure 1.3. Near the inlet, the jet region contains large gas bubbles with well-defined gas-liquid interfaces. In this region, CFD models that track the bubble

interface, such as the Volume of Fluid (VOF) methodology, are optimal for predicting the gas behaviour. The VOF method is one of the most commonly used interface tracking algorithms. It uses an Eulerian reference frame and solves a continuity equation in one of the phases to capture interface movement. The primary limitation to the model is that it is computationally intensive because it requires very small mesh cells to accurately resolve the interface. As the bubbles break up and increase in number, the interface prediction will break down.

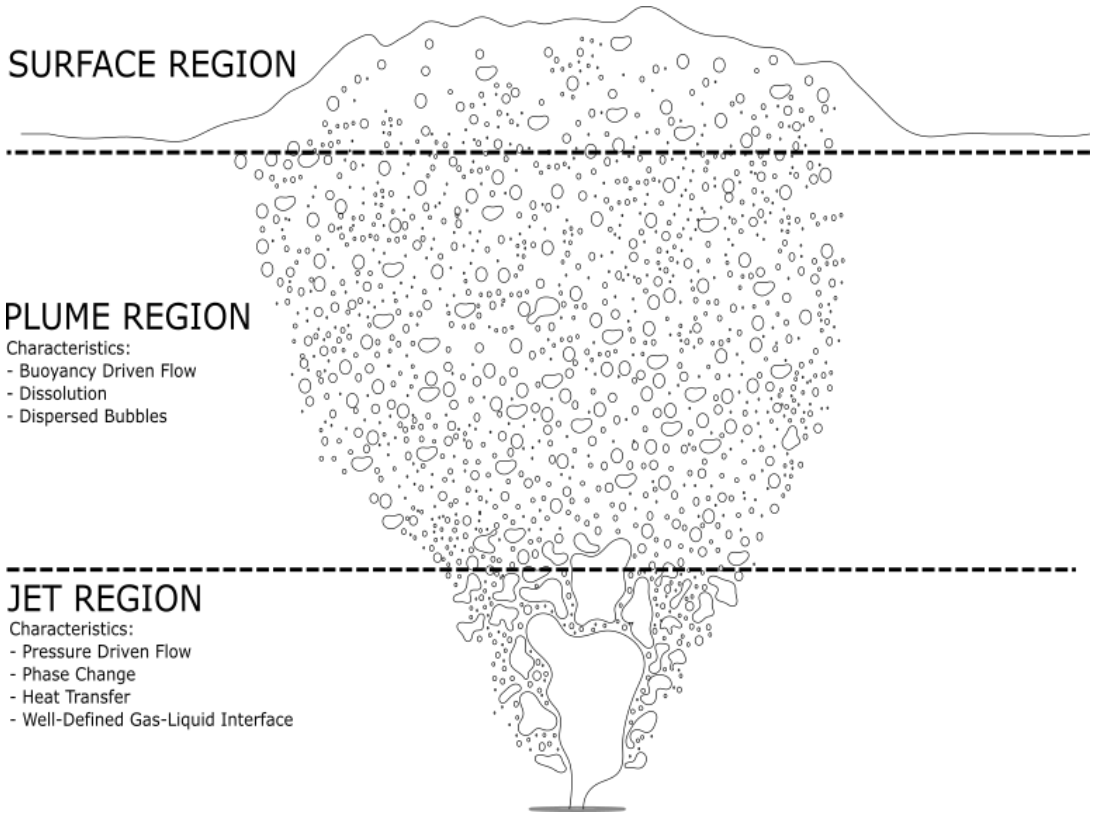

Figure 1.3: The three regions of an underwater gas release.

The plume region is where dispersed phase models, for instance the popular Euler-Euler or Euler-Lagrange models, are likely to be more accurate. In this region, the flow transforms from pressure-driven to buoyancy-driven, and bubbles reach their terminal velocities. The Euler-Lagrange models, also called discrete phase models (DPMs), track the movement each bubble or parcel of bubbles with a Lagrangian reference frame, while the liquid is modeled in the Eulerian frame. Breakup and coalescence models determine the bubble size and frequency. DPMs can be built such that the continuous phase impacts the bubbles, but not the other way around (one-way coupling), or they can be built such that both phases can impact each other

(two- or multi-way coupling). The main downside to the model is that as the number of bubbles in the domain increases, tracking each bubble or parcel can become more computationally expensive.

The Euler-Euler, or two-fluid, model solves for both gas and liquid phases from Eulerian reference frames. The phases are treated as inter-penetrating continuua using force terms to couple phase-averaged momentum equations. The gas present in each cell of the mesh is represented by the volume, or phase, fraction. It is then solved for with a continuity equation to identify the location of the gas. This allows for a coarser mesh than the interface tracking method, while being less computationally expensive than the DPMs.

Assuming that the cell is a mixture of the two phases instead of discrete locations where the phase exists in the cell results in phase-averaging. The amount of the phase in the cell is represented by a phase fraction, α [m^3 phase/m^3 cell], which acts as a weighting factor. Since the properties are all calculated volumetrically due to the volume averaging, multiplication by the phase average results in the cell center values of the properties for that phase. Figure 1.4 shows how the phase-average is taken for the properties of each phase i in the Euler-Euler representation of a multiphase bubbly system: phase fraction, density, velocity, pressure, temperature, etc.

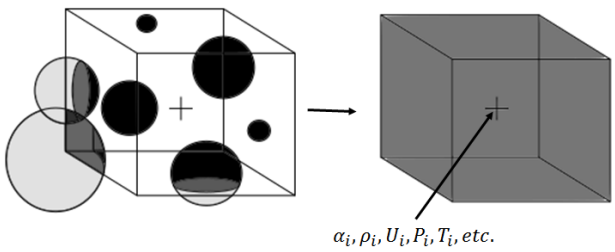

Figure 1.4: A representation of the phase-average for the properties stored at the cell centre.

At the moment, there is no single CFD model which can accurately incorporate the dramatically varying gas behaviour from the bottom to the top of the water column in the type of release scenario described. It is required, therefore, to use separate techniques for regions defined by the gas dynamics. A multi-model approach requires that the outlet conditions of the previous region are the inlet conditions to the next, which can involve certain complications. In this research, the focus is restricted to the plume region, and the techniques required to model it with the two-fluid model.

1.2.1 The Two-Fluid Modeling Approach

Two-fluid models are broadly applicable to the simulation of fluidized beds, bubble columns, and other complex two-phase flows. They are also less computationally expensive than many other modeling approaches when high phase fractions are present. These models solve the flow equations in both phases with the addition of interphase force terms.

The majority of the gas dissolution is expected to occur in the plume region, where the residence time is greatest, so a good prediction of the mass of CO_2 and H_2S transferred from the gas to the liquid is essential. For this to be possible, the hydrodynamics must be accurately represented. Bubble size has a direct influence on the magnitude of the interphase forces, as well as being important in the mass transfer prediction. For these reasons, the inclusion of a bubble size model is ultimately necessary to help prevent the over or underprediction of the dissolution. The turbulence prediction is also of great importance, because it is directly related to the lateral spreading of the plume via the turbulent dispersion force, the breakup processes which determine the bubble size, and the mass transfer, which is related to the size of the bubbles.

Since the two-fluid model only accounts for two phases, bubble size distributions must eventually be reduced to a single average size for use in the source terms of the momentum equations. To improve the prediction, additional phases could be incorporated in the model to account for bubbles of different size. This has been done with application of the inhomogeneous MUSIG (multiple size group) model Frank et al. (2005), in which multiple momentum equations are solved for different bubble size classes.

The lack of turbulence model development for the Euler-Euler models is one of its main limitations. Although there are many models which have been fitted to specific data sets, they are not necessarily broadly applicable. Often the models are tuned for bubble column simulations, which may not be applicable at all to other flow regimes. Confined and unconfined flow simulations can result in totally different conclusions for turbulence as well due to the effect of nearby walls. The ratio of bubble size to mesh size in confined flows has been established in the literature by Milelli et al. (2001b) for instance, but mesh effects in unconfined flow have not been.

The two-fluid model is also disadvantaged due to the number of sub-models it requires. Many of them are simplified in preference of computational speed or stability over accuracy. The amount of tuning for sub-model coefficients that is required can

be daunting, particularly of the drag, lift, and turbulent dispersion force coefficients. A slight alteration in one of the models could dramatically influence the whole simulation. The effects could only become more pronounced with addition of a bubble size model to an inappropriate suite of tuning parameters.

Euler-Euler models continue to be competitive against other models because the sub-models are relatively simple to implement, the simulations are comparatively faster than many other models, and the predictions are often very good if the models can be tuned to the particular flow conditions of the physical system. Extension of the sub-models to other modeling problems, such as unconfined plumes and gas well blowouts, is essential for exposing and remediating its current limitations. For the two-fluid models to dominate the landscape of dispersed flow simulations, more development in these areas is required.

The gas well blowout is a particularly challenging application due to the multi-scale nature of the bubble plume. The small bubbles in the plume impact and are impacted by the larger bubbles primarily through turbulent and wake interations, while the larger bubbles can significantly alter the dynamics of the continuous liquid phase. An appropriate mesh size to capture these interactions is unclear, and it isn't clear that any bubble size distribution model currently available would be capable of describing the interactions between bubbles on such as wide variation of scale. Due to the lack of available well blowout data, the tuning of sub-model coefficients on smaller-scale cases is required before application to the large-scale gas well blowout.

1.3 Objectives

This research is intended to evaluate a two-fluid modeling approach for two-phase computational fluid dynamics simulations of the plume region of an underwater gas blowout. The use of Euler-Euler models for this type of modeling is not ubiquitous in the literature, but they have the potential to become one of the dominant modeling approaches. An open-source software package for computational fluid dynamics, `OpenFOAM`, was used for this work.

The following objectives are met in this work:

- Comprehensive literature review of all sub-models for the two-fluid model
- Incorporation of mass transfer capability into the `twoPhaseEulerFoam` solver
- Study of applicable two-fluid turbulence models with the `twoPhaseEulerFoam` solver

- Implementation of the interfacial area transport equation (IATE) with the `twoPhaseEulerFoam` algorithm
- Verification that the mass transfer additions to the solver were working as expected on a 1-D case study and a 3-D case with fluid flow

1.4 Organization

Chapter 2 of this thesis will outline the model equations and algorithm of the two-fluid model in `OpenFOAM`, as well as the implementation of mass transfer into the code. Chapter 3 provides a review of the available interphase force, bubble size, and mass transfer models. Chapter 4 includes a study of the two-fluid turbulence models. Chapter 5 includes the study of the hydrodynamics of an unconfined flow case and IATE model for the bubble size. The mass transfer modeling of two separate cases, with and without flow, are included in Chapter 6. Conclusions about the `twoPhaseEulerFoam` solver and its applicability to scenarios such as the full-scale gas well blowout are presented in Chapter 7.

Chapter 2

Numerical Methodology

`OpenFOAM` is an open-source CFD software package which has been used throughout academic and industry literature to solve a variety of fluid dynamics problems. It includes a wide selection of solvers with differing solution procedures, several meshing utilities, and is packaged with popular thermophysical and turbulence models (OpenCFD Ltd., 2017). Of the multiphase solvers, the Euler-Euler model is represented by `twoPhaseEulerFoam` and `reactingTwoPhaseEulerFoam`. The latter has not been commonly cited in the literature and, in the cases of interest in this research, did not provide satisfactory results.

The `twoPhaseEulerFoam` solver has been validated over a range of cases in the literature which is why it has been adapted for this work. `OpenFOAM` version 3.0+ was used because it was the most recent version at the beginning of the project, but more recent versions are now available. New releases of the solver and utilities have not changed the numerical algorithm of `twoPhaseEulerFoam`, but some of the code implementation has been altered.

Details of an earlier, incompressible version of the `twoPhaseEulerFoam` algorithm have been described in Rusche (2002). Its PIMPLE (Pressure Implicit Method for Pressure-Linked Equations) algorithm linearizes the momentum equations for use in the pressure equation in the same style as the SIMPLER (Semi Implicit Method for Pressure-Linked Equations - Revised) algorithm (Patankar, 1980). It is also similar to the PISO (Pressure Implicit with the Splitting of Operators) algorithm of Issa (1985) in the coupling of pressure and velocity. PISO solves the momentum equations first and then updates the pressure with a separate equation. The `twoPhaseEulerFoam` solver splits the momentum equations as well, but does not solve them, instead solving the pressure equation based only on the linearization and iterating. Additional improvements to the stability of the solution procedure were also built into `twoPhaseEulerFoam`.

One of the downsides to the basic version of `twoPhaseEulerFoam` is that it cannot be used in cases where interphase mass transfer occurs. In `OpenFOAM`,

`reactingTwoPhaseEulerFoam` was meant to be used for this purpose, but as mentioned above, this solver did not provide adequate stability and accuracy for the cases investigated in this study. Therefore, in this work, a generalized mass transfer algorithm was added to the solution procedure of `twoPhaseEulerFoam`. This addition is discussed in detail in the following sections.

2.1 The `twoPhaseEulerFoam` Algorithm

The `twoPhaseEulerFoam` solution procedure is shown in Figure 2.1.

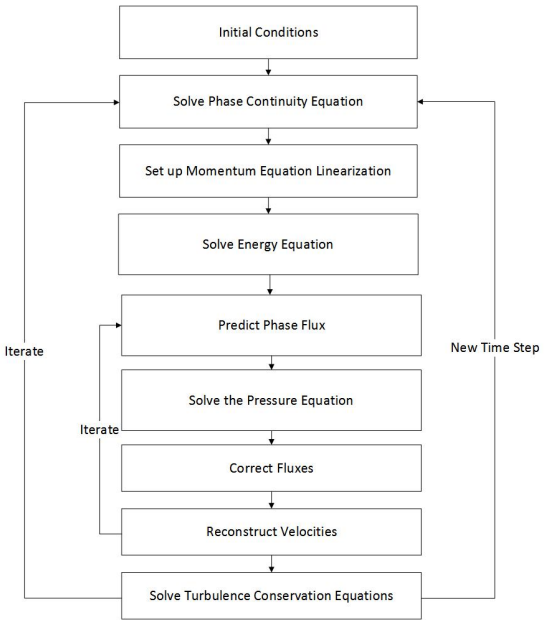

Figure 2.1: The `twoPhaseEulerFoam` algorithm built into `OpenFOAM`.

Once the initial and boundary conditions are specified, the phase continuity equation is solved and the momentum equations are discretized and linearized for use in the pressure equation. The energy equation is solved based on the solution of continuity and the previous conditions for the velocity. The flux is predicted based on the linearization of the momentum equations, and the inner corrector loop of the PIMPLE solution procedure begins. In the inner loop, the root of the pressure equation is found and the fluxes and velocities are corrected based on the updated pressure for a user-defined number of iterations. Following the inner loop, the turbulence equations can then be solved before restarting the outer loop. Alternatively, the turbulence equations can only be solved on the final iteration of the outer loop. The outer loop then begins again based on the new pressure. The outer PIMPLE loop corrects the

continuity equation based on the new velocity, and is crucial for maintaining boundedness and stability in the phase fractions. Once the loops complete, a new time step begins.

The solution procedure within `twoPhaseEulerFoam` does not include a species equation and does not solve for mass transfer between the phases, but this addition was made with a few changes to the algorithm. The changes that were made are shown in Figure 2.2.

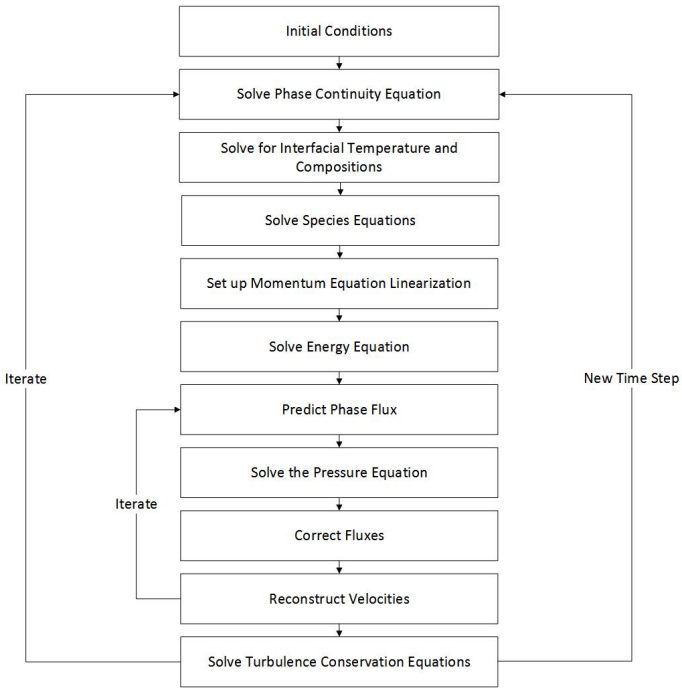

Figure 2.2: The new `twoPhaseEulerFoam` algorithm after adding mass transfer capability.

The outer loop begins with the solution of the phase continuity equation. Next, the interfacial temperature and compositions are found so that the appropriate source terms can be incorporated into the species equations. Once the species equations are computed, the momentum equations are linearized as usual, now inclusive of an explicit source term associated with interphase mass transfer. As in the original algorithm, the energy equation is solved with the incorporation of a latent heat term as well as a term accounting for the convective heat transfer across the gas-liquid interface. The flux is predicted and passed to the pressure equation in the inner loop. The only change in the pressure equation is the addition of the mass transfer term, which is also added in to the phase continuity equations as a source term for the next outer iteration. The fluxes are corrected along with the velocities and passed to the

next inner iteration. The equations to account for turbulence are solved before the outer loop once again calculates the phase fraction from the phase continuity equation. The number of inner and outer iteration loops are specified in the PIMPLE dictionary of the solver.

In the first time-step, the mass transfer term is not actually incorporated into the solution of the continuity equations until the first outer corrector loop is finished because the dilatation rate is not calculated until the pressure equation has been solved. It is this lag in the calculation that makes the reliance on the outer corrector loops so great. The fully adapted algorithm is expanded upon in the following sections.

2.1.1 Interphase Heat and Mass Transfer

Gas-liquid mass transfer was added to the base algorithm by first considering the interface between the phases as infinitely thin and calculating the interfacial quantities. The species fractions and temperature at the interface determine the direction of mass transfer and heat transfer from one phase to the other. If the transfer is from the gas phase to the liquid phase, then the bulk liquid species fraction will be less than the liquid species fraction at the interface, as shown in Figure 2.3. If the transfer is in the opposite direction, the bulk gas species fraction will be lower than the gas species fraction and temperature at the interface. Temperatures within the two phases can also influence the mass transfer, not only the heat transfer, which is why the temperature at the interface must also be calculated.

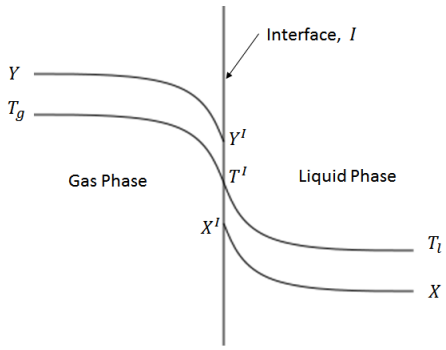

Figure 2.3: The interface between the gas and the liquid. The temperature and compositions are calculated at the interface and included in the source terms of the species equations.

It is further assumed that equilibrium is maintained at the interface, such that the species fractions at the interface can be related by algebraic relationships based on

known or empirically obtained quantities, for instance Henry's law. The interfacial energy balance is,

$$\dot{Q}_{latent,g\to l} + \dot{Q}_{convective,g} = \dot{Q}_{convective,l} \tag{2.1}$$

Where the subscripts g and l indicate the gas and liquid phases respectively, $\dot{Q}_{latent,g\to l}$ $[\mathrm{J}/(\mathrm{s}\cdot\mathrm{m}^2)]$ is the latent heat flux, which is the heat associated with phase change at the interface, and $\dot{Q}_{convective}$ $[\mathrm{J}/(\mathrm{s}\cdot\mathrm{m}^2)]$ is the convective heat flux. Since it is assumed that the interface is infinitely thin, there is no accumulation and the latent heat of dissolution and the total convective heat in the liquid and gas phases must be equal. The volume-averaged convective energy is the sum of the latent heat on either side of the interface,

$$\frac{\dot{Q}_{latent,g\to l}A}{V} = k_{h,g}(T_g - T^I) + k_{h,l}(T_l - T^I) \tag{2.2}$$

Where $k_{h,g} = h_g a_i$ and $k_{h,l} = h_l a_i$ are the volumetric convective heat transfer coefficients $[\mathrm{kg}/(\mathrm{s}^3\cdot\mathrm{K}\cdot\mathrm{m})]$ in the gas and liquid phases respectively, h_l and h_g $[\mathrm{J}/(\mathrm{s}\cdot\mathrm{K}\cdot\mathrm{m}^2)]$ are the convective heat transfer coefficients, a_i $[\mathrm{m}^{-1}]$ is the interfacial area concentration, T_g and T_l [K] are the gas and liquid temperatures respectively, and the superscript I denotes an interfacial property. A $[\mathrm{m}^2]$ is the interfacial area. The volume-averaged latent heat of dissolution is also equal to,

$$\frac{\dot{Q}_{latent,g\to l}A}{V} = \frac{\partial m}{\partial t}(H_g - H_l) \tag{2.3}$$

Where $\frac{\partial m}{\partial t}$ $[\mathrm{kg}/(\mathrm{m}^3\cdot\mathrm{s})]$ is the interfacial volumetric mass transfer rate, equal in value but opposite in sign for the liquid and gas sides, and H_g and H_l [J/kg] are the enthalpies of the gas and liquid respectively. The sign is determined by the mass transfer rate. The mass transfer rate is defined for the gas side as,

$$\frac{\partial m}{\partial t} = \rho_g k_{m,g} \sum_{i=1}^{n} (Y_i^I - Y_i) \tag{2.4}$$

Where ρ_g $[\mathrm{kg}/\mathrm{m}^3]$ is the density of the gas, $k_{m,g}$ $[\mathrm{s}^{-1}]$ is the gas-side (finite) mass transfer coefficient multiplied by the area-to-volume ratio of a bubble, and Y_k $[\mathrm{kg_k}/\mathrm{kg_{gas}}]$ is the mass fraction of species i in the gas.

The interfacial species fractions are calculated based on the balance of the gas and liquid side mass transfer rates for each species,

$$\frac{\partial m_{g,k}}{\partial t} = \frac{\partial m_{l,k}}{\partial t} \tag{2.5}$$

Which can be represented by,

$$\rho_g k_{m,g}(Y_k^I - Y_k) = -\rho_g k_{m,l}(X_k^I - X_k) \tag{2.6}$$

Where X_k $[kg_k/kg_{liquid}]$ is the mass fraction of species k in the liquid. The Henry's law relation between the gas and liquid concentrations of a species in equilibrium is,

$$X_k^I = H_k \frac{Y_k^I \rho_g}{\rho_l} \tag{2.7}$$

Where H_k is the dimensionless Henry's law coefficient. Including the Henry's law relationship in the species balance at the interface and rearranging gives,

$$Y_k^I = \frac{\rho_g k_{m,g} Y_k + \rho_l k_{m,l} X_k}{\rho_g k_{m,l} H_k + \rho_g k_{m,g}} \tag{2.8}$$

The volumetric mass transfer coefficients are defined through Sherwood number correlations as,

$$k_m = a_i D_{k,j} Sh \tag{2.9}$$

Where $a_i = \frac{6\alpha_d}{d}$ $[\mathrm{m}^{-1}]$ is the interfacial area-to-volume ratio, or interfacial area concentration, of the dispersed phase, α_d is the phase fraction of the dispersed phase, d [m] is the dispersed phase (bubble or droplet) diameter, $D_{k,j}$ $[\mathrm{m}^2/\mathrm{s}]$ is the diffusion coefficent, and $Sh = \frac{k_m d}{D_{k,j}}$ is the Sherwood number. Since both the calculation of the diffusion coefficient and the Henry's law coefficient can be taken as temperature dependent, the interfacial temperature must be found simultaneously. The van't Hoff relation, which provides the temperature dependence of the Henry's law coefficient (Sander, 1999), is written as,

$$H_k = H_k^o \exp\left(s_k\left(\frac{1}{T} - \frac{1}{T^o}\right)\right) \tag{2.10}$$

Where the superscript o indicates the reference value at 298 K, and s_k is the slope for the specific species. The expanded energy balance at the interface is,

$$\frac{\partial m}{\partial t}(H_g - H_l) = k_{h,g}(T_g - T^I) + k_{h,l}(T_l - T^I) \tag{2.11}$$

Which can be rearranged for the interfacial temperature,

$$T^I = \frac{k_{h,g}T_g + k_{h,l}T_l - \frac{\partial m}{\partial t}(H_g - H_l)}{k_{h,g} + k_{h,l}} \tag{2.12}$$

Fixed point iteration with Wegstein acceleration was used to find T^I before the species equation is solved. First the interfacial mass transfer was calculated by finding the new interfacial Y^I with Equation 2.8 based on a guess for T^I. The new T^I was found with Equation 2.12 and was used as a new guess for once again calculating the interfacial mass transfer rate from equation 2.4. The process repeats until convergence. The initial guess for the interfacial temperature was the initial temperature of the liquid phase. The final value found for the interfacial temperature is stored until the outer correction completes. The process is repeated on the new outer iteration.

2.1.2 Continuity

Continuity is ensured by solving the phase continuity equation for the dispersed phase, which can change based on the solution of the velocity and pressure fields. The phase continuity equation is not solved in its original form because it must remain tightly coupled to the pressure and momentum equations. As a result, additional terms are incorporated which result in a more stable and bounded solution. The continuity equation in the dispersed phase (subscript d) with mass transfer is written in its original form as,

$$\frac{\partial \rho_d \alpha_d}{\partial t} + \nabla \cdot (\alpha_d \rho_d \overrightarrow{U_d}) = \left(\frac{\partial m_d}{\partial t}\right) \tag{2.13}$$

Where α_d $[\mathrm{m}^3_{\mathrm{phase}}/\mathrm{m}^3_{\mathrm{cell}}]$ is the dispersed volume fraction. The left hand side can be separated into a substantial derivative of the phase fraction, and a substantial derivative of the density, which is brought to the right hand side as follows,

$$\frac{\partial \alpha_d}{\partial t} + \nabla \cdot \alpha_d \overrightarrow{U_d} = -\frac{\alpha_d}{\rho_d}\frac{D\rho_d}{Dt} + \frac{1}{\rho_d}\left(\frac{\partial m_d}{\partial t}\right) \tag{2.14}$$

Zero-sum terms (in bold) are added on either side of the equation and are used in the derivation later,

$$\begin{aligned} &\frac{\partial \alpha_d}{\partial t} + \nabla \cdot \alpha_d \overrightarrow{U_d} + \boldsymbol{\nabla \cdot (\alpha_d \vec{U})} - \boldsymbol{\nabla \cdot (\alpha_d \vec{U})} \\ &= -\frac{\alpha_d}{\rho_d}\frac{D\rho_d}{Dt} + \frac{1}{\rho_d}\left(\frac{\partial m_d}{\partial t}\right) + \boldsymbol{\alpha_d \nabla \cdot \vec{U}} - \boldsymbol{\alpha_d \nabla \cdot \vec{U}} \end{aligned} \tag{2.15}$$

Since $\vec{U} = \alpha_d\vec{U_d} + \alpha_c\vec{U_c}$, where c indicates the continuous phase, one of the added terms on the left hand side can be expanded,

$$\frac{\partial\alpha_d}{\partial t} + \nabla\cdot\alpha_d\vec{U_d} + \nabla\cdot(\alpha_d\vec{U}) - \nabla\cdot\left(\alpha_d(\alpha_d\vec{U_d} + \alpha_c\vec{U_c})\right) \tag{2.16}$$

Combining the second term with the first part of the fourth term gives,

$$\frac{\partial\alpha_d}{\partial t} + \nabla\cdot(1-\alpha_d)\alpha_d\vec{U_d} + \nabla\cdot(\alpha_d\vec{U}) - \nabla\cdot(\alpha_d\alpha_c\vec{U_c}) \tag{2.17}$$

This equation can be rewritten, recalling the definition of the relative velocity, $\vec{U_r} = \vec{U_d} - \vec{U_c}$,

$$\frac{\partial\alpha_d}{\partial t} + \nabla\cdot(\alpha_d\alpha_c\vec{U_r}) + \nabla\cdot(\alpha_d\vec{U}) \tag{2.18}$$

It will be shown later in the derivation of the pressure equation that the dilatation rate for the phase-averaged velocity is,

$$\nabla\cdot\vec{U} = -\left(\frac{\alpha_d}{\rho_d}\frac{D\rho_d}{Dt} - \frac{1}{\rho_d}\left(\frac{\partial m_d}{\partial t}\right)\right) - \left(\frac{\alpha_c}{\rho_c}\frac{D\rho_c}{Dt} - \frac{1}{\rho_c}\left(\frac{\partial m_c}{\partial t}\right)\right) \tag{2.19}$$

Looking at the right-hand side of equation 2.15 and substituting gives,

$$-\frac{\alpha_d}{\rho_d}\frac{D\rho_d}{Dt} + \frac{1}{\rho_d}\left(\frac{\partial m_d}{\partial t}\right) + \alpha_d\nabla\cdot\vec{U} - \alpha_d\left(\frac{1}{\rho_d}\left(\frac{\partial m_d}{\partial t}\right) - \frac{\alpha_d}{\rho_d}\frac{D\rho_d}{Dt} + \frac{1}{\rho_c}\left(\frac{\partial m_c}{\partial t}\right) - \frac{\alpha_c}{\rho_c}\frac{D\rho_c}{Dt}\right) \tag{2.20}$$

Combining the first term with the first two parts of the fourth term gives,

$$\alpha_d\nabla\cdot\vec{U} + (1-\alpha_d)\left(-\frac{\alpha_d}{\rho_d}\frac{D\rho_d}{Dt} + \frac{1}{\rho_d}\left(\frac{\partial m_d}{\partial t}\right)\right) - \alpha_d\left(-\frac{\alpha_c}{\rho_c}\frac{D\rho_c}{Dt} + \frac{1}{\rho_c}\left(\frac{\partial m_c}{\partial t}\right)\right) \tag{2.21}$$

The dilatation rate for each individual phase is,

$$\nabla\cdot\vec{U}_i = -\left(\frac{\alpha_i}{\rho_i}\frac{D\rho_i}{Dt} - \frac{1}{\rho_i}\left(\frac{\partial m_i}{\partial t}\right)\right) \tag{2.22}$$

And noting that $\alpha_c = 1 - \alpha_d$, yields the final form of the RHS of 2.15,

$$\alpha_d\nabla\cdot\vec{U} + \alpha_c\nabla\cdot\vec{U_d} - \alpha_d\nabla\cdot\vec{U_c} \tag{2.23}$$

All together, the compacted form of the continuity equation solved in `twoPhaseEulerFoam` is,

$$\frac{\partial \alpha_d}{\partial t} + \nabla \cdot (\alpha_d \alpha_c \overrightarrow{U_r}) + \nabla \cdot (\alpha_d \overrightarrow{U}) = \alpha_d \nabla \cdot \overrightarrow{U} + \alpha_c \nabla \cdot \overrightarrow{U_d} - \alpha_d \nabla \cdot \overrightarrow{U_c} \tag{2.24}$$

It should be noted that in the code the relative velocity at this point incorporates the turbulent dispersion from the pressure equation as,

$$U_r = (U_d - U_c) + F_{TD,d} + F_{TD,c} \tag{2.25}$$

In the code, equation 2.24 is split into an implicit and an explicit part, which is determined based on the sign of the substantial derivative terms, in the code they are called *dgdt*, in each cell. If they are negative, they are handled implicitly, and if they are positive, they are handled explicitly, which works out because the second term on the right-hand side is also equal to $\nabla \cdot \overrightarrow{U_d} - \alpha_d \nabla \cdot \overrightarrow{U_d}$.
The equation is solved for α_d using the MULES (Multidimensional Universal Limited Explicit Solver) (Jasak and Weller, 1995), which requires the implicit and explicit terms to be given as inputs. Finally, the phase fraction of the continuous phase is calculated as $\alpha_c = 1 - \alpha_d$.

This is not the only way to compute the phase continuity equation, but its form helps maintain boundedness when coupled with the other equations. Prosperetti and Tryggvason (2009), for example, give a summary of other approaches.

2.1.3 Species Conservation

Considering the existence of n species in each phase, $n-1$ species conservation equations were written to solve for the mass fractions of each species in each phase. The mass fraction of the remaining "inert" species was calculated to enforce the condition that the mass fractions in each phase sum to unity. Interphase mass transfer was incorporated through volumetric source terms. The equations were added into the solver for the gas phase as,

$$\frac{\partial \alpha_g \rho_g Y_k}{\partial t} + \nabla \cdot (\alpha_{f,g} \rho_{f,g} \overrightarrow{\phi_g} Y_k) - \nabla^2 \left(\frac{\alpha_{f,g} \nu^t_{f,g} \rho_{f,g} Y_k}{Sc^t_{f,g}} \right) - \nabla^2 \left(\frac{\alpha_{f,g} \nu_{f,g} \rho_{f,g} Y_k}{Sc_{f,g}} \right) = \frac{\partial m_{k,g}}{\partial t} \tag{2.26}$$

Where the subscript f indicates interpolation to the face, the subscript k indicates the species, ν^t and ν [m^2/s] are the turbulent and molecular kinematic viscosities,

respectively, Sc^t and Sc are the turbulent and molecular Schmidt numbers for the phase, respectively, and $\vec{\phi}$ is the face-flux of the phase. The face-flux has units of [m^3/s], but the divergence operator in the code divides through by the face area, giving it effective units of [m/s] in the transport equations. For the liquid phase the equation is,

$$\frac{\partial \alpha_l \rho_l X_k}{\partial t} + \nabla \cdot (\alpha_{f,l} \rho_{f,l} \vec{\phi_l} X_k) - \nabla^2 \left(\frac{\alpha_{f,l} \nu^t_{f,l} \rho_{f,l} Y_k}{Sc^t_{f,l}} \right) - \nabla^2 \left(\frac{\alpha_{f,g} \nu_{f,g} \rho_{f,g} Y_k}{Sc_{f,g}} \right) = \frac{\partial m_{k,l}}{\partial t} \tag{2.27}$$

The individual mass transfer rates are calculated in the gas phase as,

$$\frac{\partial m_{k,g}}{\partial t} = \rho_g k_{m,g} (Y^I_k - Y_k) \tag{2.28}$$

And in the liquid phase as,

$$\frac{\partial m_{k,l}}{\partial t} = \rho_l k_{m,l} (X^I_k - X_k) \tag{2.29}$$

The new species quantities are not incorporated into the continuity equation on the same outer loop iteration, as noted in Section 2.1, but are incorporated into the pressure equation on the first outer loop iteration. The discretized species equations are solved using the linear solution algorithm specified by the user.

2.1.4 Momentum Conservation

In `twoPhaseEulerFoam` the momentum equations are merely set up, but not solved. Their solution is not necessary because of the operator-splitting procedure of Issa (1985) in which the flux across the face is predicted and then corrected by the new pressure, which is shared between the two phases. The momentum equations are written for the i-th phase with the semi-implicit mass transfer source term as,

$$\begin{aligned} \frac{\partial \alpha_i \rho_i \vec{U_i}}{\partial t} + \nabla \cdot (\alpha_{i,f} \rho_{i,f} \vec{\phi_i} \vec{U_i}) - cont_i \vec{U_i} + (\alpha_i \rho_i + C_{vm}) \frac{\partial \vec{U_i}}{\partial t} \\ = \nabla \cdot R^{eff}_i - C_d \vec{U_i} - C_{vm} (\frac{D\vec{U_i}}{Dt} - \frac{D\vec{U_j}}{Dt}) + \frac{\partial m}{\partial t} \vec{U_i} \end{aligned} \tag{2.30}$$

Where C_d is the drag coefficient and C_{vm} is the virtual mass coefficient. The continuity equation without source terms is subtracted from the momentum equation as,

$$cont_i = \frac{\partial \alpha_i \rho_i}{\partial t} + \nabla \cdot (\alpha_{i,f} \rho_{i,f} \vec{\phi_i}) \tag{2.31}$$

Which should be equal to the interphase mass transfer rate and the substantial derivative of the density. The stress rate tensor, R_i^{eff} [N/(s · m^2)] incorporates both the molecular kinematic viscosity and the turbulent kinematic viscosity in the same term, $\nu^{eff} = \nu_i + \nu_{i,t}$, and is computed as,

$$R_i^{eff} = \left[\nabla \cdot (\alpha_i \rho_{i,f} \nu^{eff} \vec{U_i}) - \left(\alpha_i \rho_i \nu^{eff} \left(\nabla \vec{U_i}^T - \frac{2}{3} tr(\nabla \cdot \vec{U_i}) I\right)\right) + \alpha_i \rho_i \frac{2}{3} k_i I\right] \quad (2.32)$$

Where k [m^2/s^2] is the turbulent kinetic energy. The substantial derivatives, which are multiplied by the virtual mass coefficient, are defined as usual. Due to the way the divergence terms are written in the code, they appear as,

$$\frac{D\vec{U_i}}{Dt} = \frac{\partial \vec{U_i}}{\partial t} + \nabla \cdot \vec{\phi_i} \vec{U_i} - \vec{U_i} \nabla \cdot \vec{\phi_i} \quad (2.33)$$

Once the momentum equations have been set up, they are discretized and linearized into the form outlined by Patankar (1980),

$$A_P \overrightarrow{U_P} = \sum A_{nb} \overrightarrow{U_{nb}} + b - \alpha \nabla P_{rgh} \quad (2.34)$$

Where the subscript P denotes the centre of the cell, subscript nb denotes the neighbour cell centres, $P_{rgh} = P - \rho g h$ [Pa] is the modified pressure, g [m/s^2] is the acceleration due to gravity, and h [m] is the height from the reference location. The modified pressure is the pressure without the static component, and is the pressure which is shared between the phases. All of the terms that were not included implicitly in the momentum equation are lumped into the b term, including the lift force, and any other relevant explicit sources.

The explicit part of the drag term is not incorporated at this stage, which will be explained in more detail in the solution to the pressure equation. The pressure gradient term is also left out, as it is solved for as per the operator-splitting method. The linearization as written in Rusche (2002) is adopted,

$$\vec{U_i} = \mathcal{A}_i^{-1} \vec{\mathcal{H}_i} - \mathcal{A}_i^{-1} \alpha_i \nabla P_{rgh} \quad (2.35)$$

2.1.5 Energy Conservation

The next part of the solution procedure is to solve the energy equations for each phase, which may be based on the enthalpy or on the internal energy according to the user's preference. The volume-averaged energy balance for the total energy in

each phase is,

$$\frac{\partial \alpha_i \rho_i E_i}{\partial t} + \nabla \cdot (\alpha_{i,f} \rho_{i,f} \vec{\phi_i} E_i) - \nabla^2 (\alpha_{i,f} \alpha_{i,f}^{eff} \rho_i E_i) = \dot{Q}_{i,convective} + \dot{Q}_{i,latent} + \dot{Q}_{i,potential} \tag{2.36}$$

Where E_i [J] is the total energy, and $\alpha_i^{t,eff} = \alpha_i^t + \alpha_{t,i}^t$ [m^2/s] is the effective thermal diffusivity, where the subscript t indicates the addition due to turbulence and the superscript t indicates a thermal property. The total energy can be separated into kinetic energy and internal energy. In some cases using the enthalpy is preferable in lieu of internal energy, so there are two choices provided, denoted he_i. A term which adds the extra sources for either the internal energy or the enthalpy is defined as,

$$s_i = \begin{cases} P \frac{\partial \alpha_i}{\partial t} + \nabla \cdot (\alpha_{i,f} \vec{\phi_i} P), \text{ Internal Energy} \\ -\alpha_i \frac{\partial P}{\partial t}, \text{ Enthalpy} \end{cases} \tag{2.37}$$

Substituting for the total energy recasts equation 2.36 as,

$$\begin{aligned} \frac{\partial \alpha_i \rho_i (K_i + he_i)}{\partial t} + \nabla \cdot (\alpha_{i,f} \rho_{i,f} \vec{\phi_i} (K_i + he_i)) - \nabla^2 (\alpha_{i,f} \alpha_{i,f}^{t,eff} he_i) + s_i \\ = \frac{\dot{Q}_{i,convective}}{V} + \frac{\dot{Q}_{i,latent}}{V} + \frac{\dot{Q}_{i,potential}}{V} \end{aligned} \tag{2.38}$$

Where $K = \frac{1}{2} U_i^2$ [J/kg] is the kinetic energy. Since there is only thermal diffusion of the internal energy, the kinetic energy in the Laplacian term vanishes. Through expansion of the terms, the equation becomes,

$$\begin{aligned} \frac{\partial \alpha_i \rho_i he_i}{\partial t} + \nabla \cdot (\alpha_{i,f} \rho_{i,f} \vec{\phi_i} he_i) + \frac{\partial \alpha_{i,f} \rho_{i,f} K_i}{\partial t} + \nabla \cdot (\alpha_{i,f} \rho_{i,f} \vec{\phi_i} K_i) - he_i cont_i - K_i cont_i \\ -\nabla^2 (\alpha_{i,f} \alpha_{i,f}^{t,eff} he_i) = \frac{\dot{Q}_{i,convective}}{V} + \frac{\dot{Q}_{i,latent}}{V} + \frac{\dot{Q}_{i,potential}}{V} \end{aligned} \tag{2.39}$$

Expanding the source terms on the right hand side results in the final form of the energy equation in `twoPhaseEulerFoam`,

$$\begin{aligned} \frac{\partial \alpha_i \rho_i he_i}{\partial t} + \nabla \cdot (\alpha_i \rho_i \vec{\phi_i} he_i) + \frac{\partial \alpha_i \rho_i K_i}{\partial t} + \nabla \cdot (\alpha_i \rho_i \vec{\phi_i} K_i) - he_i cont_i - K_i cont_i \\ -\nabla^2 (\alpha_i \alpha_i^{eff} he_i) = k_{h,i} (T^I - T_i) + \left(\frac{k_{h,i}^{eff}}{C_{pv,i}} he_i^I \right)^{explicit} - \left(\frac{k_{h,i}^{eff}}{C_{pv,i}} he_i \right)^{implicit} \\ + \alpha_i \rho_i \vec{U_i} \cdot g + \left(\frac{\partial m_i}{\partial t} he_i^I \right)^{explicit} - \left(\frac{\partial m_i}{\partial t} he_i \right)^{implicit} \end{aligned} \tag{2.40}$$

Where $k_{h,i}$ [W/(m^{2}K)] is the convective heat transfer coefficient of the phase, $k_{h,i}^{eff} = \frac{k_{h,i}k_{h,j}}{k_{h,i}+k_{h,j}}$ [W/(m^{2}K)] is the effective volumetric convective heat transfer coefficient, and C_{pv} [J/(kg $\cdot$ K)] is the specific heat capacity at constant pressure or volume, depending on the energy type selected. The energy equations are solved using a solution algorithm specified by the user.

2.1.6 The Pressure Equation

To solve for the new pressure field, as per Rhie and Chow (1983), the $\vec{\mathcal{H}}$ vector and $\mathcal{A}$ matrix of the linearized momentum equations must be interpolated to the face while the pressure is calculated at the cell centre. A phase average of the linearized equations in each phase is taken as in the volume fraction equation, beginning with the continuity equation in each phase,

$$\frac{\partial \rho_i \alpha_i}{\partial t} + \nabla \cdot (\alpha_i \rho_i \vec{U_i}) + \alpha_i \frac{D\rho_i}{Dt} - \frac{\partial m_i}{\partial t} = 0 \tag{2.41}$$

This can be expanded to become,

$$\rho_i \frac{\partial \alpha_i}{\partial t} + \alpha_i \frac{\partial \rho}{\partial t} + \rho_i \nabla \cdot \alpha_i \vec{U_i} + \alpha_i \vec{U_i} \cdot \nabla \rho_i + \alpha_i \frac{D\rho_i}{Dt} - \frac{\partial m_i}{\partial t} = 0 \tag{2.42}$$

Rearranging,

$$\frac{\partial \alpha_i}{\partial t} + \nabla \cdot \alpha_i \vec{U_i} + \frac{\alpha_i}{\rho_i} \frac{D\rho_i}{Dt} - \frac{1}{\rho_i} \left(\frac{\partial m_i}{\partial t} \right) = 0 \tag{2.43}$$

The equations for each phase must be added together, and because the sum of the phase fractions does not change with time, the resulting equation is,

$$\nabla \cdot \alpha_d \vec{U_d} + \frac{\alpha_d}{\rho_d} \frac{D\rho_d}{Dt} + \nabla \cdot \alpha_c \vec{U_c} + \frac{\alpha_c}{\rho_c} \frac{D\rho_c}{Dt} - \frac{1}{\rho_d} \left(\frac{\partial m_d}{\partial t} \right) - \frac{1}{\rho_c} \left(\frac{\partial m_c}{\partial t} \right) = 0 \tag{2.44}$$

Recalling $\alpha_d \vec{U_d} + \alpha_c \vec{U_c} = \vec{U}$, the equation reduces to,

$$\nabla \cdot \vec{U} + \frac{\alpha_d}{\rho_d} \frac{D\rho_d}{Dt} + \frac{\alpha_c}{\rho_c} \frac{D\rho_c}{Dt} - \frac{1}{\rho_d} \left(\frac{\partial m_d}{\partial t} \right) - \frac{1}{\rho_c} \left(\frac{\partial m_c}{\partial t} \right) = 0 \tag{2.45}$$

This equation can be rearranged for the dilatation rate, $\nabla \cdot \vec{U}$, between the two fluids. It must be noted that the substantial derivative of the density is incorporated into

the pressure equation as,

$$\frac{\alpha_i}{\rho_i}\left(\frac{D\rho_i}{Dt}\right) = \frac{1}{\rho_i^{explicit}}\left(\left[\frac{\partial \alpha_i \rho_i}{\partial t} + \nabla \cdot (\alpha_{i,f}\rho_{i,f}\vec{\phi_i})\right] - \rho_i^{implicit}\left[\frac{\partial \alpha_i}{\partial t} + \nabla \cdot (\alpha_{i,f}\vec{\phi_i})\right]\right) + \left(\frac{\alpha_i}{\rho_i}\right)^{explicit}\frac{D\left(\psi_i P_{rgh}^N\right)}{Dt} \tag{2.46}$$

Where $\psi_i = \rho_i / P_{rgh}$ is the phase compressibility factor. In the code, the compressibility term included in the substantial derivative uses a correction function defined in fvMatrix.C. The velocity is written as,

$$\vec{U} = \alpha_d \overrightarrow{U_d} + \alpha_c \overrightarrow{U_c} = \alpha_d \frac{\overrightarrow{\mathcal{H}_d} + C_d \overrightarrow{U_c} + \alpha_d \nabla P_{rgh}}{\mathcal{A}_d} + \alpha_c \frac{\vec{H}_c + C_d \overrightarrow{U_d} + \alpha_c \nabla P_{rgh}}{\mathcal{A}_c} \tag{2.47}$$

Defining the overall $\vec{H}$ term as inclusive of the explicit drag terms,

$$\vec{H} = \alpha_d(\overrightarrow{\mathcal{H}_d} + C_d U_c) + \alpha_c(\overrightarrow{\mathcal{H}_c} + C_d U_d) \tag{2.48}$$

Equation 2.47 is interpolated to the face and written more compactly as,

$$\overrightarrow{U_f} = \frac{\overrightarrow{\mathcal{H}_f}}{\mathcal{A}_f} + (\alpha_d^2 \mathcal{A}_d^{-1} + \alpha_c^2 \mathcal{A}_c^{-1})_f \nabla P_{rgh} \tag{2.49}$$

The total pressure equation becomes,

$$\nabla \cdot \left(\frac{\overrightarrow{\mathcal{H}_f}}{\mathcal{A}_f} + (\alpha_d^2 \mathcal{A}_d^{-1} + \alpha_c^2 \mathcal{A}_c^{-1})_f \nabla P_{rgh}\right) + \frac{\alpha_d}{\rho_d}\left(\frac{D\rho_d}{Dt}\right) + \frac{\alpha_c}{\rho_c}\left(\frac{D\rho_c}{Dt}\right) - \frac{1}{\rho_d}\left(\frac{\partial m_d}{\partial t}\right) - \frac{1}{\rho_c}\left(\frac{\partial m_c}{\partial t}\right) = 0 \tag{2.50}$$

Which can be separated to become the final form of the pressure equation as written in the code,

$$\nabla \cdot \left(\frac{\overrightarrow{\mathcal{H}_f}}{\mathcal{A}_f}\right) + \nabla^2\left((\alpha_d^2 \mathcal{A}_d^{-1} + \alpha_c^2 \mathcal{A}_c^{-1})_f P_{rgh}\right) + \frac{\alpha_d}{\rho_d}\left(\frac{D\rho_d}{Dt}\right) + \frac{\alpha_c}{\rho_c}\left(\frac{D\rho_c}{Dt}\right) - \frac{1}{\rho_d}\left(\frac{\partial m_d}{\partial t}\right) - \frac{1}{\rho_c}\left(\frac{\partial m_c}{\partial t}\right) = 0 \tag{2.51}$$

The equation is solved iteratively to find the modified pressure. Once the convergence criteria (specified by the user) is met, the average flux is reconstructed as,

$$\vec{\phi} = \left(\mathcal{A}_f^{-1} \overrightarrow{\mathcal{H}_f} + (\alpha_d^2 \mathcal{A}_d^{-1} + \alpha_c^2 \mathcal{A}_c^{-1}) \nabla \cdot P_{rgh} \right)_f \cdot A_s \tag{2.52}$$

Where A_s is the surface area vector. In order to reconstruct the phase fluxes, several intermediate steps are taken. In this solver, the explicit drag terms were only added into the $\overrightarrow{\mathcal{H}_f}$ and not into the individual $\overrightarrow{\mathcal{H}_{i,f}}$ because a reliance on the old value of the individual $\vec{\phi_i}$ when reconstructing the two fluxes could be unstable in flow cases. The `twoPhaseEulerFoam` solver approximates the new fluxes with an expression based on the drag coefficient which requires calculating the dragless $\vec{\phi_i}$. It seems quite stable in flow cases, but could cause significant problems in low-flow cases because the pressure field may overcompensate for a drag contribution which should be negligible.
The individual $\vec{\mathcal{H}_i}$, calculated at the cell centres, do not contain the explicit drag source terms in the current notation. The first step is to create individual $\vec{\phi_i}$ without the drag term,

$$\overrightarrow{\phi_{s,i}} = (\mathcal{A}_i^{-1} \overrightarrow{\mathcal{H}_{i,f}} + \alpha_i \mathcal{A}_i^{-1} \nabla \cdot P_{rgh})_f \cdot A_s \tag{2.53}$$

A relative flux term is created from the two individual dragless phase fluxes and the drag additions. It is defined as,

$$\vec{\phi_r} = \frac{\left((\overrightarrow{\phi_{s,1}} + \mathcal{A}_{1,f}^{-1} C_d \overrightarrow{\phi_{s,2}}) - (\overrightarrow{\phi_{s,2}} + \mathcal{A}_{2,f}^{-1} C_d \overrightarrow{\phi_{s,1}}) \right)}{1 - (\mathcal{A}_{1,f}^{-1} C_d)(\mathcal{A}_{2,f}^{-1} C_d)} \tag{2.54}$$

Where C_d is the drag coefficient, which should be equal in both phases. The individual phase fluxes are then constructed from the relative and average quantities,

$$\begin{aligned} \vec{\phi_1} &= \vec{\phi} + \alpha_{2,f} \vec{\phi_r} \\ \vec{\phi_2} &= \vec{\phi} - \alpha_{1,f} \vec{\phi_r} \end{aligned} \tag{2.55}$$

Once the fluxes have been found, the face values must be reconstructed to the cell centres in order to find the velocities. Again, since the $\vec{\mathcal{H}_i}$ values do not contain the explicit drag sources, they must be reincorporated into the velocity reconstruction at this stage. As with the fluxes, the velocities are calculated in stages because the drag term is problematic.
The pressure and force terms are reconstructed to the cell centres. This is done by

taking the sum of all the faces multiplied by the unit vector to the face, multiplying the face values by their area and summing them, and taking the dot product of the two quantities,

$$reconstruct_i = \sum_S \left[\left(\frac{A_s}{|A_s|} \right) A_s \right]^{-1} \cdot \sum_S A_s \left[(\alpha_i \mathcal{A}_i^{-1} \nabla \cdot P_{rgh})_f \cdot A_s - \alpha_i \mathcal{A}_i^{-1} (F_{g,f,i} + F_{s,f,i}) \right] \tag{2.56}$$

Where $F_{g,f,i}$ is the gravitational source term of the i-th phase interpolated to the face, and $F_{s,f,i}$ are all other source terms (except drag) of the i-th phase interpolated to the face. The individual dragless velocities are calculated as,

$$\overrightarrow{U_{s,i}} = \mathcal{A}_i^{-1} \overrightarrow{\mathcal{H}_i} + reconstruct_i \tag{2.57}$$

The drag terms are incorporated into an average velocity,

$$\overrightarrow{U_{avg}} = \alpha_1 (\overrightarrow{U_{s,1}} + \mathcal{A}_1^{-1} C_d U_2) + \alpha_2 (\overrightarrow{U_{s,2}} + \mathcal{A}_2^{-1} C_d \overrightarrow{U_1}) \tag{2.58}$$

And a relative velocity is also constructed using the same technique as was done with the relative flux,

$$\overrightarrow{U_r} = \frac{(1 + \mathcal{A}_2^{-1} C_d) \overrightarrow{U_{s,1}} - (1 + \mathcal{A}_1^{-1} C_d) \overrightarrow{U_{s,2}}}{1 - (\mathcal{A}_1^{-1} C_d)(\mathcal{A}_2^{-1} C_d)} \tag{2.59}$$

The velocities are then constructed from the average and relative quantities,

$$\begin{aligned} \overrightarrow{U_1} &= \overrightarrow{U_{avg}} + \alpha_2 \overrightarrow{U_r} \\ \overrightarrow{U_2} &= \overrightarrow{U_{avg}} - \alpha_1 \overrightarrow{U_r} \end{aligned} \tag{2.60}$$

The static pressure is recalculated and limited,

$$P = P_{rgh} + \rho g \cdot h \tag{2.61}$$

where ρ is the phase-averaged density. The densities are updated using the compressibility and the new and old modified pressure values,

$$\rho_i = \rho_i^0 + \psi_i (P_{rgh}^N - P_{rgh}^{N-1}) \tag{2.62}$$

Where the superscript $N-1$ indicates the old-time value. Finally the kinetic energies, for use in the energy equation, are updated,

$$K_i = \frac{|\vec{U_i}|^2}{2} \tag{2.63}$$

Chapter 3

Sub-Models for the Transport Equations

The Euler-Euler approach requires the use of empirical models, which provide the closure relations for the equations of mass, momentum and energy. The sub-models must be selected based on their ranges of applicability to each specific case. For a gas dispersed in a liquid, there are a number of relationships that must be taken into account. Figure 3.1 shows some of the known interactions for the bubbly flow scenarios of interest for the present study.

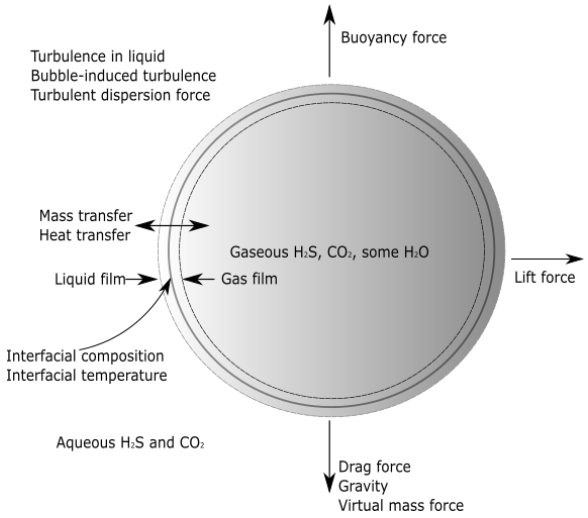

Figure 3.1: The interactions between a single sour gas bubble and the surrounding water in the plume region.

The interactions can be divided into three categories. The first category comprises the interphase forces, the forces which account for the presence and behaviour of the other fluid. The second is heat and mass transfer across the bubble interface, both of which determine the composition and temperature of the phases. The final category is the fluid stress due to velocity fluctuations, which can alter the normal Newtonian behaviour of the liquid continuous phase. Additional models which can be implemented account for the interactions of the bubbles with themselves, and how their population and size evolve over time.

To this day, semi-empirical models are commonly used in simple hand calculations to predict the behaviour of two-phase flow. Many of the same models have been adapted for use in CFD codes. The implementation of models that are not valid within the range of application or overly simple in a CFD simulation can add significant error when comparing to experimental results. Selection of appropriate models is paramount to making an accurate prediction, particularly in complicated flow scenarios such as the underwater gas well blowout.

There are a plethora of models available for each of the interphase forces, turbulence, mass transfer, and bubble size. Since almost all of the models require tuning parameters, the number of variables can quickly become unmanageable if all of the possible models must be validated and cross-validated with each other. Due to the number of sub-models and their inter-dependence, it is also nearly impossible to find the exact value for each of the tuning parameters in the models which give the most realizable result. For this reason, most of the interphase force models used in this study were selected based on their ranges of applicability from the literature, and were used consistently throughout in the individual studies which proceed from this chapter. Tuning was applied only to the lift force and the turbulent dispersion force to attempt to match experimental data. This chapter details and provides justification for the use of the models implemented in the following chapters.

3.1 Interphase Force Modeling

At low gas volume fractions, or holdups, the behaviour of the dispersed phase is primarily impacted by the behaviour of the continuous phase. At moderate or high dispersed phase fractions, the dispersed phase has a greater impact on the behaviour of the continuous phase (Behzadi et al., 2004). In the cases of interest to most of industry, the dispersed phase fraction will be high, and for this reason a two-way coupling between the phases is required. The formulation of the momentum equation in the `twoPhaseEulerFoam` algorithm allows for this coupling by ensuring that the momentum equation does not become singular in regions where the liquid phase fraction approaches zero and becomes the dispersed phase (Rusche, 2002).

Interphase forces help to maintain the two-way coupling between the phases primarily through their reliance on the relative velocity. Without the presence of these terms in the momentum equations, the velocity of the other phase would never appear in the momentum equations for the phase. Some of the interphase forces have been derived directly from the physical laws, and do not require a model on the macroscale

as a result. The two forces which do not require modeling are the buoyancy force and the gravitational force. The buoyancy force is driven by the difference in density between the two phases, and is the dominant upward force in the plume region. The gravitational force accounts for the weight of the bubble by the downward acceleration due to gravity. The pressure is also responsible for the direction and magnitude of motion of the bubble, but it is determined directly through the algorithm and also does not require a model.

One of the most important considerations for the application of interphase force models is the flow regime. Table 3.1 from Coulson et al. (1996) gives a description of some of the known flow regimes at different gas and liquid velocities for horizontal and vertical flow through pipes. In vertical pipes, mist flow, stratified flow, and plug flow are not typically seen. Since this table describes pipe flow, and not unconfined flow such as the gas well blowout scenario, many of the regimes are not applicable. In the plume region of an underwater gas well blowout, the bubbly regime is the most likely.

Table 3.1: Flow regimes for two-phase flows (Coulson et al., 1996)

		Typical Velocities [m/s]	
Regime	**Description**	**Liquid**	**Vapour**
1. Bubble Flow	Bubbles of gas dispersed throughout the liquid	$1.5 - 5$	$0.3 - 3$
2. Plug flow	Plugs of gas in liquid phase	0.6	< 1.0
3. Stratified flow	Layer of liquid with a layer of gas above	< 0.15	$0.6 - 3$
4. Wavy flow	As stratified but with a wavy interface due to higher velocities	< 0.3	> 5
5. Slug flow	Slug of gas in liquid phase	Occurs over a wide range of velocities	
6. Annular flow	Liquid film on inside walls with gas in centre		> 6
7. Mist flow	Liquid droplets dispersed in gas		> 60

The bubbly flow regime does not necessarily indicate a uniform bubble shape or size. Bubble shape is known to be influenced by surface tension, viscosity of the continuous phase, bubble diameter and relative velocity, as well as the presence of surfactants or other contaminants. Aside from the relative velocity, these parameters are all intrinsic fluid properties dependent only on the intensive thermodynamic quantities. It is the balance between the intrinsic nature of the two fluids and the inertial forces which determine the bubble shapes that are possible. The different shapes can be divided into regimes which represent the balance between the properties of the fluids and the forces acting upon them.

Since many interphase force models are based on the assumption of a spherical

bubble, the shape regime must be known in advance to ensure that a model in the correct range of validity is selected. This is much easier in theory than in practice, particularly since many of the models are only valid within small ranges for specific flow regimes. Figure 3.2 adapted from Clift et al. (1978), plots the bubble shape regime over a range of Reynolds numbers, Re, Morton numbers, M, and Eötvös numbers, Eo.

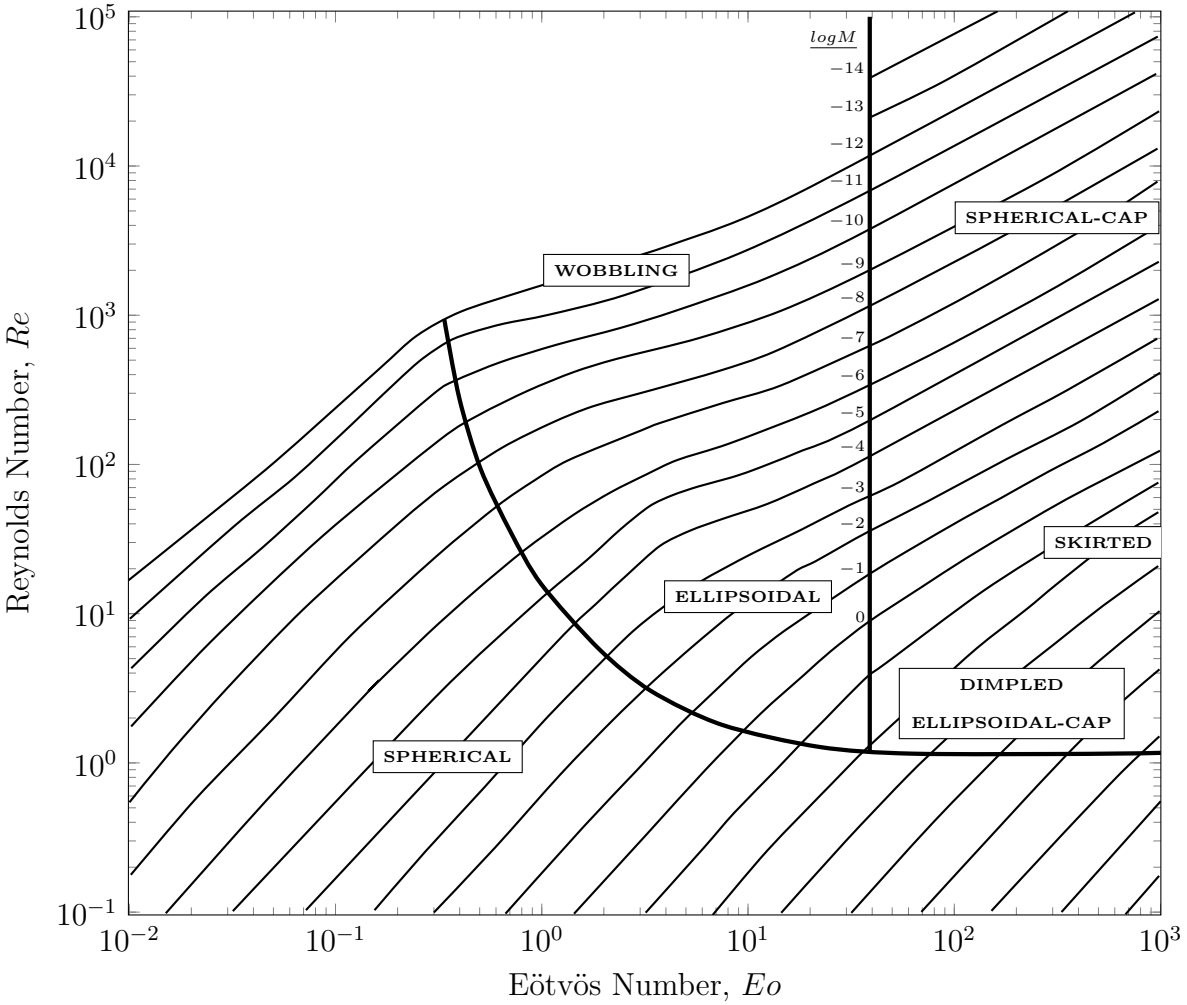

Figure 3.2: Shape regimes for bubbles and drops in unhindered gravitational motion through liquids (adapted from Clift et al. (1978)).

The dimensionless numbers are defined as,

$$Eo = \frac{g\Delta\rho d^2}{\sigma}, \quad M = \frac{g\mu_l^4\Delta\rho}{\rho_l^2\sigma^3}, \quad Re = \frac{\rho_l U_t d}{\mu_l} \tag{3.1}$$

Where the Reynolds number is evaluated at the magnitude of the terminal bubble velocity, U_t.

Spherical bubbles are observed at lower Reynolds numbers over the full range of Eötvös numbers, where the viscous forces are higher and the bubble diameter is lower. Larger diameter bubbles tend to be ellipsoidal at higher Eötvös number because their surface tension is no longer able to maintain their shape and inertial forces can deform them. Ellipsoidal bubbles are not necessarily symmetric, and tend to wobble at higher Reynolds numbers. Spherical cap bubbles will appear at even higher Reynolds and Eötvös numbers where the buoyancy can form them into half-spheres or -ellipsoids, leading with their curved side. At very low surface tension and gas density, the skirted and dimpled-ellipsoidal cap bubbles are present (Clift et al., 1978). The flow and shape regimes must be taken into account before the models are chosen. In the plume region of an underwater blowout, it is likely that many of the bubble types discussed would be present at various locations in the plume, so multiple models could be implemented depending on the bubble size and relative velocity.

3.1.1 The Drag Force

The drag force is of particular importance in the two fluid model because it is the force which accounts for the resistance of the liquid to the movement of the bubble. It also is the primary force which influences the liquid to move due to the gas, and is the only interphase force which is contained in the explicit $\mathcal{H}_i$ terms of the momentum equation linearization, as well as in the flux correction of `twoPhaseEulerFoam`. Coupling is provided through the relative velocity. The drag force is represented by,

$$F_{drag} = -\frac{3\alpha_d \rho_c}{4d} C_d |\overrightarrow{U_r}| \overrightarrow{U_r} \tag{3.2}$$

Where C_d is the modeled drag force coefficient, d is the bubble diameter, the subscript d represents the dispersed phase, $\overrightarrow{U_r} = \overrightarrow{U_d} - \overrightarrow{U_c}$ [m/s] is the relative velocity, and the subscript c indicates the continuous phase. It is known from experiment that the drag coefficient is dependent on the bubble radius, the particle Reynolds number based on the relative velocity, and the shape and impurities of the bubble (Kolev, 2012). The presence of other bubbles in the vicinity can also impact the drag force due to their influence on the continuous phase through which the bubble must move, for instance the wake effects which alter the viscosity of the liquid.

Figure 3.3 shows the value of the drag coefficient for gas bubbles moving through

a continuous liquid medium at terminal velocity for three popular models: Ishii and Zuber (1979), Schiller and Naumann (1933), and Kolev (2007). The graph is not representative of bubbles which have not yet reached their terminal velocities. The Schiller and Naumann (1933) model was originally derived for glass beads, and is only meant to be used for solid spherical particles. It is given as,

$$C_d = \begin{cases} \frac{24}{Re}(1 + 0.15Re^{0.687}), & Re \leq 800 \\ 0.44, & Re > 800 \end{cases} \tag{3.3}$$

The Ishii and Zuber (1979) model is a combination model that is represented by a step function. It is given for a range of flow regimes as,

$$C_d = \begin{cases} \frac{24}{Re}(1 + 0.1Re^{0.75}), & \text{Undistorted} \quad r_d\left(\frac{\rho_c g \nabla\rho}{\mu_c}\right) \geq 34.65 \\ \frac{2}{3}(Eo)^{1/2}\left[\frac{1+17.67f(\alpha_g)^{6/7}}{18.67f(\alpha_g)}\right]^2, & N_\mu \geq \frac{0.11(1+\psi)}{\psi^{8/3}} \text{ Distorted} \\ \frac{8}{3}(1-\alpha_g)^2, & \text{Churn} - \text{turbulent} \end{cases} \tag{3.4}$$

Churn-turbulent flow is typified by a high Reynolds number with bubbles which readily coalesce, and is usually classified in the bubbly regime. The other parameters are defined as,

$$\begin{gathered} f(\alpha_g) = \frac{\mu_l(1-\alpha_g)^{1/2}}{\mu_{mix}}, \quad \mu_{mix} = \mu_l(1-\alpha_g)^{\frac{-2.5(\mu_g+0.4\mu_l)}{\mu_g+\mu_l}} \\ N_\mu = \frac{\mu_l}{\left(\rho_l\sigma(\frac{\sigma}{g\Delta\rho})^{1/2}\right)^{1/2}}, \quad \psi = 0.55\left[(1+0.08r_o^3)^{4/7} - 1\right]^{3/4}, \quad r_o = \frac{r_d}{(\frac{\rho_l g\Delta\rho}{\mu_l})^{1/3}} \end{gathered} \tag{3.5}$$

Where r_d [m] is the bubble radius. Finally, the model assembled by Kolev (2007, pp. 37-39) for the viscous ($C_{d,vis}$), distorted ($C_{d,dis}$), and spherical-cap ($C_{d,cap}$) bubble regimes is,

$$C_d = \begin{cases} C_{d,vis} = \frac{24}{Re}(1 + 0.1Re^{0.75}) & C_{d,dis} < C_{d,vis} \\ C_{d,dis} = \frac{2}{3}\sqrt{\frac{g\rho_l}{\sigma}}d\left(\frac{1+17.67\alpha_l^{1.286}}{18.67\alpha_l^{1.5}}\right)^2 & C_{d,cap} > C_{d,dis} > C_{d,vis} \\ C_{d,cap} = \frac{3}{8}\alpha_l^2 & C_{d,dis} > C_{d,cap} \end{cases} \tag{3.6}$$

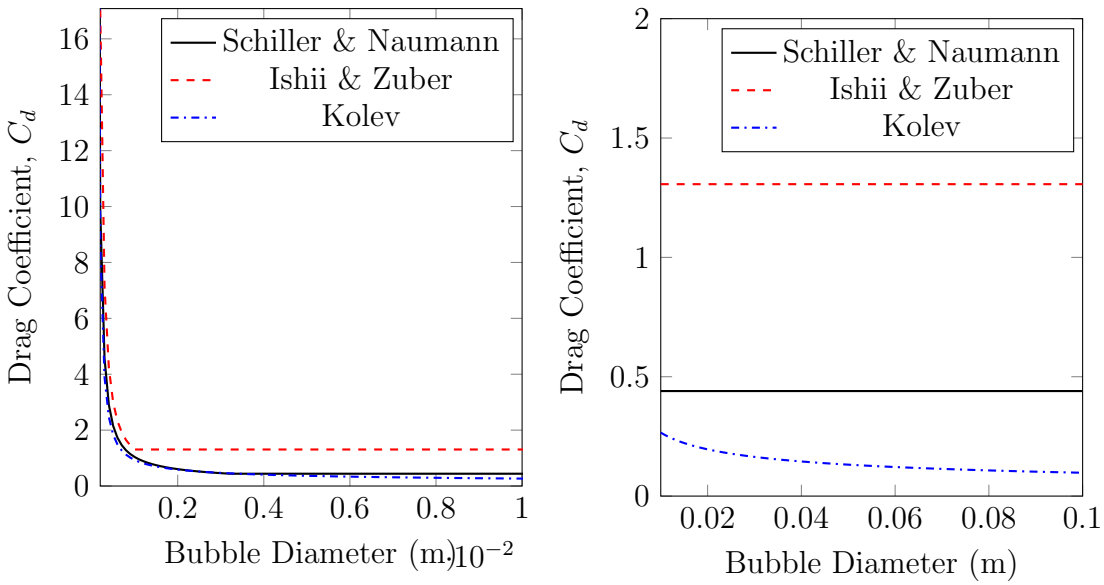

Figure 3.3: Drag coefficient vs. bubble diameter at terminal velocity. Low (left) and higher (right) ranges of bubble sizes. The Ishii and Zuber (1979) and Kolev (2007) models were calculated with $\alpha_g = 0.3$ and properties were obtained for air (dispersed) and water (continuous) at STP.

Other correlations for the drag force, such as Tomiyama et al. (2002a) require the advance knowledge of an approximate distortion coefficient β. As data for large scale gas well blowouts is unavailable, the distortion coefficient cannot be known in advance, and these models would not necessarily be more accurate. For the bubble sizes of interest in the validation cases, the Kolev (2012) and Schiller and Naumann (1933) models yield very similar results, overlapping at several diameters on the graph.

In the simulations of a gas-stirred ladle, carried out by Lou and Zhu (2013b), the drag coefficient of Kolev (2012) was determined to give the most accurate result for the liquid velocity and the turbulent kinetic energy out of the five models they compared. The drag force was assumed to be well-represented by the model of Kolev (2012) for the validation cases in this work for this reason unless otherwise indicated.

3.1.2 The Lift Force

The lift force acts in the direction perpendicular to the direction of flow. It is very important in the determination of the lateral spreading of bubbles, and aside from turbulence effects, is the only other mechanism by which the characteristic cone of the bubble plume is achieved. Many authors have determined the analytical, numerical, or experimental lift force in a variety of fluid regimes. For the present discussion,

focus is on models for the lift force acting on clean bubbles in viscous flow, as there are several proposed forms for the lift force. It is typically written for a gas-liquid system as,

$$F_L = -C_L \alpha_d \rho_c \frac{\pi d^3}{6} \overrightarrow{U_r} \times (\nabla \times \overrightarrow{U_c}) \tag{3.7}$$

Where C_L is the lift coefficient.

Legendre and Magnaudet (1998) studied the flow around a single spherical bubble by numerically solving the three-dimensional momentum (Navier-Stokes) equations for a spherical shear-free bubble at constant velocity in a variety of flows. They found that the lift coefficient was strongly dependent on Reynolds number and shear rate at low Reynolds number, but became less so at higher Reynolds numbers. Legendre et al. (2003) investigated the interactions between two bubbles rising side by side. The study revealed that when the Reynolds number crossed a certain critical value, the sign of the lift force was reversed. Other studies have confirmed the assertion of a critical value for the sign change of the lift force based on the bubble diameter (Lucas and Tomiyama, 2011).

Hibiki and Ishii (2007) put together an extensive list of lift force models with their applicability limits. The majority of the models in the list have only been formulated for single solid spheres or bubbles, and very few are within the appropriate regime for the cases of interest to the current research.

Tomiyama et al. (2002b) proposed a model obtained through experiment for a single bubble in laminar, high-viscosity flow,

$$C_L = \begin{cases} min\big[0.288tanh(0.121Re), f(Eo)\big], & Eo < 4 \\ f(Eo), & 4 \leq Eo \leq 10.7 \end{cases} \tag{3.8}$$

Where,

$$f(Eo) = 0.00105Eo^3 - 0.0159Eo^2 - 0.0204Eo + 0.474 \tag{3.9}$$

The model was determined to be valid for $-5.5 \leq logM \leq -2.8$. Referring to Figure 3.2, the given range is within the spherical, spherical cap, and ellipsoidal bubble regimes. The model was later used for multiple-bubble turbulent simulations in air-water systems for small and large diameter pipes with good results (Lucas and Tomiyama, 2011). As discussed by Sokolichin et al. (2004), lift coefficients for small bubbles < 6 mm are predicted in the range $0 < C_L \leq 0.288$, and for large bubbles $-0.288 < C_L < 0$.

For this work, a constant lift coefficient was used within the given limits which

gave the most realizable results. Although the coefficient of Tomiyama et al. (2002b) would technically be applicable to all bubble sizes, in the validation cases of this work it did not provide satisfactory results. This was likely because many of the cases assumed a constant bubble size and in these cases the lift coefficient would have been represented better with a statistical average of the lift coefficients of the true bubble size distribution instead of simply the calculated lift coefficient at that single size. Being able to tune the coefficent was absolutely necessary as the lift force had a major impact in all of the validation cases studied.

3.1.3 The Virtual Mass Force

The virtual mass force accounts for the weight of the surrounding fluid due to the acceleration of another body through it. It is of particular importance in bubbly flow because the bubble density is normally much lower than the density of the liquid it displaces. Several models have been proposed for the virtual mass effect in bubbly two-phase flows. Soo (1967), Hinze (1963), and Wallis (1969) observed through analytical derivation that the force was proportional to the substantial derivative of the relative velocity.

Drew et al. (1979) determined that previous formulations of the virtual mass force were not mathematically objective. They derived a new formulation of the virtual mass force on the basis that the objectivity of the surface traction must be maintained. The result was similar to previous models but with two additional spatial derivative terms and an empirical parameter, λ.

The virtual mass force model of Cook and Harlow (1984) was derived with mathematical objectivity in mind. They sought to find a virtual mass model which did not require two empirical parameters. They defined three phases - the bulk fluid, the dispersed gas phase, and the liquid phase surrounding the gas - and derived a model similar to the others which only incorporated the fractional multiplier relating the gas phase and the surrounding liquid phase as an adjustable parameter.

The well-posedness of the two-phase Navier Stokes equations has been addressed by Gidaspow (1974). It was determined that the equations had complex eigenvalues and as a result were intrinsically unstable. Ramshaw and Trapp (1978) observed that the reduction of the imaginary component (i.e. by reducing the first and third characteristic invariants) in relation to the real component improved the stability of the equations. They also determined that the incorporation of known physical effects, such as the surface tension, achieved this. Lahey (2005) concluded that the inclusion

of a virtual mass force also improves stability in the CFD solution of the momentum equations for the same reason.

Lahey (2005) compared the models of Drew et al. (1979) and Wallis (1969) to momentum equations with no virtual mass force in a number of simulations with different gas nozzle shapes and flow orientations. They found that the formulation of the virtual mass force and the magnitudes of the virtual mass coefficient and λ did not affect the result significantly, but the simulations without a virtual mass force were less stable and required longer computational time.

Since the formulation of the virtual mass force, regardless of objectivity, is unlikely to significantly impact the solution, a version which is simple to implement was used for the sake of stability. For the present study, the virtual mass force was represented by the relation used by Soo (1967),

$$F_{VM} = \alpha_g \rho_g C_{VM} \left[\frac{D\vec{U_g}}{Dt} - \frac{D\vec{U_l}}{Dt} \right] \tag{3.10}$$

Where $C_{VM} = 0.5$. Some bubble plume studies do not implement it at all, e.g. Lou and Zhu (2013a), but many who do, use this version.

3.1.4 Turbulent Dispersion

Lopez de Bertodano (1992) observed that the momentum equations do not account for the fluctuating component of the dispersed phase fractions which would be expected in a turbulent field. He proposed an analogue to thermal diffusion of air molecules for bubbles under the influence of turbulence due to the turbulent energy of the other phase. He derived the following expression for the turbulent dispersion force,

$$F_{TD} = C_{TD} \rho_l k_l \nabla \alpha_g \tag{3.11}$$

Where C_{TD} is the turbulent dispersion coefficient and the $\nabla \alpha_g$ came from approximating $ln(1 - \alpha)$ as the first term in a Taylor series expansion. Although there have been other forms for the turbulent dispersion force (Drew, 2001; Gosman et al., 1992; Lopez de Bertodano, 1998) which have been proposed, this formulation has been widely used.

Values of the coefficient vary between 0 and 1 in the literature. The magnitude of the force is very important in determining the spread of the gas and feeds back into the turbulence model. In this work, C_{TD} was tuned along with the lift coefficient

through trial and error to attempt to obtain the most realizable result.

Another model which has been used in the literature is the model of Davidson (1990). It does not involve any tuning parameters of its own, but its result is highly dependent on the choice of drag model. The model is written as,

$$F_{TD} = 0.75\frac{C_d}{d}\mu_t\alpha_l\rho_l|U_r|\nabla\alpha_g \tag{3.12}$$

3.2 Turbulence Modeling

Turbulence poses a significant modeling challenge in the numerical simulation of bubbly two-phase flow. In turbulent flow, the Newtonian fluid stress is increased by the additional stress due to the fluctuating velocity. With the inclusion of two phases, the fluid stresses become more difficult to characterize. The stress in each phase is increased with the generation of turbulent fluctuations with low energy dissipation. These conditions could be caused by minor variations in the other properties or inlet effects. The motion of the bubbles also has a major influence on the stresses in the liquid.

Kolmogorov (1941) identified three ranges in what is referred to as the energy cascade: energy generation, the inertial subrange, and energy dissipation. The generation of energy occurs at the largest turbulence length scales, while the dissipation of energy occurs at smaller scales by viscous forces. The generated energy passes from the larger, anisotropic scales to the smaller, statistically isotropic scales.

The largest length scales of the eddies in any fluid system are restricted to the shortest dimension of the fluid's container, while the smallest are not determined by geometry but by the Kolmogorov length scale (first similarity hypothesis). In between the smallest and largest scales is the inertial subrange, where inertial forces dominate over viscous forces, but not to the extent that energy is generated. In this range, the length scale is determined by the dissipation only, and not by the viscosity (second similarity hypothesis).

There are several popular methods used to determine the total and turbulent stresses in single phase flow. In Reynolds-averaged Navier-Stokes simulations (RANS), the fluid velocity is represented by an average and a fluctuating component, $u = U+u'$. Plugging this definition into the Navier-Stokes equations and taking the time-average

results in an additional term accounting for the stress due to turbulent velocity fluctuations, the Reynolds stress tensor,

$$R_{ij} = \nabla \cdot \rho < \vec{u_i}' \vec{u_j}' > \tag{3.13}$$

Where $\vec{u_i}'$ and $\vec{u_j}'$ are the i-th and j-th components of the fluctuating velocity. To obtain closure of the momentum equations, this quantity must be a function of the average velocity, its derivatives, or other known quantities.

In Large Eddy Simulations (LES), a low-pass filtering process is applied to the momentum equations which results in a residual stress term τ_{ij}^r, in addition to the resolved stress. The residual stress is usually referred to as the sub-grid stress (SGS) because the filtering process is typically equivalent to the spatial discretization (implicit filtering), and must be modeled. That is to say, LES simulations usually (but not always) consider the stresses at or above the grid scale to be resolved.

The most popular models for both LES-SGS modeling and RANS usually rely on the eddy viscosity hypothesis of Boussinesq (1877). As Rivlin (1997) notes, the normal components of total stress of a fluid in turbulent flow are not equivalent to the hydrostatic pressure, as would be the case in a Newtonian fluid. The turbulent kinetic energy, k [$\mathrm{m}^2/\mathrm{s}^2$], represents normal components of total stress in turbulent flow which are present in addition to the hydrostatic pressure. It is sourced through the solution of a transport equation. The Boussinesq hypothesis is written for a compressible system as,

$$\tau_{ij} = \rho \frac{2}{3} k \delta_{ij} - \rho \nu_t \bar{S}_{ij} \tag{3.14}$$

Where τ_{ij} [N/m^2] is the modeled stress, ν_t [m^2/s] is the eddy viscosity, and $\bar{S}_{ij}$ [$\mathrm{m}/(\mathrm{m} \cdot \mathrm{s})$] is the compressible mean rate of strain,

$$\bar{S}_{ij} = \nabla \vec{U} + \nabla \vec{U}^T - \frac{2}{3} I \nabla \cdot \vec{U} \tag{3.15}$$

The validity of the Boussinesq hypothesis has been questioned, and even in homogeneous, isotropic turbulence (i.e. at small length scales), it has been shown to fail due to the direct proportionality between the stress and the strain rate (Schmitt, 2007). Despite this finding, remarkably good results have been achieved for two-phase bubbly flows using the basic linear eddy-viscosity hypothesis. Even so, Speziale (1987) recommended the use of nonlinear eddy viscosity models to avoid potential issues in more complex turbulent flows.

For this work, modeling the Reynolds stress transport equation (RSTE) directly

in the style of Launder et al. (1975) or Speziale et al. (1990) was not considered, even though their models provide an alternative to the Boussinesq hypothesis. The RSTE can only be closed through the use of empirical functions of the mean velocities, Reynolds stresses, and their derivatives (Launder et al., 1975). This closure necessarily requires many tuning parameters. Due to the lack of empirical data for underwater gas well blowouts, obtaining the correct values of the parameters through an optimization study is not possible. Algebraic RSTE, such as the type proposed by Rodi (1993) which are nonlinear eddy-viscosity models, were also not considered because the abundant empirical parameters would still pose a problem.

Predictive accuracy was given preference over computational efficiency in this study. Considering the number of empirical models which must be incorporated in the Euler-Euler model, all of which rely on the accuracy of the turbulence model, any economizing in computational time could end up counterbalanced by a heavy increase in error or a poor prediction of the interphase forces.

The majority of RANS and LES-SGS models have been developed and validated only for single-phase cases. This limits the choice of available models significantly, but there have been some proposed improvements to the single-phase models which incorporate effects due to the second phase. These extensions are discussed in the following sections.

3.2.1 Two-phase RANS Modeling

Several RANS models have been considered for implementation in this work, but only two have been chosen for the comparison study. Unfortunately, few nonlinear eddy-viscosity RANS models have been validated for two-phase flow, so models which rely on the linear hypothesis were used. The mixture $k-\epsilon$ model of Behzadi et al. (2004) and the $k-\epsilon$ model of Simonin and Viollet (1988) have been selected, and are discussed in this section.

The $k-\epsilon$ model is one of the most popularly developed for use in two-phase flow. For single-phase flow it is arguably the most popular RANS model. It was originally conceived by Launder and Spalding (1974) and requires the solution of two transport equations for both k and the eddy dissipation rate, ϵ [m^2/s^3]. The

single-phase turbulent dissipation rate transport equation is,

$$\frac{\partial \rho\epsilon}{\partial t} + \nabla \cdot (\rho\epsilon\vec{U}) - \nabla^2\left(\epsilon\left(\mu + \frac{\mu_t}{\sigma_\epsilon}\right)\right) = C_1\frac{\rho\epsilon}{k}G - \left(\left(\frac{2}{3}C_1 + C_2\right)\rho\epsilon\nabla\cdot\vec{U}\right) - \frac{C_2\rho\epsilon^2}{k} \tag{3.16}$$

Where $C_1 = 1.44$, $C_2 = 1.92$, $C_3 = -0.33$ and $\sigma_\epsilon = 1.3$ are empirical tuning parameters for the standard $k-\epsilon$ model, and the generation term, G, is defined as,

$$G = \nu_t\left(\nabla\vec{U} : dev(2\nabla\vec{U})\right) \tag{3.17}$$

Where $dev()$ indicates the deviatoric. The turbulent kinetic energy transport equation is written as,

$$\frac{\partial \rho k}{\partial t} + \nabla \cdot (\rho k\vec{U}) - \nabla^2\left(k(\mu + \frac{\mu_t}{\sigma_k})\right) = G - \rho\epsilon \tag{3.18}$$

Where $\sigma_k = 1$ is an empirical tuning parameter. The expression for the eddy-viscosity is,

$$\nu_t = C_\mu\frac{k^2}{\epsilon} \tag{3.19}$$

3.2.1.1 Behzadi et al. (2004) $k-\epsilon$ Model

Lee et al. (1989) derived a $k-\epsilon$ model which assumed that the bubble-induced turbulence was proportional to the bubble-induced generation rate of Rodi (1993). This was based on the observation that the length scales of turbulence in the liquid were broken up by the bubble moving through it, and new length-scales were generated. They also observed that the constant parameter $C_\mu = 0.09$ for single-phase flows needed to be artificially increased to 0.8 for two-phase flows.

The model used a term created by Sato and Sekoguchi (1975), who suggested implementing turbulence only in the continuous phase with the addition of a viscosity due to bubble-induced turbulence (BIT) to capture wake effects. It was derived by incorporating a second fluctuating velocity due to bubble agitation. The bubble-induced viscosity is,

$$\mu_{BIT} = c_{\mu,BI}\rho_l\epsilon_{BI} \tag{3.20}$$

Where $c_{\mu,BI} = 0.6$ is a model constant, and

$$\epsilon_{BI} = \alpha_g d|\vec{U_r}| \tag{3.21}$$

The single phase $k-\epsilon$ model combined with the BIT viscosity was used by Díaz et al. (2008) for the liquid phase, while the gas phase eddy viscosity was computed as a multiple of the liquid-phase eddy viscosity based on the densities of the phases and the turbulent Prandtl number. It was shown to be very effective for obtaining both time-averaged and transient results. Contrarily, Zhang et al. (2006) compared the BIT source terms of Pfleger and Becker (2001), and Troshko and Hassan (2001) with the standard $k-\epsilon$ model, all including the addition of the BIT viscosity. They determined that without source terms to account for BIT, a quasi-steady state bubble plume is produced by the $k-\epsilon$ model. For this reason there was no comparison with the basic $k-\epsilon$ model without source terms in the present study.

The $k-\epsilon$ model of Lee et al. (1989) is the basis for the Behzadi et al. (2004) model. A bubble-induced turbulence source term is incorporated in both transport equations of the continuous phase as well as the addition of the Sato and Sekoguchi (1975) bubble-induced turbulent term in the calculation of the eddy viscosity. In `OpenFOAM`, the ϵ transport equation for the Lee et al. (1989) model is implemented as,

$$\begin{aligned}\frac{\partial(\alpha_l\rho_l\epsilon_l)}{\partial t}+\nabla\cdot(\alpha_l\rho_l\epsilon_l\vec{U_l})-\nabla^2\left(\alpha_l\epsilon\left(\mu+\frac{\mu_t}{\sigma_\epsilon}\right)\right)=\alpha_l\rho_l C_2\epsilon_l-C_1\frac{\alpha_l\rho_l\epsilon_l}{k}G \\ -\left(\left(\frac{2}{3}C_1+C_2\right)\alpha_l\rho_l\epsilon_l\nabla\cdot\vec{U_l}\right)-\frac{C_2\alpha_l\rho_l\epsilon_l^2}{k_l}+S_{BIT}\end{aligned} \tag{3.22}$$

Where the constants are the same as for the single-phase version but $\alpha^I=0.3$ and the source term is,

$$S_{BIT}=\frac{\alpha_l\rho_l C_2\epsilon_l G_{bubble}}{k}+max(\alpha^I-\alpha_l,0)min\left(\frac{\epsilon_g}{k_g},\frac{1}{\Delta t}\right)\rho_l(\epsilon_g-\epsilon_l) \tag{3.23}$$

Where,

$$G_{bubble}=\frac{C_p\alpha_g}{d_g}|\vec{U_r}|^{5/3}(C_d|\vec{U_r}|)^{4/3} \tag{3.24}$$

The turbulent kinetic energy transport equation is implemented as,

$$\frac{\partial(\alpha_l\rho_l k_l)}{\partial t}+\nabla\cdot(\alpha_l\rho_l k_l\vec{U_l})-\nabla^2\left(\alpha_l(\mu+\frac{\mu_t}{\sigma_k})\right)=\alpha_l\mu_t G-\frac{2}{3}\rho\epsilon\nabla\cdot\vec{U}-\alpha_l\rho_l\epsilon_l+S_{BIT} \tag{3.25}$$

The source term is,

$$S_{BIT} = \alpha_l \rho_l G_{bubble} + max(\alpha^I - \alpha_l, 0) min\left(\frac{\epsilon_g}{k_g}, \frac{1}{\Delta t}\right) \rho_l (\epsilon_g - \epsilon_l)(k_g - k_l) \tag{3.26}$$

The model was initially intended to be implemented only in the liquid phase. In cases where phase-inversion is likely to occur, this could become problematic if there is no model available in the gas phase. To prevent this, a complementary model was included in the gas phase such that the source terms are applied in only one or the other phase depending on which phase is continuous. In `OpenFOAM` the complementary model is called the `continuousGasKEpsilon` model. It employs a blending function to determine when phase-inversion has occurred, i.e. when $\alpha = \alpha^I$. If the condition is met, the g subscript and l subscripts are switched, and the effective turbulent viscosity in the gas phase is calculated as,

$$\nu_t^{eff} = \frac{1 - min(1, e^{min(\frac{\Theta_l}{\Theta_g}, 50)})}{1 + min(1, e^{min(\frac{\Theta_l}{\Theta_g}, 50)})} \tag{3.27}$$

Where,

$$\begin{aligned} \Theta_l &= \frac{k_l}{\epsilon_l} \\ \Theta_g &= d^2 \frac{\rho_g + C_{VM}\rho_l}{18\rho_l \nu_l} \end{aligned} \tag{3.28}$$

Behzadi et al. (2004) used a similar strategy for the source terms, but used mixture values for k and ϵ instead of switching between models when phase-inversion occurs. The second term of the sources used for the Lee et al. (1989) model is not used, but the first term is the same for both k and ϵ equations. Mass-averaging k, ϵ, ϕ, ρ, ν_t and the generation term and then substituting them into the single-phase $k - \epsilon$ transport equations in place returns the new mixture values, k_m and ϵ_m. These are then converted back to individual phase fields using a turbulence response coefficient defined as,

$$C_{t2} = \sqrt{1 + (C_{t0} - 1) exp(-\alpha_d^f)} \tag{3.29}$$

Where,

$$C_{t0} = \frac{3+\beta}{1+\beta+2\frac{\rho_g}{\rho_l}}, \qquad \beta = \frac{6C_\mu C_d k_l}{4\sqrt{\frac{3}{2}}\rho_l \epsilon_l}$$
$$\alpha_d^f = \alpha_g\Big(180 + \alpha_g(-4.71\times10^3 + 4.26\times10^4\alpha_g)\Big) \tag{3.30}$$

The weighting is first applied to the liquid phase,

$$k_l = k_m\frac{\rho_m}{\alpha_l\rho_l + \alpha_g\rho_g C_{t2}}, \qquad \epsilon_l = \epsilon_m\frac{\rho_m}{\alpha_l\rho_l + \alpha_g\rho_g C_{t2}}, \qquad \nu_{t,l} = C_\mu\frac{k_l^2}{\epsilon_l} \tag{3.31}$$

And then to the gas phase,

$$k_g = k_m C_{t2}, \qquad \epsilon_g = \epsilon_m C_{t2}, \qquad \nu_{t,g} = \nu_{t,l}\frac{C_{t2}\nu_l}{\nu_g} \tag{3.32}$$

3.2.1.2 Simonin and Viollet (1988) Model

Another model that has been used in the literature, this time specifically for unconfined flows, is the model of Simonin and Viollet (1988). They applied the $k-\epsilon$ model in the liquid phase only, with additional source terms in the two transport equations. The source terms they used were,

$$S_k = C_{k2}C_f\alpha_g\rho_L k$$
$$S_\epsilon = C_{\epsilon 2}C_f\alpha_g\rho_L\epsilon \tag{3.33}$$

Where $C_{k2} = C_{\epsilon 2} = 0.6$ are constant coefficients, and the friction coefficient is,

$$C_f = \frac{3}{4d}C_d|U_r| \tag{3.34}$$

Where C_d is the drag coefficient. Sheng and Irons (1993) later altered the source term coefficients slightly for their ladle simulations, and found that changing $C_{k2} = 0.75$ gave a better fit to their experimental data.

3.2.1.3 Wall Functions

Wall functions are used in RANS modeling to account for the boundary layer effects near the walls in a simulation which does not have the near-wall mesh resolution such that the logarithmic behaviour of the flow in these regions is represented. Assuming

equilibrium between the generation and dissipation of turbulent kinetic energy, wall functions calculate the values for ν_t, α_t, k and ϵ within a certain distance from the boundary. For example, the `epsilonWallFunction` in OpenFOAM calculates the value of ϵ and the generation term, G, near the wall as,

$$\begin{aligned} \epsilon &= \frac{1}{W}\sum_{faces}\frac{C_\mu^{3/4}k^{3/2}}{\kappa y} \\ G &= \frac{1}{W}\sum_{faces}\frac{(\nu_t+\nu)|\nabla U|C_\mu^{1/4}k^{1/2}}{\kappa y} \end{aligned} \tag{3.35}$$

Where $\kappa = 0.41$ is the von Karman constant, W is the number of faces and y is the distance from the wall.

The `nutkWallFunction` in `OpenFOAM` calculates the near-wall values of the viscosity as,

$$\nu_t = \begin{cases} \nu(\frac{y^+\kappa}{log(Ey^+)} - 1), & y^+ > y^+_{laminar} \\ 0, & y^+ \leq y^+_{laminar} \end{cases} \tag{3.36}$$

Where $E = 9.8$ is a constant and y^+ is the dimensionless distance from the wall,

$$y^+ = \frac{C_\mu^{1/4}yk}{\nu} \tag{3.37}$$

Typically, the wall functions for the single-phase flows are also applied to two-phase applications (Gosman et al., 1992; Issa, 1988). In the full-scale gas well blowout the only wall in evidence is the seabed, and it is not expected to influence the simulation because it commences at the beginning of the plume region, not at the ocean floor. The validation cases which were chosen in Chapter 4 are also cases in which the flow should be minimally affected by the wall, and the mixing is driven primarily by the gas velocity. For this reason, a Neumann boundary condition, $\frac{\partial k}{\partial n} = \frac{\partial \epsilon}{\partial n} = 0$, was applied at the wall for the k and ϵ transport equations in lieu of wall functions for many of the case studies in this work.

3.2.2 LES Sub-grid Scale Modeling

LES-SGS models typically are quite computationally expensive because the grid size must be close to the size of the turbulent length scales of interest. Considering these length scales can be on the order of the bubble diameter, this could be problematic

for the two-fluid model. In Euler-Euler modeling, one of the basic assumptions is that the bubble size should not be greater than the grid size because the model is not intended to be used for capturing the gas-liquid interface and could encounter large gradients in the phase fraction between adjacent cells.

Using an LES-SGS model to predict dynamic behaviour in a bubble column, where bubbles are usually expected to be quite small, may not be theoretically sound. On an Euler-Euler-appropriate mesh the model might then accidentally be applied to all the length scales of turbulence, like a RANS-type model. This type of validation case would not necessarily be indicative of the model's efficacy on any other case. In modeling the gas well blowout, the size of the cells would necessarily be larger, and this scenario could easily occur if an LES-SGS model were applied without consideration of this fact. Even so, good results have been achieved with LES-SGS models in bubble columns (Deen et al., 2001; Dhotre et al., 2009; Lakehal et al., 2002).

For the large-scale gas blowout plume, a wide variety of bubble regimes could be present which may overshadow the importance of resolving the length scales generated by the smallest bubbles. In multiscale, multiphase scenarios the LES-SGS models may be a far more worthwhile approach, but this has not been demonstrated to date for the Euler-Euler model.

SGS models, unless they are derived for wall-modeling specifically, do not generally represent wall effects properly. In wall-bounded cases (e.g. bubble columns) this could be problematic because a false positive or negative result could be achieved due to the presence of the walls. In application to the large-scale blowout, however, this would not be a problem.

The potential for achieving realizable results in the scale-up from the small validation cases to the large, real-world blowout cases could be increased with the use of a dynamic LES-SGS model, despite the associated computational expense. This has not been explored much in the literature, and as a result was not incorporated in the validation cases. It would be an interesting topic to pursue in future work. The LES-SGS models selected are discussed in the following sections.

3.2.2.1 Two-phase Smagorinsky Models

Most LES-SGS models for two-phase flow modeling used in the literature are linear eddy viscosity models which do not incorporate the turbulent kinetic energy term, assuming the modified pressure will account for all normal components of stress (Ničeno

et al., 2008a). In general, the models which have been used are rooted in the single-phase Smagorinsky (1963) style of eddy viscosity modeling. The single-phase equation for the eddy-viscosity of Smagorinsky (1963) is,

$$\nu_t = C_s^2 \Delta^2 |\bar{S_{ij}}| \tag{3.38}$$

Where Δ is the grid scale filter width, and $C_s = 0.1 - 0.2$ is the Smagorinsky constant. The basic single-phase Smagorinsky (1963) model was compared against the other models in the validation section of this work.

Lakehal et al. (2002) used the single-phase Smagorinsky (1963) model in both phases and compared it to the same with a bubble-induced turbulence term and also to the dynamic Smagorinsky model of Germano et al. (1991). They determined that the Smagorinsky model with no additional bubble-induced turbulent viscosity and a Smagorinsky constant of $C_s = 0.12$ behaved best in their simulations of a small rectangular channel. Their mesh study and others (Milelli et al., 2001b) showed that the optimal results were obtained with $\frac{\Delta}{d_g} = 1.5$, which could result in a very large number of mesh cells if the bubble size is very small. This is usually referred to as the Millelli condition.

The simulations of Milelli et al. (2001a) and Lakehal et al. (2002) are very similar and share many of the same conclusions. Milelli et al. (2001a) recommend that in bubble plumes, application of a bubble-induced turbulence term was likely to be successful for predicting the velocity field in the cases they studied. Zhang (2007) suggested implementing the single-phase model in only the continuous phase with the addition of the Sato and Sekoguchi (1975) BIT term discussed in Section 3.2.1.

Zhang et al. (2006) compared a number of Smagorinsky constants for the same setup and determined that a lower value was appropriate for two-phase flow than for single phase flow. In their simulations, a constant of $C_s = 0.08$ produced the closest mean gas and liquid velocities to their experimental data. This model, with the altered coefficient, was also used to compare results between the RANS and other LES-SGS models in the case studies in this work.

3.2.2.2 One-Equation LES Subgrid Model

Ničeno et al. (2008a) suggested using the one-equation model of Davidson (1997) to account for the loss of information associated with using only the deviatoric part of the sub-grid stress. They also included the BIT viscosity of Sato and Sekoguchi

(1975). The compressible turbulent kinetic energy transport equation is,

$$\frac{Dk}{Dt} = \nabla\left[\alpha_l(\mu + \mu_t)\nabla k\right] + \alpha_l\mu_t G - \alpha_l\rho_l C_\epsilon \frac{k^{3/2}}{\Delta} \tag{3.39}$$

Where $C_\epsilon = 1.05$ and the turbulent viscosity is defined as,

$$\mu_t = C_k \Delta k^{1/2} \tag{3.40}$$

Where $C_k = 0.07$. They compared this model to the dynamic model of Germano et al. (1991) as well as to the model of Davidson (1997) with the Pfleger and Becker (2001) BIT viscosity, and it performed better than both at predicting gas and fluctuating liquid velocity profiles. In their mesh refinement study they concluded that the grid to bubble size ratio obtained by Milelli et al. (2001b) was consistent with their result. This model was used to compare with the other turbulence models in the validation.

3.3 Modeling Bubble Size

The bubble diameter is one of the main bubble properties responsible for the behaviour of the dispersed flow hydrodynamics. It must be carefully approximated, as it directly influences the drag force through the particle Reynold's number. The mass transfer prediction is also highly dependent on the bubble diameter, since the empirical correlations used in this research are multiplied by the area-to-volume ratio, or interfacial area concentration, of the individual bubbles. It has been shown that the bubble size is also a major factor in the lateral movement of bubbles, with smaller bubbles moving toward areas of higher shear, and bigger bubbles moving away (Tomiyama et al., 2002b).

If it is assumed that all the bubbles remain at an initially assigned approximate size, or that their only volume change is due to the decrease in pressure as they move up the water column, this could be an extreme oversimplification in certain cases. Bubbles tend to break apart and recombine, and their tendency to do so is dependent on many factors, including the flow regime, the surface tension, and the viscous stresses in the continuous phase (Kocamustafaogullari and Ishii, 1995). Many breakup and coalescence rates have been determined through mechanistic modeling, and have been implemented as source or sink terms to a conservation equation for the number of bubbles present in each cell.

The choice of equation itself must be based on one of the known conservative

quantities and cannot be highly nonlinear or anisotropic, but beyond these requirements, is relatively inconsequential in acquiring an acccurate result. The strength of the approach, in terms of realizability, is primarily determined by the breakup and coalescence models, which can only be evaluated through comparison to experimental data.

3.3.1 Population Balance Modeling

Population balance models (PBM) track the bubble size distribution over time. The most popular of these are the class method (CM), which identifies discrete bubble size classes and tracks their populations (and velocities, in the inhomogeneous method) over time, and the method of moments (MOM), which requires the solution of multiple transport equations to track the moments of the bubble size distribution, such as the mean, variance, and skew. The CM has some of the same downsides as the Lagrangian particle tracking models; it can be very slow when a large number of classes must be solved for.

In the simulations of Selma et al. (2010), it was concluded that the direct quadrature MOM (DQMOM) (Marchisio and Fox, 2005) with three moments and the multiple size group (MUSIG) (Lo, 1996) CM with 15+ classes are equivalently accurate, but as the number of classes is increased, the MOM becomes comparatively more computationally efficient. This result could change with the application of different breakup and coalescence models, or by changing the turbulence model, as the former models are often proportional to the cube root of the turbulent dissipation rate. The MOM may be more computationally efficient but also can be disadvantageous. These methods require a moment inversion algorithm for back-calculating the bubble size distribution. According to Marchisio and Fox (2013), moment-inversion algorithms must have four basic properites which can be difficult to meet if the particle density function requires higher-order moments to attain realizability.

Population balance modeling of any kind is limited in its range of applicability, which can only be expanded through validation on different cases and tuning of the models. The bubble sizes expected in the large-scale gas well blowout occur at many scales, and the domain is not wall-bounded. It is not common to see PBM used in unconfined, multiscale bubble plumes, and it is unknown whether they would improve accuracy in cases such as the blowout which cannot be compared to experimental data.

Lab-scale experiments of unconfined flow can be used to validate PBM models, but their applicability to large-scale models is still questionable. For the purposes of

this research, the interfacial area transport equation was used to attempt to expand the range of applicability of PBM to unconfined bubbly flow at the lab scale.

3.3.2 The Interfacial Area Transport Equation

The interfacial area transport equation (IATE) was based on the population balance model concept, and was developed specifically with bubbly flow systems in mind unlike other methods (Kocamustafaogullari and Ishii, 1995). The IATE method solves for the interfacial area concentration, and returns an effective bubble diameter in each cell which can then be used by the empirical models for the interfacial forces and mass transfer rates. The one-group IATE treats all the bubbles as if they were in the spherical/distorted regimes, which can be a valid assumption in many flow scenarios. This formulation only solves one transport equation, and is not computationally expensive.

In cases where large-cap, churn-turbulent, or slug bubble regimes are present, the one-group IATE will no longer be sufficient. A second group was introduced to account for these regimes, resulting in the creation of a two-group IATE (Ishii and Kim, 2004). Although this should add additional accuracy, inter-group transfer terms must be incorporated into the source terms of the equations to account for bubbles which enter or exit their original regime. These terms can reduce accuracy if the number of bubbles which could coalesce and/or break up is restricted to some maximum. For example, uniform binary breakup restricts the number of daughter bubbles to two identical bubbles, but this may not be representative of physical reality.

The two-group method has promise for the scaled-up gas well blowout case, but has not been validated in the literature for a wide range of expected bubble sizes or in large geometries which are unconfined. Furthermore, the implementation of a two-group IATE method would necessitate the prediction of the velocity of the bubbles in the second group (Smith et al., 2012b). The `twoPhaseEulerFoam` solver could be altered to include a third momentum equation, but the coupling between the equations through the force terms would have to reflect the change in regime and be appropriately tuned, which is beyond the scope of this work.

For this study, the one-group IATE method was employed in an unconfined flow system. The available source terms for the model were not developed for very large systems, so their applicability is in question. At the assumed bubble sizes of a well blowout, the drag coefficient may be effectively constant, so should not have a great impact on the flow dynamics.

The one-group IATE is derived by consideration of the bubble number density equation (without phase change) as described by Ishii and Hibiki (2010),

$$\frac{\partial f}{\partial t} + \nabla \cdot (f\overrightarrow{U_g}) + \frac{\partial}{\partial t}\left(f\frac{dV_b}{dt}\right) = \sum_j S_j \tag{3.41}$$

Where $f(V_b, x, t)$ is the number density distribution, V_b [m^3] is the bubble volume, and S_j are the source terms. This equation is multiplied by the interfacial area, A_i, and integrated between the minimum and maximum bubble volumes of the group,

$$\int_{V_{b,min}}^{V_{b,max}} \left[A_i\frac{\partial f}{\partial t} + A_i\nabla\cdot(f\overrightarrow{U_g}) + A_i\frac{\partial}{\partial t}\left(f\frac{DV_b}{Dt}\right)\right]dV_b = \int_{V_{b,min}}^{V_{b,max}} A_i\left(\sum_j S_j\right)dV_b \tag{3.42}$$

The interfacial area concentration is given by,

$$a_i(x,t) = \int_{V_{b,min}}^{V_{b,max}} f A_i dV_b \tag{3.43}$$

This simplifies the first two terms on the left side of Equation 3.42 to be,

$$\frac{\partial a_i}{\partial t} + \nabla \cdot (a_i\overrightarrow{U_g}) \tag{3.44}$$

The third term of Equation 3.42 is slightly more difficult to prove. Rewriting $V_b = x$, and $A_i(V_b) = g(x)$, the equation becomes,

$$\int_{V_{b,min}}^{V_{b,max}} g(x)\frac{\partial}{\partial t}\left(f\frac{dx}{dt}\right)dx \tag{3.45}$$

Through partial integration,

$$\int_{V_{b,min}}^{V_{b,max}} g(x)\frac{\partial}{\partial t}\left(f\frac{dx}{dt}\right)dx = \left[f\frac{Dx}{Dt}g(x)\right]_{V_{b,min}}^{V_{b,max}} - \int_{V_{b,min}}^{V_{b,max}} \frac{dg(x)}{dt}\left(f\frac{Dx}{Dt}g(x)\right) \tag{3.46}$$

Recalling that $f(V_{b,min}) = f(V_{b,max}) = 0$ because the bubble size only exists between $V_{b,min}$ and $V_{b,max}$, the first term on the right hand side is zero. Rearranging the interfacial area to be dependent on bubble volume gives,

$$A_i = g(x) = \left(\frac{6V_b}{\pi}\right)^{\frac{2}{3}}\pi \tag{3.47}$$

And its derivative is,

$$\frac{\partial g(x)}{\partial t} = \frac{2}{3x} g(x) \tag{3.48}$$

Substituting everything into Equation 3.42 and rewriting in terms of V and A_i,

$$\int_{V_{b,min}}^{V_{b,max}} A_i \frac{\partial}{\partial t}\left(f \frac{dV_b}{dt}\right) dV_b = -\int_{V_{b,min}}^{V_{b,max}} \frac{2}{3V_b} \frac{DV_b}{Dt} f A_i \tag{3.49}$$

Which can be rewritten as,

$$-\int_{V_{b,min}}^{V_{b,max}} \frac{2}{3V} \frac{DV_b}{Dt} f A_i = -\int_{V_{b,min}}^{V_{b,max}} \frac{2}{3\alpha_g} \frac{D\alpha_g}{Dt} f A_i \tag{3.50}$$

It is assumed at this point that the change in the phase fraction is independent of the volume of the bubbles, i.e. $\frac{1}{\alpha_g}\frac{D\alpha_g}{Dt} \neq f(V_b)$. Ultimately there is some dependence on the bubble volume, in that the substantial derivative of the phase fraction is equal to the interphase mass transfer rate, which relies on the interfacial area concentration. This could be a problematic assumption for this reason. Finding a numerical solution of the integral could be a potential workaround for this approximation, but this extension was not attempted in the present study.

Continuing the derivation, from the continuity equation it is known that the substantial derivative of the phase fraction is equal to the dilatation rate,

$$\frac{\partial \alpha_g}{\partial t} + \vec{U_g} \cdot \nabla \alpha_g = \nabla \cdot \vec{U_g} \tag{3.51}$$

Adding the dilatation rate into Equation 3.42 results in,

$$\frac{\partial a_i}{\partial t} + \nabla \cdot (a_i \vec{U_g}) = \frac{2a_i}{3\alpha_g} \nabla \cdot \vec{U_g} + \int_{V_{b,min}}^{V_{b,max}} A_i \left(\sum_j S_j\right) dV_b \tag{3.52}$$

The source terms are written assuming that the decrease or increase in interfacial area is always associated with either the doubling or halving respectively of a spherical bubble volume, i.e. $\Delta A_i = \frac{1}{3} A_i$. Since $A_i = \frac{a_i}{n}$, where n is the number density of bubbles equal to $n = \Psi \frac{a_i^3}{\alpha_g^2}$, where $\Psi = \frac{1}{36\pi}$ is the sphericity of spherical bubbles, the source terms become,

$$\int_{V_{b,min}}^{V_{b,max}} A_i \left(\sum_j S_j\right) dV_b = \sum_j S_j \Delta A_i = \sum_j \frac{1}{3\Psi} \left(\frac{\alpha_g}{a_i}\right)^2 S_j \tag{3.53}$$

The final equation for the IATE, assuming spherical bubbles, is written as,

$$\frac{\partial a_i}{\partial t} + \nabla \cdot (a_i \overrightarrow{U_g}) = -\frac{2a_i}{3\alpha_g} \nabla \cdot \overrightarrow{U_g} + \sum_j \frac{1}{3\Psi} \left(\frac{\alpha_g}{a_i} \right)^2 S_j \tag{3.54}$$

The processes which contribute to the fluid particle breakup and coalescence were outlined by Kocamustafaogullari and Ishii (1995). Typically, bubble breakup is considered to be mostly driven by turbulent eddies and interfacial stability, which are usually lumped together into a single turbulent interaction term. The turbulent interaction term is an additive term because the interfacial area is greater for the same volume if there are more bubbles, and by extension, more breakup. The bubble coalescence is usually taken to be a product of random collisions and wake entrainment, which is highly dependent on the turbulent fluctuations as well. The bubble coalescence terms are sink terms because random collisions and wake entrainment usually result in larger bubbles, reducing the area-to-volume ratio.

The one-group IATE has been shown by Ishii et al. (2005) to be accurate for pipe diameters between $5.08 - 15.2$ cm in the bubbly flow regime with small bubbles, having error less than $\pm 20\%$ when using the source and sink terms of Sun et al. (2004). For large diameter pipes of 10.2 cm and 20 cm, Tian et al. (2015) found that the models of Sun et al. (2004) gave the best results for the one-group IATE, along with that of Smith et al. (2012b) and Ishii and Kim (2001) which all had error less than ± 10 % when compared to interpolated experimental values.

Smith et al. (2012a) indicated that, since most of the models are not dependent on the channel geometry, there is no obvious impediment to applying them to different geometries. Some studies, such as Hansen (2009), have used the one-group IATE model in a bubble column with the source terms of Wu et al. (1998) and Moilanen et al. (2008). Acher (2015) has compared the IATE model kernels used by Hansen (2009) with DQMOM, however there were very few bubble size data points. In general the IATE model was shown to predict a lower bubble size near the walls than DQMOM.

The IATE model has promise for large-scale cases with larger bubbles (< 1 cm) where the drag coefficient is likely to be fairly constant, but where the mass transfer can be highly influenced by the effective bubble diameter in each cell. It has been applied in this work to attempt to determine its efficacy in unconfined flow, however additional modifications to the source terms may be required for larger bubbles in future work.

3.3.3 `OpenFOAM` Implementation of the IATE Model

In `OpenFOAM`, the model was written based on the interfacial curvature $\kappa_i = \frac{6}{d}$ in lieu of the interfacial area concentration $a_i = \frac{6\alpha_g}{d}$. The equation is only slightly different once the change is worked through, and is written as,

$$\frac{\partial \kappa_i}{\partial t} + \overrightarrow{U_g} \cdot \nabla \kappa_i = -\frac{\kappa_i}{3\alpha_g} \nabla \cdot \overrightarrow{U_g} + \sum_j \frac{1}{3\alpha_g \Psi} \left(\frac{\alpha_g}{a_i} \right)^2 S_j \tag{3.55}$$

The source terms are written to be implicit in κ_i. Since $\kappa_i = \frac{a_i}{\alpha_g}$, the summed source and sink terms envelope the preceeding coefficients and become,

$$\sum_j \frac{1}{3\alpha_g \Psi} \left(\frac{\alpha_g}{a_i} \right)^2 S_j = \kappa_i \sum_j \frac{1}{3\Psi} \frac{\alpha_g^2}{a_i^3} S_j \tag{3.56}$$

The number of bubbles is $n = \Psi \frac{a_i^3}{\alpha_g^2}$, so the coefficient to the sources becomes $\frac{1}{3n}$. In this study, the breakup and coalescence models of Wu et al. (1998) have been implemented in the code. This was one of the original source term models for the IATE. The turbulent interaction source is,

$$S_{TI} = C_{TI} \frac{n|\overrightarrow{U_t}|}{d} \left(1 - \frac{We_{cr}}{We} \right)^{1/2} exp(-\frac{We_{cr}}{We}) \tag{3.57}$$

The equation is valid for $We > We_{cr}$ and does not exist otherwise. $C_{TI} = 2.0$ is a constant, $We_{cr} = 0.18$ is the critical Weber number, where the Weber number is defined as,

$$We = \frac{\rho_l |\overrightarrow{U_r}|^2 d}{\sigma} \tag{3.58}$$

Where σ [N/m] is the surface tension, and the magnitude of the terminal velocity is,

$$|\overrightarrow{U_t}| \approx 1.4(\epsilon_l d)^{1/3} \tag{3.59}$$

The random coalescence sink term is given as,

$$S_{RC} = -C_{RC} \left(\frac{n^2 |\overrightarrow{U_t}| d^2}{\alpha_{max}^{1/3} (\alpha_{max}^{1/3} - \alpha_g^{1/3})} \right) \left(1 - exp\left(-C \frac{\alpha_{max}^{1/3} \alpha_g^{1/3}}{\alpha_{max}^{1/3} - \alpha_g^{1/3}} \right) \right) \tag{3.60}$$

Where $\alpha_{max} = 0.8$, $C_{RC} = 0.0565$ and $C = 3.0$ are constants.

Finally, the wake entrainment sink term is given by,

$$S_{WE} = -C_{WE} C_D^{1/3} n^2 d^2 |\overrightarrow{U_r}| \tag{3.61}$$

Where $C_{WE} = 0.151$ is a constant, the drag coefficient is found using a combination model of Tomiyama et al. (1998) for a pure system,

$$C_D = \begin{cases} \frac{16}{Re}(1 + 0.15Re^{0.687}) & \text{Spherical Bubbles} \\ \frac{48}{Re} \quad Re > 43.4 & \text{Spherical Bubbles} \\ \frac{8Eo}{3(Eo+4)} & \text{Non} - \text{Spherical Bubbles} \end{cases} \tag{3.62}$$

And the relative velocity is approximated to avoid iterating with the drag coefficient,

$$|\overrightarrow{U_r}| = (1 - \alpha_g)^{1.75} \sqrt{2} \left(\frac{\sigma g (\rho_l - \rho_g)}{\rho_l^2} \right)^{1/4} \tag{3.63}$$

The IATE is treated as a diameter model in `twoPhaseEulerFoam`, which is solved at the beginning of each new outer PIMPLE loop.

3.4 Mass Transfer Modeling

The new mass transfer algorithm for the solver is capable of selecting a number of mass transfer models for the Sherwood number to determine the volumetric mass transfer coefficient. To verify that the algorithm was working as expected, a case which used a constant Sherwood number was executed in Chapter 6 along with a case which used a model. Several applicable mass transfer models were considered.

One of the most popular models is that of Frössling (1938) which was derived for evaporation from falling liquid droplets. It is written as,

$$Sh = 2 + 0.552 Re^{1/2} Le^{1/3} Pr^{1/3} \tag{3.64}$$

Where Pr is the Prandtl number, Le is the Lewis number, and Sh is the Sherwood number defined as,

$$Pr = \frac{\nu_l}{\alpha_t}, \quad Le = \frac{\alpha_t}{D_{ij}}, \quad Sh = \frac{k_m d}{D_{ij}} \tag{3.65}$$

Where k_m [m/s] is the convective mass transfer coefficient (not volumetric). The volumetric mass transfer coefficient is simply the mass transfer coefficient multiplied by the interfacial area concentration, as previously noted ($k_{m,i}$). The dimensionless

numbers were all calculated using the molecular transport coefficients.

The Frössling correlation has been widely used for $Re = 2 - 2000$. For very large bubbles reaching their terminal velocities, this range could be too low, but should remain appropriate for the cases discussed in this work.

Akita and Yoshida (1974) experimentally derived a correlation for the Sherwood number in a bubble column at varying pressures. For Bond numbers between $0.1-100$ they found,

$$Sh = 0.5 Sc^{1/2} Ga^{1/4} Bo^{3/8} \tag{3.66}$$

Where the Schmidt, Galilei and Bond numbers are defined as,

$$Sc = \frac{\nu_l}{D_{ij}}, \quad Ga = \frac{gd^3}{\nu_l^2}, \quad Bo = \frac{gd^2\rho_l}{\sigma} \tag{3.67}$$

Hughmark (1967) determined that for swarms of bubbles in a bubble column, the Sherwood number is,

$$Sh = 2 + 0.0187 Re^{0.779} Sc^{0.546} \left(\frac{dg^{1/3}}{D_{ij}^{2/3}} \right)^{0.116} \tag{3.68}$$

For much larger Reynolds numbers, Griffith (1960) provides a review of available models and their ranges of applicability. The three mass transfer models have been compared against each other at their terminal velocities (determined by the Kolev (2007) drag model). Figure 3.4 shows the change in $k_{m,l}$ value with bubble diameter.

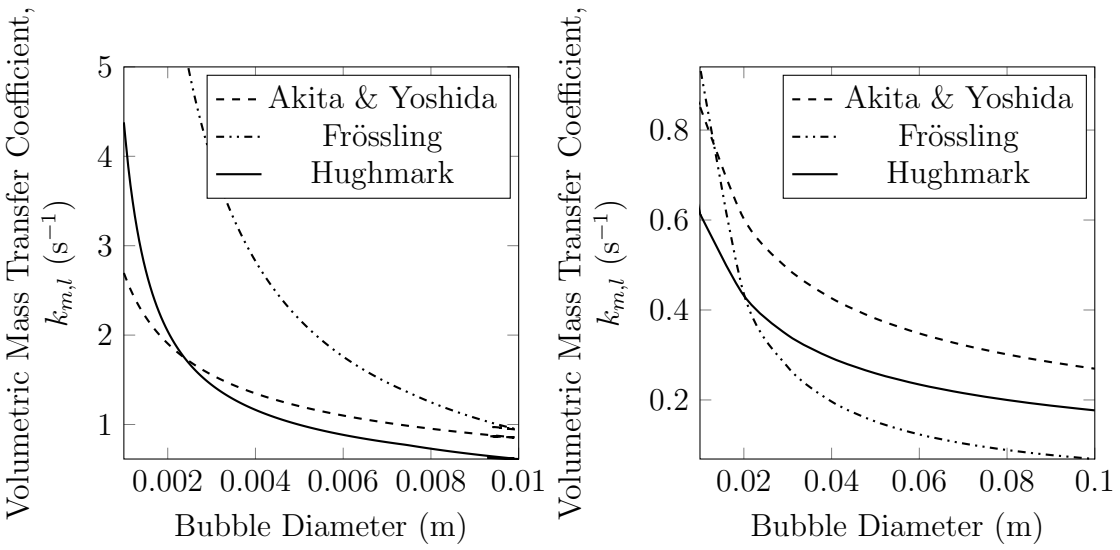

Figure 3.4: Volumetric mass transfer coefficient ($k_{m,l}$) vs. bubble diameter at terminal velocity. Small (left) and larger (right) bubble diameters. Liquid properties were for water at 298 K, and gas properties were for oxygen at STP, $\alpha_g = 0.3$.

Above a 5 cm bubble diameter the $k_{m,l}$ values become very close in value, and stop changing as radically as at the lower bubble sizes. In the large-scale case the bubbles are expected to be quite large, so the $k_{m,l}$ value will be less reliant on the interfacial area concentration in that range, and the mass transfer coefficient should stay relatively constant. The Frössling correlation gives the lowest $k_{m,l}$ values of the three models in the larger bubble size range, and highest in the lower size range. It should give the upper limit on dissolution in the smaller bubble sizes up to 2 cm. Mass transfer models which were not purely empirical, such as the surface renewal model or penetration theory, were not used in this study in order to reduce the reliance on the turbulence and/or bubble size model.

3.5 Finite Volume Methods

The numerical methods which were used in the validation cases were kept consistent for all validations. The following sections give details on the discretization schemes and the linear equation solvers which were used.

3.5.1 Interpolation Schemes

The convective terms were discretized in `OpenFOAM` according to Table 3.2.

Table 3.2: Convection schemes

Term	**Scheme**
$\nabla \cdot \vec{\phi}\alpha$	`Gauss vanLeer`
$\nabla \cdot \alpha\rho\vec{\phi}\vec{U}$	`Gauss limitedLinearV 1`
$\nabla \cdot \vec{\phi}\vec{U}$	`Gauss limitedLinearV 1`
$\nabla \cdot \alpha\rho\vec{\phi}e$	`Gauss limitedLinear 1`
$\nabla \cdot \alpha\rho\vec{\phi}K$	`Gauss limitedLinear 1`
$\nabla \cdot \alpha\vec{\phi}P$	`Gauss limitedLinear 1`
$\nabla \cdot \alpha\rho\vec{\phi}k$	`Gauss limitedLinear 1`
$\nabla \cdot \alpha\rho\vec{\phi}\epsilon$	`Gauss limitedLinear 1`
$\nabla \cdot \alpha\rho\vec{\phi}Y$	`Gauss limitedLinear 1`
$\nabla \cdot \alpha\rho\vec{\phi}\kappa_i$	`Gauss limitedLinear 1`
$\nabla \cdot (\alpha\rho\nu_{eff}\vec{U})$	`Gauss linear`
$\nabla \cdot \left[\left(\alpha\rho\nu_{eff}\left(\nabla\vec{U}^T - \frac{2}{3}tr(\nabla \cdot \vec{U})I\right)\right) + \alpha\rho\frac{2}{3}kI\right]$	`Gauss linear`

`Gauss vanLeer` indicates the use of the Van Leer (1974) flux-limiting total variation diminishing (TVD) scheme. It is a weighted average of the upwind and central finite volume schemes with a limiter function of,

$$\phi(r) = \frac{r + |r|}{1 + |r|} \quad \lim_{r\to\infty} \phi(r) = 2 \tag{3.69}$$

Where r is the ratio between the upwind and downwind gradients. Gauss limitedLinear and limitedLinearV are also flux-limiting TVD schemes which discretize scalar and vector arguments respectively. The limiter function is similar to that of the well-known MUSCL scheme and is given by,

$$\phi(r) = max\left[min\left(\frac{2r}{k}\right), 0\right] \tag{3.70}$$

Where $k = 1$ is the specified flux limiter coefficient. `Gauss linear` indicates the symmetric scheme. Using the TVD schemes ensures that monotonicity is preserved (Harten, 1983) which is important for the tightly coupled `twoPhaseEulerFoam` solver. All other terms were discretized according to type, and all terms of that type used the same scheme. The schemes which were selected in `OpenFOAM` are summarized in Table 3.3.

Table 3.3: Finite volume schemes

Time Discretization	`euler`
Gradient Discretization	`Gauss linear`
Laplacian Discretization	`Gauss linear uncorrected`
Face Interpolation	`linear`
Surface Normal Gradient Discretization	`uncorrected`

The Laplacian and surface normal gradient terms were discretized using a symmetric scheme with no correction for non-orthogonality in all orthogonal meshes. Some of the meshes detailed in chapters 4-6 were cylinders, and necessarily had some non-orthogonality. For those cases, a correction was applied. The phase continuity equation uses the MULES solver in lieu of forward Euler. The selected combination of schemes provided stability for the validation cases in this work, and were chosen on this basis.

3.5.2 Linear Equation Solvers

MULES was used for the solution of the phase continuity equation, as previously mentioned in Chapter 2. The MULES solution is calculated as,

$$\psi^{i+1} = \frac{1}{\varphi\frac{1}{\Delta t} + Sp}\left(\varphi\psi^{i}\frac{1}{\Delta t} + Su - \sum_{faces}\frac{(\psi(\Phi\psi)}{V_{cell}}\right) \tag{3.71}$$

Where ψ is the variable to be solved for, Su indicates an explicit source term, Sp indicates an implicit source term, φ is the multiplier to ψ in the time derivative and $(\Phi\psi)$ represents any additional convective terms in the equation for ψ, treated explicitly. The final sum indicates a linear interpolation of a surface field to the cell centers. The MULES solver also limits the discretization of the convective terms like the TVD schemes.

The pressure equation was solved using the geometric-algebraic multigrid (GAMG) solver with a diagonal-based incomplete Cholesky (DIC) smoother. All other fields were solved with the Gauss-Seidel method except for the species equations which were solved using the preconditioned bi-conjugate gradient (PBiCG) method with the simplified diagonal-based incomplete L-U (DILU) preconditioner. These methods are described in detail elsewhere (Hestenes and Stiefel, 1952; Moukalled et al., 2016). The linear equation solvers which were used were kept consistent throughout

the validation cases in this work unless otherwise stated.

3.6 Blending

The `twoPhaseEulerFoam` algorithm was built to accept phase-inversion. For this reason, models in the gas and liquid must be specified for both the case where gas is the dispersed phase and the case where liquid is the dispersed phase. In regions where the dispersed and continuous phase are more difficult to determine, for instance in the case where $\alpha_g = 0.5$, a blending model can be implemented. This allows for the coefficients of the interphase forces to have a value which corresponds to a partly continuous or partly dispersed phase instead of fully continuous or fully dispersed phase. The blending models can also help stabilize the solution in regions where an interface, such as a free surface, occurs.

There are three blending models that can be chosen: None, Linear, or Hyperbolic. Each of the models applies a weighted average,

$$k_{blended} = (f_1 - f_2)k + f_1 k_{12} + f_2 k_{21} \tag{3.72}$$

Where k is an unordered pair (for an undefined continuous phase) if it exists, k_{12} is the coefficient if phase 1 is dispersed, k_{21} is the coefficient if phase 2 is dispersed, and f_1 and f_2 are weights. The weights are defined for the linear model as,

$$\begin{aligned} f_1 &= min\left(max\left(\frac{\alpha_1 - \alpha_{1,max}}{\alpha_{1,min} - \alpha_{1,max}}, 0\right), 1\right) \\ f_2 &= min\left(max\left(\frac{\alpha_{2,min} - \alpha_2}{\alpha_{2,min} - \alpha_{2,max}}, 0\right), 1\right) \end{aligned} \tag{3.73}$$

Where α_{min} is the volume fraction at which the phase is fully dispersed, and α_{max} is the volume fraction at which the phase is fully continuous. To avoid using an intermediate model, theses values can be the same for both phases (i.e. the first term vanishes). For the no-model blending, the weights are,

$$\begin{aligned} f_1 &= \alpha_1 \\ f_2 &= \alpha_2 \end{aligned} \tag{3.74}$$

And for the Hyperbolic model,

$$f_1 = \frac{1 + tanh(\frac{4}{s}(\alpha_1 - \alpha_{1,min}))}{2}$$
$$f_2 = \frac{1 + tanh(\frac{4}{s}(\alpha_{2,min} - \alpha_2))}{2} \tag{3.75}$$

Where s is an adjustable constant. The three blending methods are demonstrated in Figure 3.5 for arbitrary coefficient values of $k = 1$, $k_{12} = 0.1$ and $k_{21} = 5$ with a symmetric α_{min} and α_{max}.

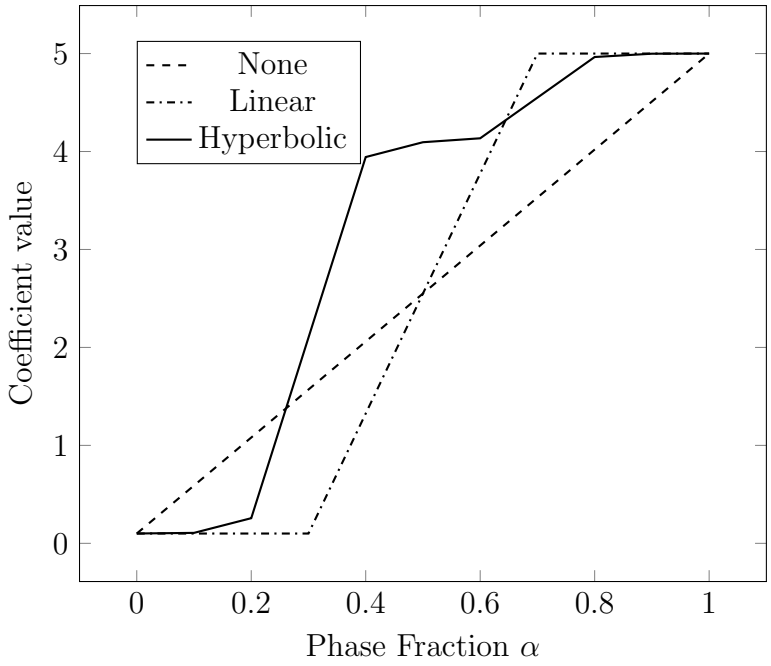

Figure 3.5: The three blending models for values of $\alpha_{1,min} = 0.3$, $\alpha_{1,max} = 0.7$, and $s = 0.5$.

For the purposes of the current study, the linear blending model was sufficient. The blended region was minimized such that each case was unlikely to have any blended regions.

Chapter 4

Turbulence Model Study

In two-phase flow, the turbulence and interphase forces are strongly coupled, so validating the turbulence models separately is theoretically problematic. Despite the demonstrated effectiveness of turbulence models in many applications, foundationally they are not verifiable and can only be labeled either realizable or not based on validation against experimental data. In combination with different interphase force models, the results also may vary. For this reason the models described in Chapter 3 are consistent throughout the validation studies in this chapter.

Optimization of all models is practically impossible, particularly when validating against small-scale experiments for potential use on a multiscale simulation such as the gas well blowout case. Although it may be possible to isolate certain forces in experiment and validate models against the results, the turbulence model may ultimately not work well with other models, or it may work better. In this chapter, several turbulence models were compared to experimental data to investigate the effect of the turbulence model on simulations of a bubble plume.

4.1 Fluid Properties

The fluid properties, which were used for all the simulations in this chapter and in Chapter 5 are given in this section to avoid ambiguity. Table 4.1 gives the relevant fluid properties for the gas species in the simulations. The ideal gas law was used to determine the density for all gas-phase species while the liquid phase was incompressible. Other properties were calculated at the temperature condition given in the study, but were not temperature dependent in the simulations.

Table 4.1: Gas phase species properties

Species	**Molecular Weight**	**Viscosity**	**Specific Heat Capacity**	**Prandtl Number**
Air	28.9 g/mol	1.7×10^{-5} Pa $\cdot$ s	1004 J/kg $\cdot$ K	0.7

The temperature for all the validation simulations was 20°C. The properties of each species in the liquid phase are given in Table 4.2.

Table 4.2: Liquid phase species properties

Density	**Molecular Weight**	**Viscosity**	**Specific Heat Capacity**	**Prandtl Number**
1000 kg/m^3	18 g/mol	1×10^{-3} Pa $\cdot$ s	4293 J/kg $\cdot$ K	8.34

4.2 Sheng and Irons (1993) Experiment

An experiment which was expected to maintain a fairly constant bubble size was used for comparing turbulence models in this work. As the bubble size model is likely to improve the prediction, determining appropriate turbulence models to use without it first is sensible. An absolute determination of the best turbulence model to use for bubbly plumes with all force models and over all length-scales is not realistic. For this study, a bubble plume produced in a model ladle was simulated because it was one of the largest available bubble plume data sets.

The results of Sheng and Irons (1993) were used to compare the turbulence models. They showed that coalescence was negligible at a gas flowrate of 5×10^{-5} m^3/s from the nozzle in their study. The flowrate chosen also resulted in a relatively high inlet velocity, which is desirable when comparing models for eventual application to a scenario where the inlet velocity is also high, and mixing is due solely to the gas injection, such as for the full-scale gas well blowout. The experiment was also chosen because the gas inlet was a single sparger instead of a porous or perforated plate. This allowed for the analysis of the gas spread, which is important when considering the large-scale gas well blowout scenario.

The study of Lou and Zhu (2013b) replicated the ladle of Sheng and Irons (1993) with their own suite of interphase force and turbulence models. They determined that the Kolev (2012) drag model in conjunction with the Lopez de Bertodano (1998) model with $C_{TD} = 0.1$ and $C_L = 0.1$ gave the optimal result. Since these details were not included in the Sheng and Irons (1993) paper, which also included a turbulence model comparison, the force models used in their study were used in the present study as well. The Sheng and Irons (1993) study compared five RANS turbulence models and determined that their tuned model, that of Simonin and Viollet (1988) with $C_k = 0.75$, gave them the best result. Sheng and Irons (1993) assumed axial symmetry and gave 2-D simulation results, while Lou and Zhu (2013b) gave 3-D results.

One of the most important aspects of the full-scale well blowout is the amount of

lateral spreading of the gas. Aside from the lift and turbulent dispersion forces, turbulence is primarily responsible for the lateral distribution of the gas phase fraction.

The experimental setup in Sheng and Irons (1993) was a model ladle, 500 mm in diameter with a flush-mounted 4 mm diameter nozzle at the centre bottom. The ladle was 760 mm high with a free surface at 420 mm, surrounded by a water-filled box to prevent distorion. Five, 3 mm measurement slots were cut into the wall of the cylinder, as shown in Figure 4.1. Measurements were taken with a combined laser Doppler anemometer (LDA) and electrical probe for the measurement of bubble velocities and phase fractions.

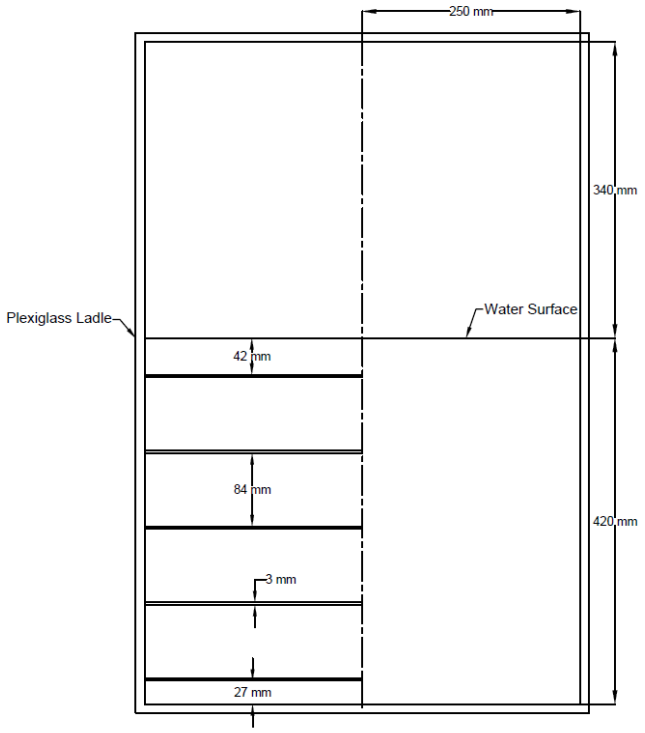

Figure 4.1: The vertical cross-section of the model ladle of Sheng and Irons (1993).

Since the bubble diameter was not given in Sheng and Irons (1993), the formula of Sano and Mori (1976) was used to estimate the initial diameter of bubbles exiting a nozzle, as in Lou and Zhu (2013b), in the simulations in this chapter,

$$d = \left[\left(\frac{6\sigma d_o}{\rho_l g} \right)^2 + 0.0248 (Q^2 d_o)^{0.867} \right]^{1/6} \tag{4.1}$$

Where d_o [m] is the nozzle diameter and Q [m^3/s] is the volumetric flowrate. The

bubble diameter obtained for a flowrate of 5×10^{-5} m^3/s was 0.014 m. This value is consistent with the range of bubble sizes in the column, between $5 - 10$ mm, reported by Sheng and Irons (1993) and also would correspond to a bubble frequency of around 10 Hz as observed by Hoefele and Brimacombe (1979) and Coppock and Meiklejohn (1951).

4.3 Case Setup for the Turbulence Study

The computational domain was taken to be cylindrical with $D \times z = 65 \times 40$ cells (max $\frac{\Delta}{d_g} = 0.934$, min $\frac{\Delta}{d_g} = 0.35$). The nozzle was represented by 1 cell on the bottom surface, totalling approximately the nozzle diameter (Area $= 1.60 \times 10^{-5}$ m^2). The domain was meshed as a central rectangle with four curved blocks surrounding it, as shown in Figure 4.2. The blocks were graded in the z-direction with a first-to-last cell expansion ratio of 1:2. The majority of the plume was contained near the center of the ladle, so it was more refined than the rest of the domain, which was kept relatively fine to capture the liquid velocity recirculation.

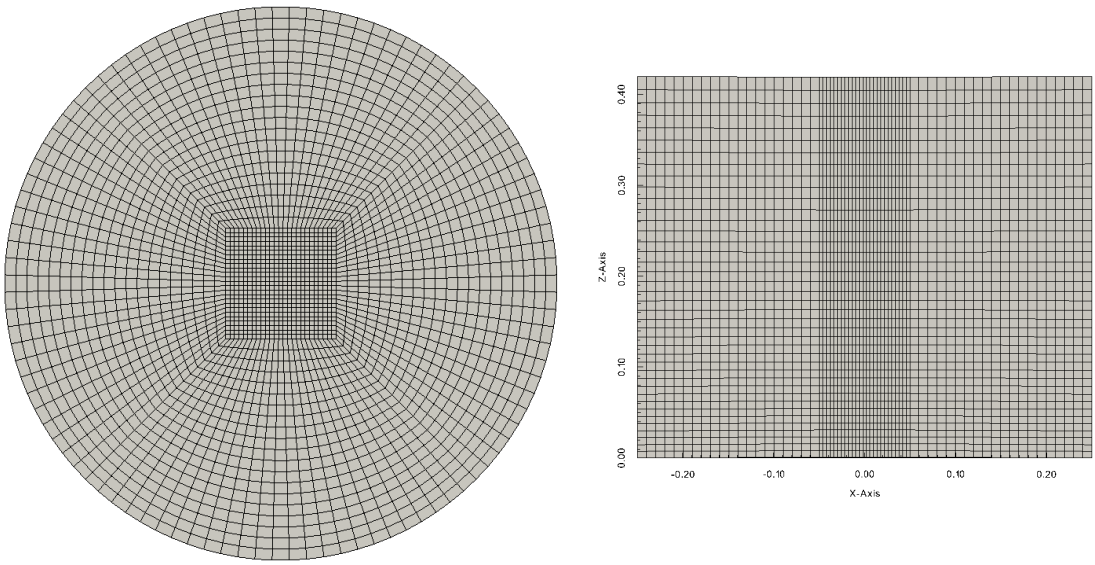

Figure 4.2: The computational domain for the turbulence model comparison cases. Top view (left) and cross-section (right).

The boundary conditions for all the simulations are summarized in Table 4.3. Wall functions were not used for the k and ϵ equations. Some of the `OpenFOAM` terminology for the boundary conditions is explained here. The `inletOutlet` condition determines the boundary condition based on the direction of the flux, setting the

boundary condition to a Neumann condition $\frac{\partial \xi}{\partial n} = 0$ if it is out of the domain and a Dirichlet condition $\xi = 0$ if it is inward unless otherwise specified in the table. The `fixedFluxPressure` condition sets the modified pressure gradient based on the flux at the boundary. The `prghPressure` condition uses the density and the height, relative to a reference height in the domain, to determine the modified pressure at the boundary with a set value of pressure. In the present simulations, the mixture-averaged density was used. The `calculated` specification indicates that no boundary condition was applied. Finally, the `slip` condition imposes a zero-shear wall condition for velocity at the boundary.

Table 4.3: Boundary conditions for the turbulence validation cases

		Walls	**Outlet**	**Bottom**	**Inlet**
Temperature	Gas	`zeroGradient`	`inletOutlet` 293 K	`zeroGradient`	293 K
	Liquid	`zeroGradient`	`inletOutlet` 293 K	`zeroGradient`	293 K
Phase Fraction	Gas	`zeroGradient`	`inletOutlet 0`	`zeroGradient`	0.7853
	Liquid	zeroGradient	`inletOutlet 1`	`zeroGradient`	0.2147
Velocity	Gas	$(0, 0, 0)$ m/s	`zeroGradient`	$(0, 0, 0)$ m/s	$(0, 0, 3.979)$ m/s
	Liquid	$(0, 0, 0)$ m/s	`slip`	$(0, 0, 0)$ m/s	$(0, 0, 0)$ m/s
Modified Pressure		`zeroGradient`	`prghPressure`	`zeroGradient`	`zeroGradient`
Turbulent Kinetic Energy		`zeroGradient`	`inletOutlet 0`	`zeroGradient`	`zeroGradient`
Turbulent Dissipation Rate		`zeroGradient`	`inletOutlet 0`	`zeroGradient`	1×10^{-3} m^2/s^3
Turbulent Thermal Diffusivity		`calculated`	`calculated`	`calculated`	`calculated`
Turbulent Viscosity		`calculated`	`calculated`	`calculated`	`calculated`

The initial conditions for the fields are given in Table 4.4.

Table 4.4: Initial field conditions for the turbulence validation cases

Temperature		**Phase Fraction**		**Velocity**		**Modified Pressure**
Gas	Liquid	Gas	Liquid	Gas	Liquid	
293 K	293 K	0	1	$(0, 0, 3.979)$ m/s	$(0, 0, 0)$ m/s	1×10^5 Pa

Turbulence initial conditions are given in Table 4.5 below. The turbulent kinetic energy was initialized as non-zero even though the liquid was initially stationary to avoid division by zero errors. The same was done for the turbulent kinematic viscosity and the turbulent thermal diffusivity.

Table 4.5: Initial turbulent field conditions

Turbulent Kinetic Energy $[m^2/s^2]$	**Turbulence Dissipation Rate** $[m^2/s^3]$	**Turbulent Thermal Diffusivity** $[kg/m \cdot s]$		**Turbulent Kinematic Viscosity** $[m^2/s]$	
Liquid	Liquid	Gas	Liquid	Gas	Liquid
1×10^{-3}	1×10^{-3}	1×10^{-12}	1×10^{-12}	1×10^{-12}	1×10^{-12}

All of the simulations were initially unstable due to the high inlet velocity. The simulations were initialized with a low time-step which was allowed to increase over time based on the Courant Freidrichs Lewy (CFL) condition ($Co_{max} = 0.5$). All the simulations were very sensitive to the time-step, particularly in the calculation of drag. A maximum of $\Delta t = 0.001$ s was therefore also employed as a second condition on the time-step.

Four outer correctors and two inner correctors were selected for the PIMPLE loop, and turbulence was solved on every outer loop. Residuals (absolute tolerance) for the solutions of every property were kept below 1×10^{-7} and convergence on the outer PIMPLE loops was closely monitored.

4.4 Results

To assess which turbulence models could be suitable for application with the `twoPhaseEulerFoam` solver, the phase fraction contours between the model result and the experiment were compared. Predicting the correct spread of the gas is important for the interfacial area concentration prediction as well as the mass transfer rate, both of which are proportional to the phase fraction. The magnitude of the turbulent

kinetic energy in the liquid is also very important to predict correctly because it has a major impact on the liquid velocity. The experimental results of Sheng and Irons (1993) are shown for reference in Figure 4.3, with 10 levels of the phase fraction and 9 levels of the turbulent kinetic energy.

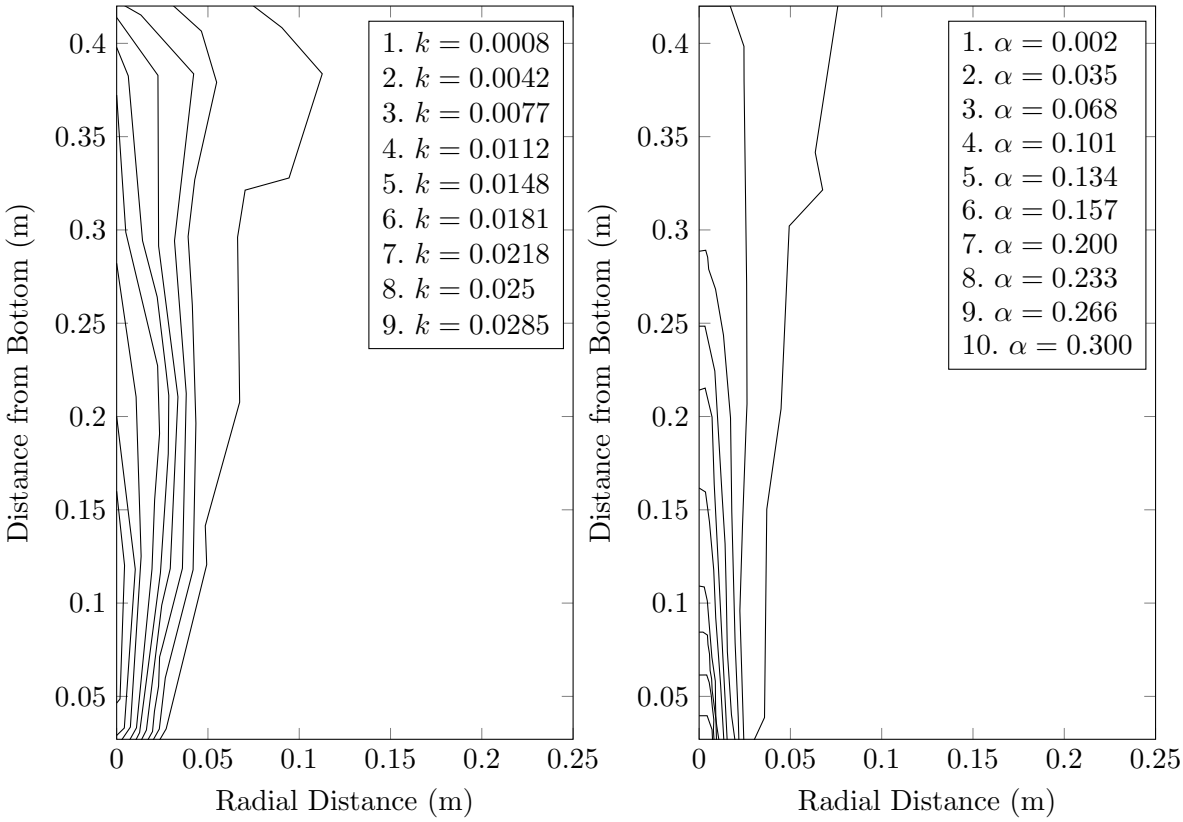

Figure 4.3: Experimental results from Sheng and Irons (1993). Turbulent kinetic energy (left) and phase fraction (right) contours for a volumetric gas flowrate of 50 mL/s in a model ladle. The graph begins from the first measurement location, 0.027 m up the ladle.

For the simulations, all data was averaged over a minimum of 50 s, after the gas had reached the free surface. Each of the cases was executed on four processors, however computational speed was not compared due to the difference in frequency and age of the processors that were used. In general, the simulation which incorporated the Smagorinsky (1963) model was the fastest to run. The phase fraction contours in each of the following figures are the same as the contours of Figure 4.3.

The combinations of simulations that were included in this chapter are summarized in Table 4.6. Several lift force coefficients were applied to test cases in advance of the included simulations, and the results were consistent with the conclusion of Lou and

Zhu (2013b) that the lift coefficient should be $C_L = 0.1$. The boundary conditions were also varied to attempt to obtain the most realizable result in the final simulations.

Table 4.6: Models and tuned parameters

Model	**Bubble Sizes**	**Meshes**	**BIT Viscosity**	**Lopez de Bertodano (1998) Turbulent Dispersion Coefficient**
Behzadi et al. (2004)	$d = 0.014$ m	M_2	Yes	0.2
Ničeno et al. (2008b)	$d = 0.014$ m	M_2	Yes	0.1
Smagorinsky (1963)	$d = 0.014$ m	M_2	No	0.4
		M_2	Yes	0.2
Simonin and Viollet (1988)	$d = 0.005$ m	M_2	Yes	0.2
	$d = 0.01$ m	M_2	Yes	0.2
	$d = 0.014$ m	M_1	Yes	0.2
		M_2	Yes	0.2
		M_3	Yes	0.2
	$d = 0.02$ m	M_2	Yes	0.2

4.4.1 General Model Comparison

The time-averaged result for the phase fraction from the simulation of the ladle with the Behzadi et al. (2004) model is shown in Figure 4.4. A turbulent dispersion coefficient of $C_{TD} = 0.2$ was found to be the most appropriate through trial and error. The coefficient was chosen based on whether it maximized the spread without splitting the plume down the centre, as well as how closely it matched the experimental data. The model yielded the least spread of the phase fractions compared to the other turbulence models, but the general shape was correct.

The Simonin and Viollet (1988) model result for the time-averaged phase fraction is shown in Figure 4.5. A turbulent dispersion coefficient of $C_{TD} = 0.2$ was used to maximize the spread while attempting to match the experimental data. The spread and location of the contours are similar to those in the Sheng and Irons (1993) experimental study. The $\alpha = 0.233$ contour is slightly higher, and the higher phase fraction contours disappear much lower in the ladle simulation than in the experimental study.

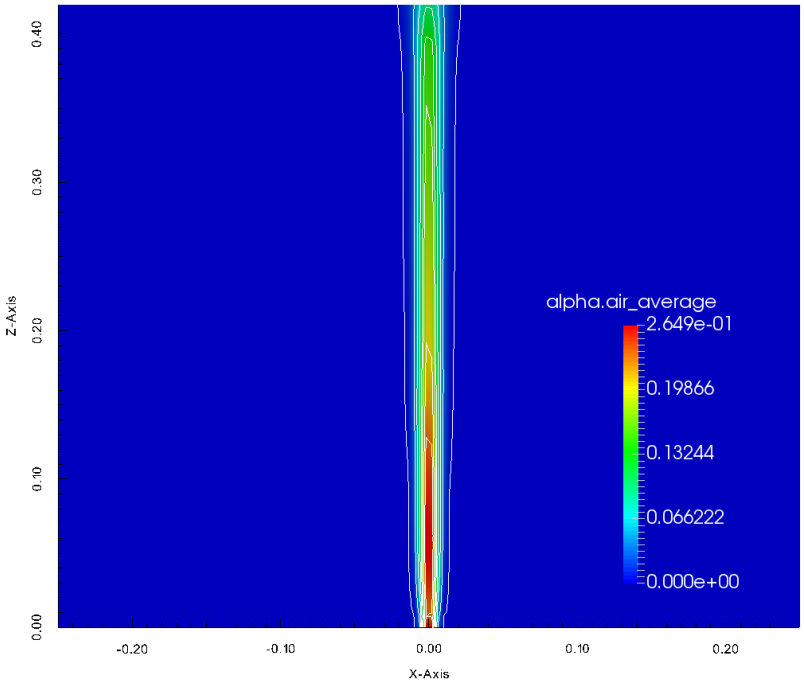

Figure 4.4: Phase fraction contours using the Behzadi et al. (2004) $k-\epsilon$ model.

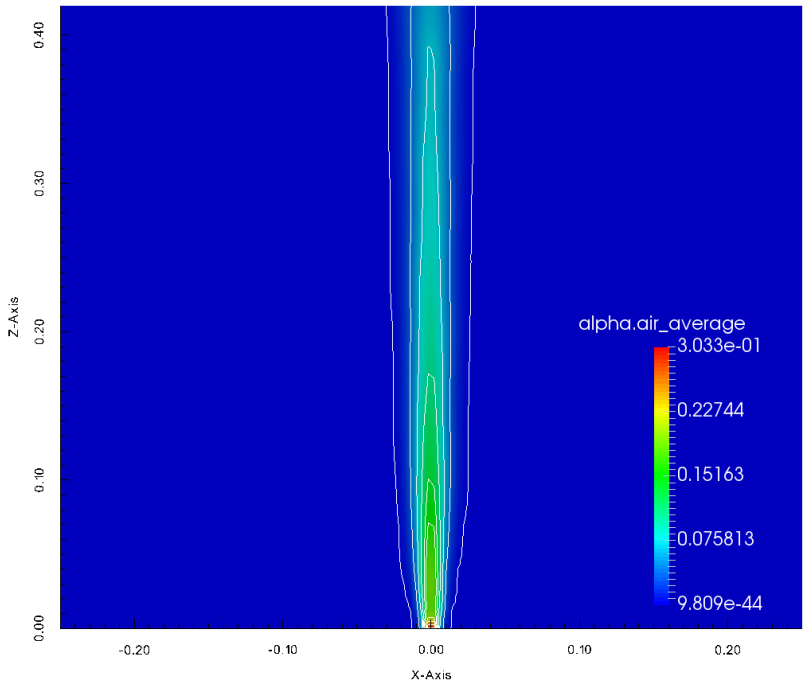

Figure 4.5: Phase fraction contours using the Simonin and Viollet (1988) $k-\epsilon$ model.

The time-averaged phase fraction result for the Ničeno et al. (2008b) model case is shown in Figure 4.6. A turbulent dispersion coefficient of $C_{TD} = 0.1$ was used,

although all coefficients caused overly high spreading of the low phase fractions and not enough spreading of the higher fractions. The phase fraction contours are also not quite symmetric about the axis, and a longer averaging time may have been necessary for the case.

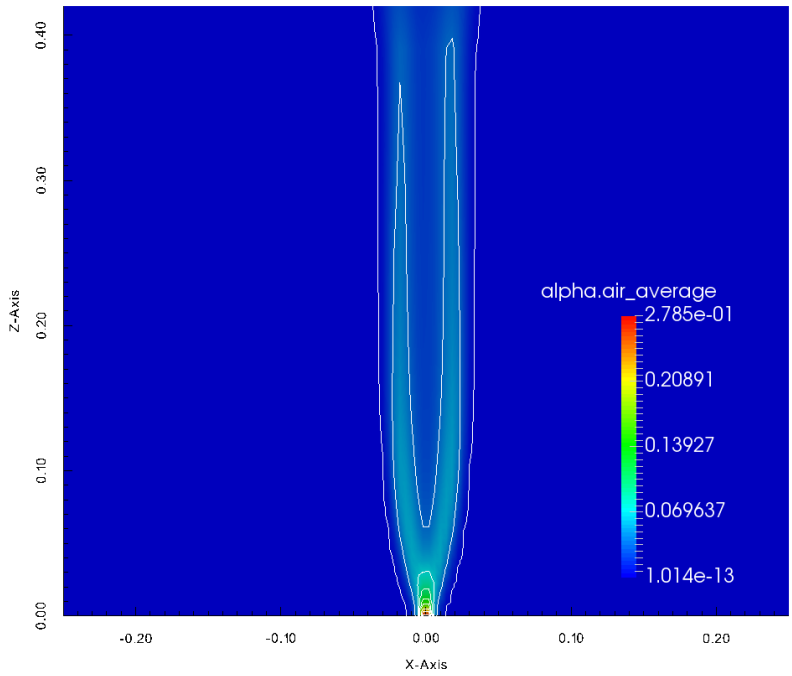

Figure 4.6: Phase fraction contours using the Ničeno et al. (2008b) model.

The time-averaged phase fraction result for the Smagorinsky (1963) model case is shown in Figure 4.7. A turbulent dispersion coefficient of $C_{TD} = 0.4$ was found to yield a result which was closest to the experimental data through trial and error. Compared to the experimental result, the contours are closer than those of Behzadi et al. (2004), but the higher phase fraction contours still did not extend far enough up the ladle.

The time-averaged phase fraction result for the Smagorinsky (1963) model case with the BIT viscosity is shown in Figure 4.8. A turbulent dispersion coefficient of $C_{TD} = 0.2$ was used based on trial and error. The plume developed a minimum down the center, but the simulation came closest to the experimental data with this value. The phase fraction contours are not totally symmetric about the axis, which, like with the Ničeno et al. (2008b) model, indicates that a longer averaging time may have been necessary for the case. The high phase fractions were suppressed, and spreading was only observed in the lowest phase fractions.

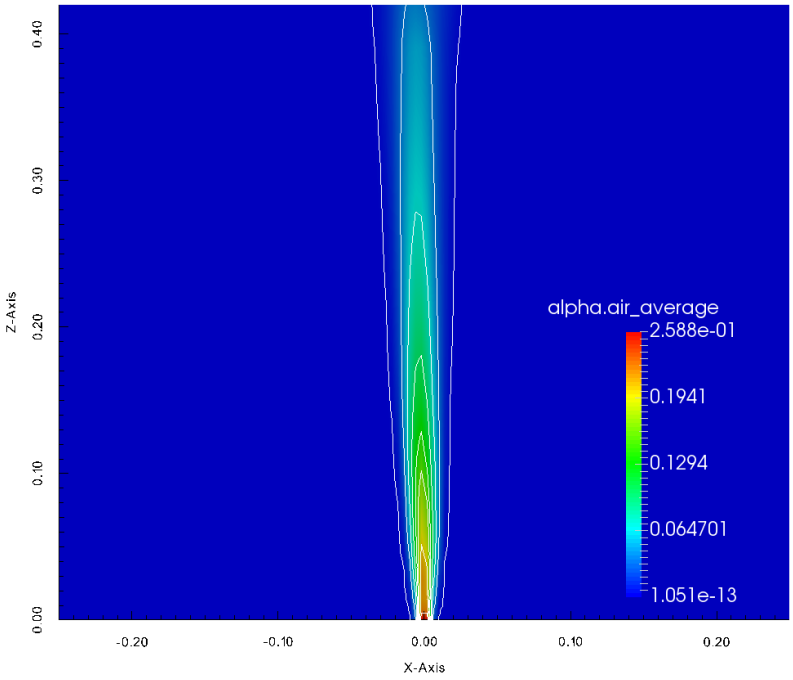

Figure 4.7: Phase fraction contours using the Smagorinsky (1963) model.

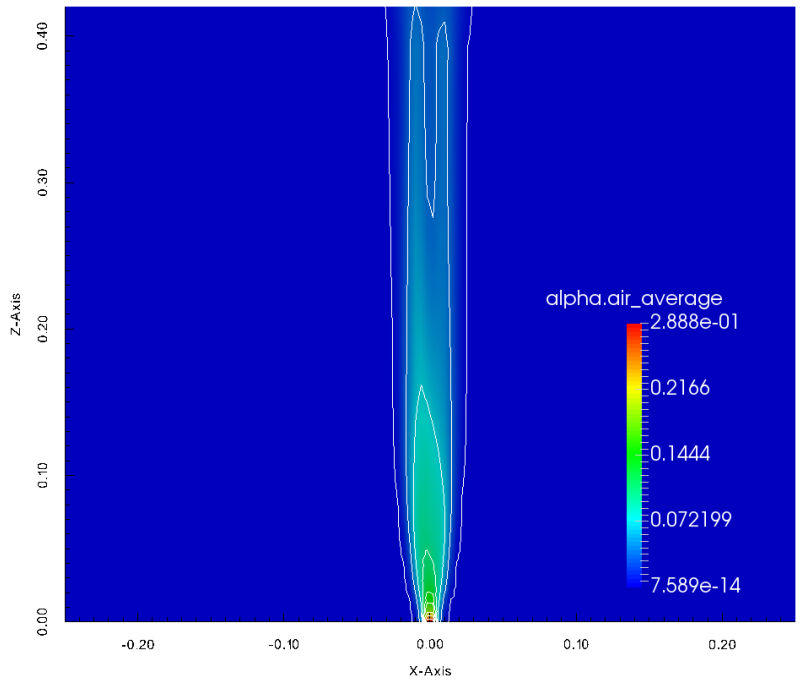

Figure 4.8: Phase fraction contours using the Smagorinsky (1963) model with the BIT viscosity term of Sato and Sekoguchi (1975).

4.4.2 Detailed Model Comparison

The centreline profile of the axial liquid velocity obtained with each model is shown in Figure 4.9. The Smagorinsky (1963) model produced the best result of the five models, but it, like all the other models except the Simonin and Viollet (1988) model, exhibited strange behaviour near the top of the ladle. This may be due to the unphysicality of the boundary conditions compared to the true free-surface behaviour. The Simonin and Viollet (1988) model did not have this effect, but resulted in a very low liquid velocity along the centreline. This result is not the same as that obtained by Sheng and Irons (1993), who found that their modification to the turbulent kinetic energy and turbulent dissipation rate equation source terms gave them results for the liquid axial velocity which matched well with the experimental data. Lou and Zhu (2013b) also found good agreement between their model and the experiment. The overprediction of the liquid axial velocity by the Behzadi et al. (2004) model was expected due to the comparisons made by Sheng and Irons (1993), which showed that several other $k-\epsilon$ models tended to result in a high liquid axial velocity along the centreline as well. The other two models gave similar results to each other, but did not match the trend of the data well.

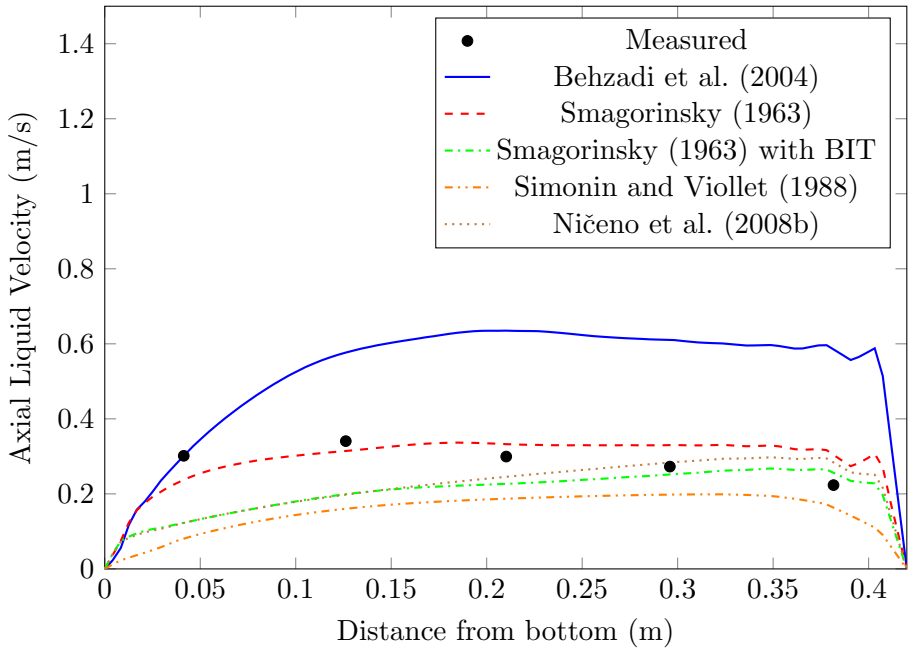

Figure 4.9: The time-averaged axial liquid velocity along the centreline of the plume.

The radial profile of the time-averaged axial liquid velocity at 0.21 m is shown in Figure 4.10. None of the models were able to capture the effect of the wall, and this

may be due to the lack of wall functions used in the $k-\epsilon$ cases. The Smagorinsky (1963) model was the closest to predicting the correct phase fraction at 0.21 m at the centreline, but did not produce the correct amount of spreading, resulting in an overly steep slope in the radial direction between $r = 0$ m and $r = 0.05$ m. The Simonin and Viollet (1988) model predicted too much spreading of the phase fraction in the radial direction, caused by too high a value of liquid axial velocity, and underpredicted the value at the centreline. The Ničeno et al. (2008b) model, as seen on the contour map, resulted in a large spread of the lower phase fractions, which is also shown by the radial profile for the velocity seen here. The Smagorinsky (1963) model with the BIT viscosity term appears to have the most accurate trend in the liquid axial velocity along the radial direction, however only three experimental data points were provided near the centreline so this would be difficult to quantify.

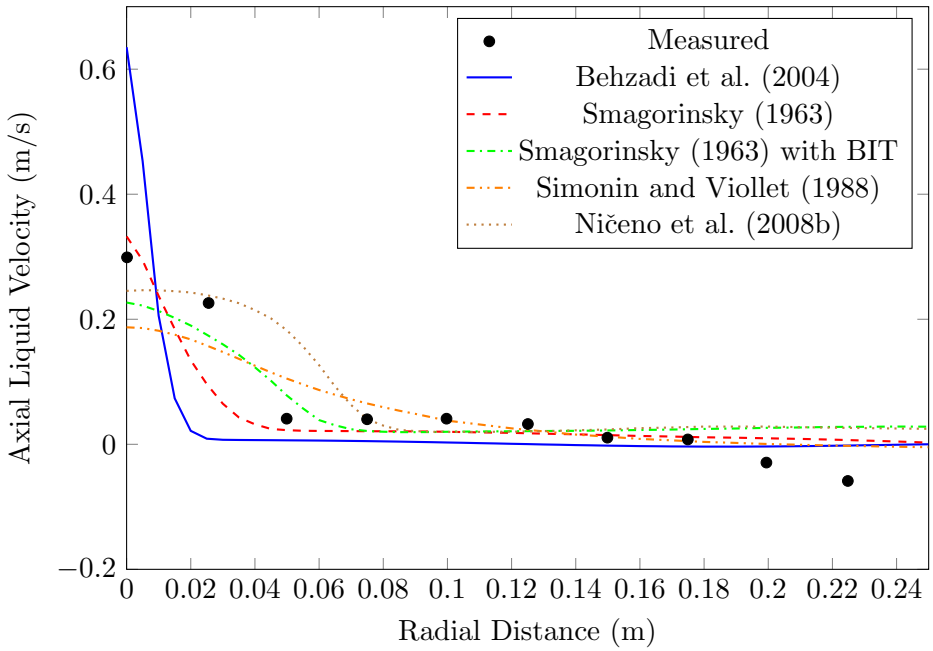

Figure 4.10: The average axial liquid velocity in the radial direction at 0.21 m from the bottom of the ladle.

The time-averaged phase fractions from each model along the centreline of the plume are shown in Figure 4.11. The Smagorinsky (1963) model gave the closest result to the experimental value, followed by the Simonin and Viollet (1988) model. The Behzadi et al. (2004) model has a large dip in its profile adjacent to the centreline, and also exhibited the most spread of the higher phase fractions. The Ničeno et al. (2008b) and Behzadi et al. (2004) models were very far off from the experimental

data.

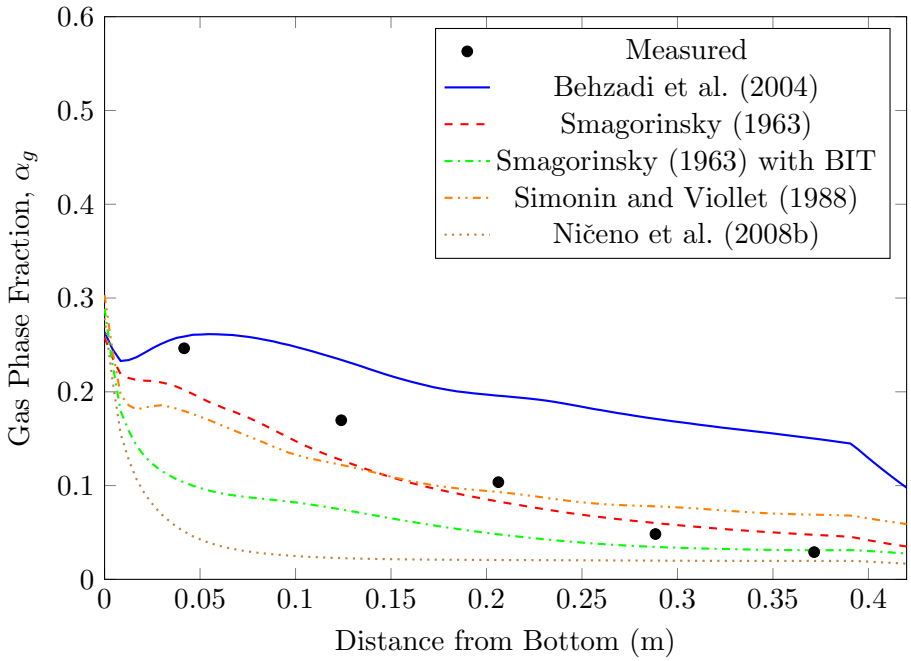

Figure 4.11: The average phase fraction along the centreline of the plume.

The turbulent kinetic energy in the liquid phase was plotted for the five models. The $k-\epsilon$ models resulted in the lowest turbulent kinetic energies in the liquid. The Behzadi et al. (2004) model gave the lowest values along the centreline, which is consistent with the finding in Sheng and Irons (1993). The Simonin and Viollet (1988) model simulation results were not consistent with the modeled results of Sheng and Irons (1993), who found that their simulations came very close to matching with the experiment, which was not the case in the present study. The resolved turbulent kinetic energies for the two no-equation LES-SGS models were computed as,

$$k = \frac{1}{2}\overline{U_l}^2 \tag{4.2}$$

The Smagorinsky (1963) model predicted the highest value for the turbulent kinetic energy along the centreline, which did not correspond with the experimental data. Considering only the resolved stress was plotted, the total turbulent kinetic energy including the sub-grid quantity would have resulted in an even higher value. Although the Simonin and Viollet (1988) model with the altered coefficient of Sheng and Irons (1993) did not yield a result close to the experimental result, nor did the case reproduce the modeled result of Sheng and Irons (1993) it probably gave the best

prediction aside from the two Smagorinsky (1963) models for the turbulent kinetic energy.

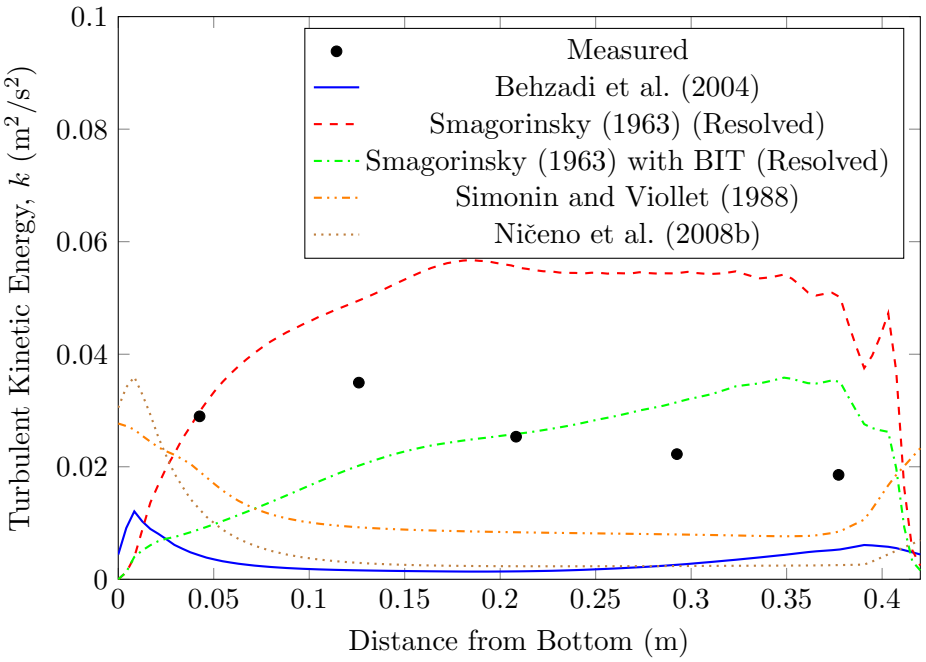

Figure 4.12: The average turbulent kinetic energy along the centreline of the plume.

In general, the Smagorinsky (1963) model and the model of Simonin and Viollet (1988) gave the best predictions for the parameters shown. The Smagorinsky (1963) model overpredicted the turbulent kinetic energy in the liquid, but obtained the closest results to the experimental study for all the other parameters. The Simonin and Viollet (1988) model with the altered coefficient did not behave as it did in the Sheng and Irons (1993) study, and the reason for this is unknown, but is likely due to the tuning of the force models. The differences could have come down to the convergence criteria of the other studies, number of dimensions simulated, numerical schemes, etc. Aside from the Smagorinsky (1963) model, the Simonin and Viollet (1988) model still gave better predictions for the parameters than the other models.

To test whether the Simonin and Viollet (1988) model with the alterations of Sheng and Irons (1993) was obtaining the best result, two additional studies were performed. The first, a mesh study, compared three meshes to verify that the optimal mesh was being used for the model. The second study was performed to observe the sensitivity of the results to the bubble size. The results of these studies are given in the following sections.

4.4.3 Mesh Study

A mesh study was performed using the Simonin and Viollet (1988) model, to be sure the model had been optimized in the turbulence model comparison. To determine the mesh which yielded the best result for the Simonin and Viollet (1988) turbulence model, the axial liquid velocity, volume fraction, and liquid turbulent kinetic energy along the centreline were compared to the experimental values. Mesh sizes of $M_1 =$ 187500 cells (max $\frac{\Delta}{d_g} = 0.76$) and $M_3 = 42750$ cells (max $\frac{\Delta}{d_g} = 1.4$) were compared to the original mesh ($M_2 = 105000$).

The first comparison for the three meshes was for the phase fraction along the centreline. The most resolved mesh, M_1, resulted in the lowest phase fraction along the centreline. This was likely because the mesh size was so small that the turbulent kinetic energy was overly dissipated near the inlet to the domain. The least refined mesh, M_3, overpredicted the phase fraction along the centreline, despite being the closest to obeying the Milleli condition of $\frac{\Delta}{d_g} = 1.5$. The best result for the phase fraction along the centreline was decidedly the mesh which was used in the turbulence model comparison, M_2.

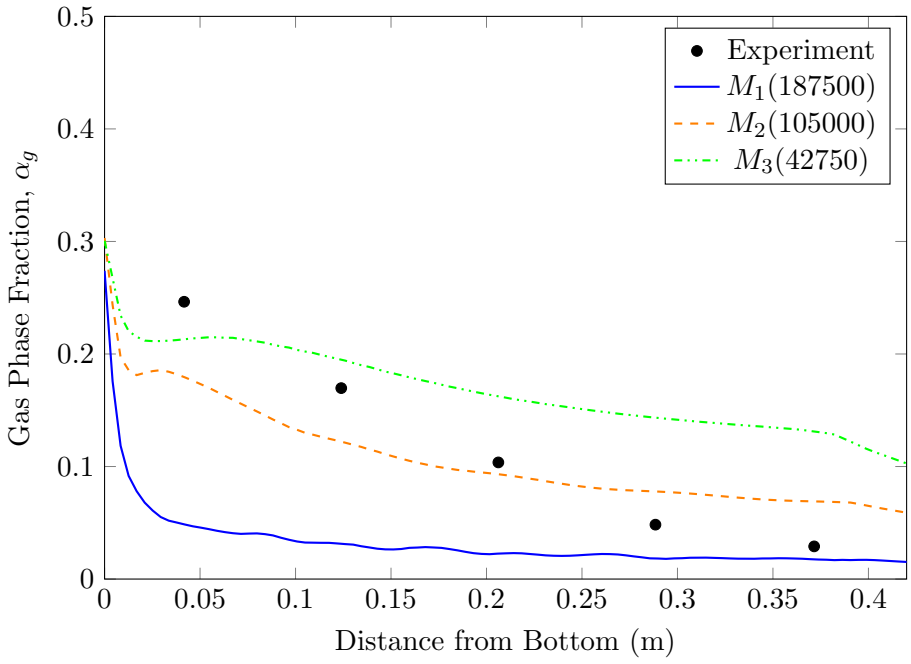

Figure 4.13: Comparison of experimental and mesh study results for the phase fraction along the centreline.

The axial liquid velocity along the centreline is shown in Figure 4.14 for the three

meshes. The least refined mesh gave the highest average liquid axial velocity along the centreline of the three meshes, making it slightly closer to the experimental values than the other meshes. The most refined mesh gave the worst result for the liquid axial velocity, which lines up with the result obtained for the phase fraction as well.

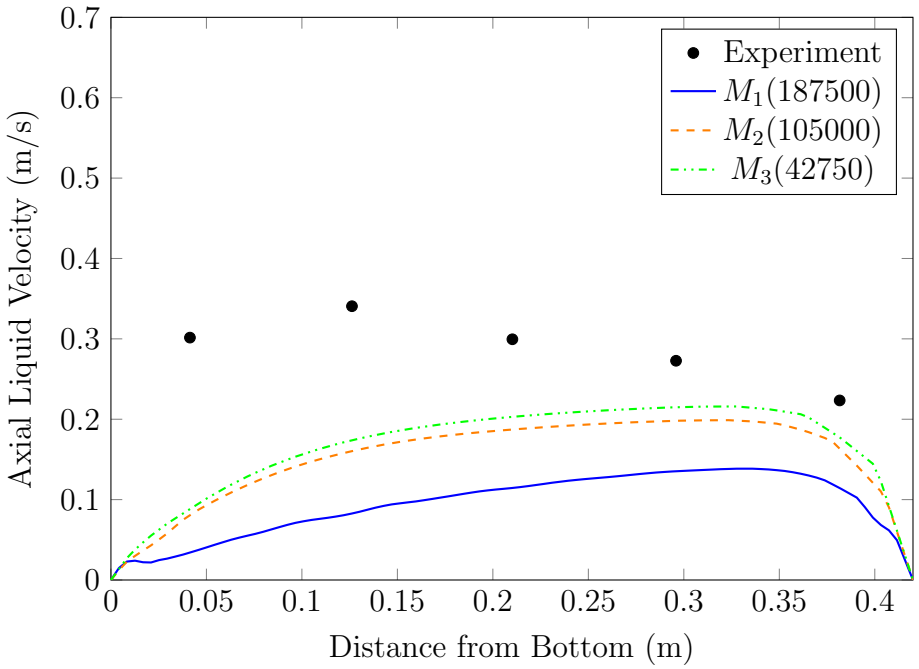

Figure 4.14: Comparison of experimental and mesh study results for the axial liquid velocity along the centreline.

The turbulent kinetic energy in the liquid along the centreline is shown in Figure 4.15. None of the meshes improved upon the result obtained in the turbulence model comparison. The trends are very different than in the experiment, and the values are very far off. The turbulent kinetic energy is dissipated too quickly near the inlet, where it should be increasing. Near the top of the ladle, the turbulent kinetic energy increases, where it appears to be decreasing in the experimental data.

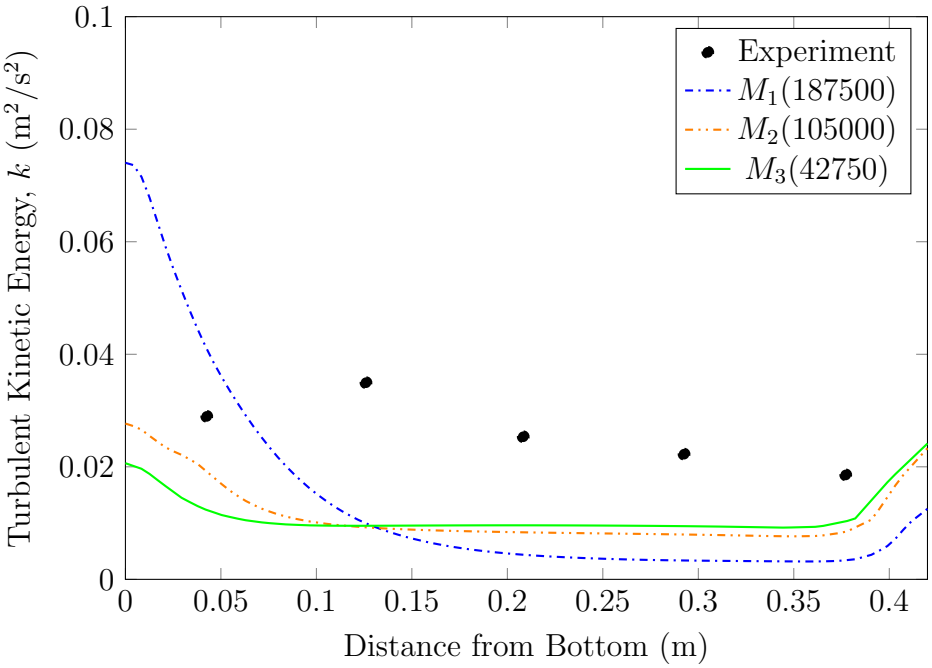

Figure 4.15: Comparison of experimental and bubble size study results for the turbulent kinetic energy along the centreline.

The mesh that was used in the turbulence comparison should have given the best result for the Simonin and Viollet (1988) model. The mesh was clearly not the cause for the discrepancy in simulation results between the study of Sheng and Irons (1993) and those displayed in this study. Lou and Zhu (2013b) did not give the details about the mesh they used, but based on the picture, it appears to be similar to the second mesh in this study. Mesh independence does not appear to be achievable with the parameters selected.

4.4.4 Bubble Size Study

In the turbulence model comparison, only a single constant bubble size was chosen. To ensure that the choice of bubble size did not have an extraordinary influence on the model of Simonin and Viollet (1988), a range of bubble sizes was chosen to be sure that the bubble size was not the cause for the discrepancy between the result of the current study and that of Sheng and Irons (1993). Bubble diameters of $d_1 = 0.005$ m, $d_2 = 0.01$ m, $d_3 = 0.014$ m (the original size), and $d_4 = 0.02$ m were compared to the experimental values.

The phase fraction along the centreline for the four different bubble sizes is shown in Figure 4.16. The two middle bubble sizes, d_2 and d_3 gave the closest results to the

experimental data. Bubble size d_2 was closer to the experimental result near the inlet of the plume, but maintained too high of a phase fraction near the outlet. The same is true for bubble size d_3, but the phase fraction in that simulation stayed the closest to the experimental result for both the top and bottom of the ladle. For the phase fraction prediction, the bubble size selected in the original turbulence comparison study, d_3, behaved the best with the selected model.

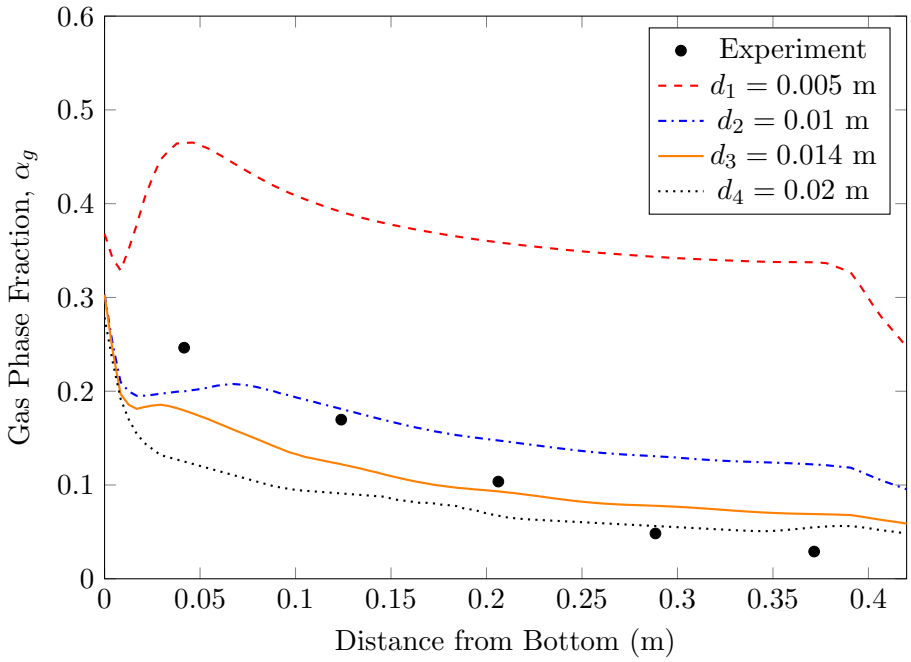

Figure 4.16: Comparison of experimental and bubble size study results for the phase fraction.

The axial liquid velocity for each bubble size simulation is shown in Figure 4.17. The smallest bubble size simulation, d_1, obtained the closest result to the experimental values. None of the curves had the correct trend for the liquid axial velocity, instead of increasing in value quickly near the bottom and gradually decreasing, all the simulations resulted in liquid axial velocity trends which were low near the bottom but higher at the top of the ladle. The original bubble size, d_3, had the lowest liquid axial velocity of all the bubble size simulations, but bubbles sizes d_1, d_2, d_3, and d_4 all gave very close results to each other in their predictions.

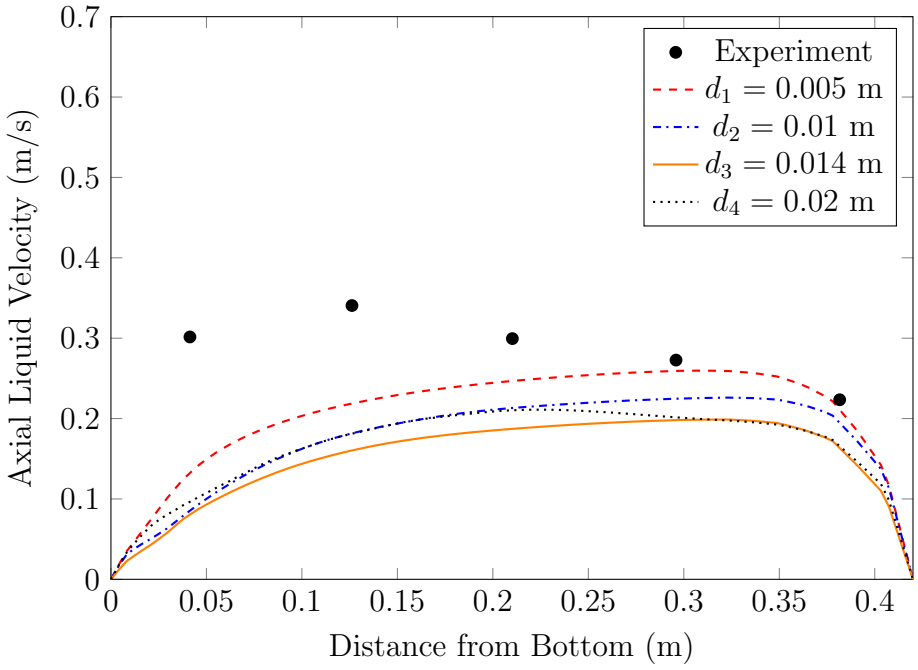

Figure 4.17: Comparison of experimental and bubble size study results for the axial liquid velocity along the centreline.

The liquid turbulent kinetic energy is shown for the four bubble sizes in Figure 4.18 along the centreline of the plume. The smallest bubble size, d_1, again gave the closest result to the experimental data. The trend for the turbulent kinetic energy for all the bubble sizes was not similar to that given by the experiment, still decreasing near the bottom of the ladle, and then only increasing again near the top. The experimental data may be subject to variability of the flow field, but the study of Sheng and Irons (1993) was capable of reproducing the experimental data nevertheless.

Despite bubble size d_1 resulting in the closest prediction for the liquid axial velocity and the liquid turbulent kinetic energy, its phase fraction prediction along the centreline was so far off from the experimental values that it must be disqualified. The original bubble size, d_3, resulted in approximately the same liquid axial velocity as the other sizes, although it was slightly lower. It also was the closest along the centreline to the experimental data for the phase fraction. The originally chosen bubble size was most likely to have been the optimal choice for those reasons.

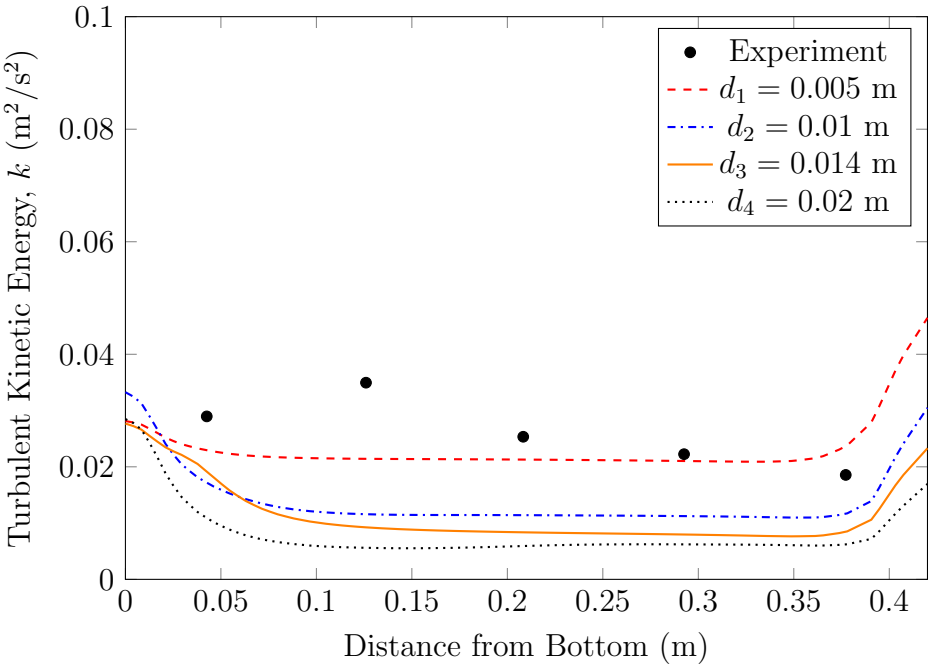

Figure 4.18: Comparison of experimental and bubble size study results for the turbulent kinetic energy along the centreline.

4.5 Discussion

Based on the results from the mesh and bubble size studies, the Simonin and Viollet (1988) model with the alterations of Sheng and Irons (1993) was optimized in the original comparison study between the five turbulence models. Nevertheless, it did not yield the same or similar result as in the simulation of Sheng and Irons (1993). The number of possible sources for error were reduced through the mesh and bubble size studies, but there are other tuning parameters that could be investigated more closely, such as wall functions and boundary conditions, the turbulent dispersion force, and the lift force. These parameters had been tested by trial and error before executing the simulations, but all the permutations of the tuning parameters could not be compared in the current study due to the time required for each simulation. The `twoPhaseEulerFoam` algorithm appears to be very sensitive to tuning, and this characteristic would indicate that it may not be a good model to use on a simulation where tuning parameters could not be adjusted to match experimental data.

Chapter 5

Hydrodynamic Study and IATE Model Evaluation

The results of the previous chapter did not compare well with the results obtained by Sheng and Irons (1993). An experiment which was more representative of the hydrodynamics in the plume region of the full-scale case was used to attempt to further assess the hydrodynamic predictions obtained using `twoPhaseEulerFoam`. The numerical study of Dhotre and Smith (2007), which used the data from the second experimental study of Simiano (2005), was reproduced in this section. In order to assess the effectiveness of the IATE model, the experimental results from the first experimental study of Simiano (2005) were used to apply the model of Wu et al. (1998) described in Chapter 3. The two separate case studies are referred to as case 1 and case 2, respectively, throughout this chapter.

5.1 Experimental Configurations of Simiano (2005)

The experiments of Simiano (2005) were chosen because the wall was quite far from the plume, and the flow could potentially be considered almost unconfined. Experimental measurements of the interfacial area were also provided at several heights in the vessel, and were used for comparison. Additionally, simulation results from Dhotre and Smith (2007) and Dhotre et al. (2009) were available to help in the tuning of the sub-models.

In the experiment, a bubble plume was produced in a large vessel, $D \times z = 2$ m $\times$ 3.4 m, which was monitored using a combination of photography, thermocouple measurements, pitot tubes, optical and electromagnetic probes, and particle image velocimetry (PIV). The vertical cross-sections of the two setups are shown in Figure 5.1. Two separate case studies were used to assess the hydrodynamics and bubble size predictions for the two setups.

The injection plate was comprised of 350 needles with 1 mm inner diameters in the first case, and 716 needles with inner diameters of 1 mm for the second case, distributed on a 0.15 m diameter plate and a 0.3 m diameter plate respectively.

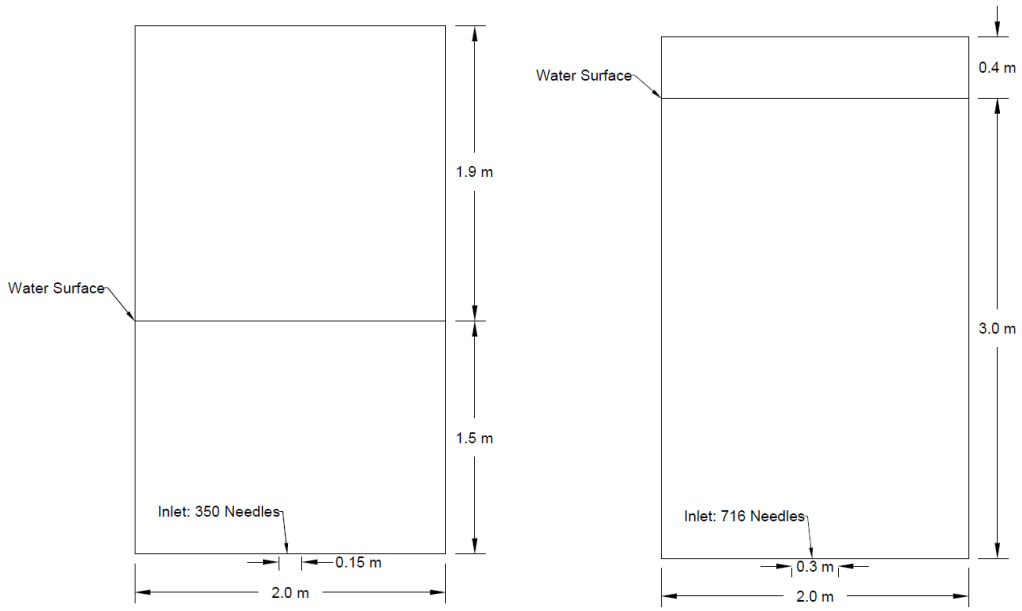

Figure 5.1: The cross-sections of the geometry for the experiments of Simiano (2005). Case study 1 (left) and case study 2 (right).

5.2 Setup for the First Case Study

Three meshes for case 1 were used to simulate the first experimental study of Simiano (2005). Mesh 1 had 12150 cells, with max $\frac{\Delta}{d_g} = 54.00$ and min $\frac{\Delta}{d_g} = 7.00$ for the same initial bubble diameter as the first mesh (Figure 5.2). The inlet of the second mesh did not have smooth circular edges, which could cause artificial turbulence generation. The first mesh was made to address this potential issue.

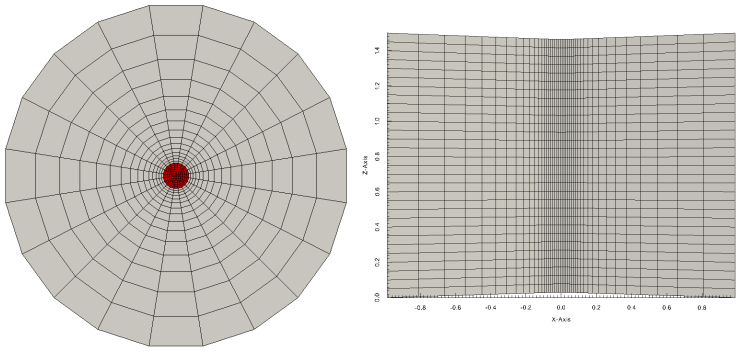

Figure 5.2: The first computational domain for the case 1 simulation of the experiments of Simiano (2005). The meshed domain (left) and cross-section of the domain (right).

Mesh 2 had 108750 cells, $D \times z = 85$ m $\times$ 30 m, with max $\frac{\Delta}{d_g} = 24.84$ and min

$\frac{\Delta}{d_g} = 4.03$ assuming a 2.5 mm bubble diameter (Figure 5.3). This mesh was slightly less refined than that of Dhotre and Smith (2007) in the radial direction, and had the same refinement in the z-direction. Smearing of the properties in the corner directions of the central rectangle due to the interpolation was not observed. The inlet was modeled as the 0.15 m diameter circular plate and the free surface was not included in the simulations.

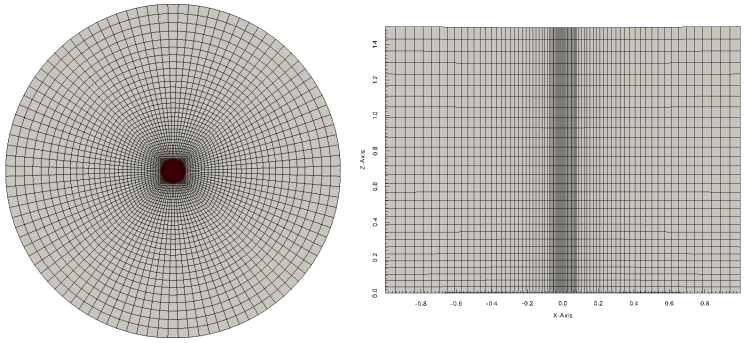

Figure 5.3: The second computational domain for the case 1 simulation of the experiments of Simiano (2005). Top view (left) and cross-section (right).

Mesh 3 was the same mesh as in Dhotre and Smith (2007), but no free surface was included in the simulation. It had 352000 cells with max $\frac{\Delta}{d_g} = 18.30$ and min $\frac{\Delta}{d_g} = 2.03$ with the same initial bubble diameter as the first mesh. Figure 5.4 shows mesh 3.

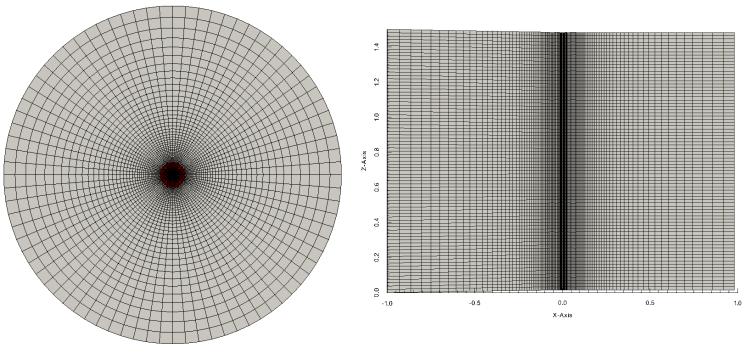

Figure 5.4: The third computational domain for the case 1 simulation of the experiments of Simiano (2005). Top view (left) and cross-section (right).

The boundary conditions for the first case are given in Table 5.1 and were the same for all meshes, except in the simulations with wall functions. The inlet gas flow rate was 7.5 NL/min in the experimental study, and the velocity was calculated based on the whole needle plate as the inlet. The gas flow in was not adjusted for the pressure

or temperature, which was a minor oversight. This would change the density slightly, but would not change the trends in the results appreciably for these cases. Since the model of Simonin and Viollet (1988) is only meant to be solved in the liquid, only the liquid turbulence model transport equations were solved. The turbulent kinetic energy and dissipation rate were set to low values at the inlet to avoid division by zero, although their values would have been zero since no liquid entered the vessel through the inlet. Adjusting this low value did not have an appreciable impact on the result.

Table 5.1: Boundary conditions for case 1

		Walls	**Oulet**	**Bottom**	**Inlet**
Temperature	Gas	`zeroGradient`	`zeroGradient`	`zeroGradient`	293 K
	Liquid	`zeroGradient`	`zeroGradient`	`zeroGradient`	293 K
Phase Fraction	Gas	`zeroGradient`	`zeroGradient`	`zeroGradient`	0.5
	Liquid	`zeroGradient`	`zeroGradient`	`zeroGradient`	0.5
Velocity	Gas	$(0, 0, 0)$ m/s	`zeroGradient`	$(0, 0, 0)$ m/s	$(0, 0, 0.01415)$ m/s
	Liquid	$(0, 0, 0)$ m/s	slip	$(0, 0, 0)$ m/s	$(0, 0, 0)$ m/s
Modified Pressure		`zeroGradient`	1×10^5 Pa	`zeroGradient`	`zeroGradient`
Turbulent Kinetic Energy		`zeroGradient`	`inletOutlet` 0.001	`zeroGradient`	1×10^{-3} m^2/s^2
Turbulent Dissipation Rate		`zeroGradient`	`inletOutlet` 0.001	`zeroGradient`	1×10^{-3} m^2/s^3
Turbulent Thermal Diffusivity		`calculated`	`calculated`	`calculated`	`calculated`
Turbulent Viscosity		`calculated`	`calculated`	`calculated`	`calculated`

The turbulent dispersion model of Davidson (1990) was used with a constant value for the drag coefficient, $C_d = 0.44$, along with a lift coefficient of $C_L = 0.1$ and a virtual mass coefficient of $C_{VM} = 0.5$ as in the study of Dhotre and Smith (2007). The bubble diameter was set as a constant value of 2.5 mm as in Dhotre and Smith (2007). The initial field conditions for the first case are specified in Table 5.2.

Table 5.2: Initial field conditions for case 1

Temperature		**Phase Fraction**		**Velocity**		**Modified Pressure**	**Turbulent Dissipation Rate**	**Turbulent Kinetic Energy**
gas	liquid	gas	liquid	gas	liquid			
293 K	293 K	0	1	$(0, 0, 0.01415)$ m/s	$(0, 0, 0)$ m/s	1×10^5 Pa	1×10^{-3} m^2/s^3	1×10^{-3} m^2/s^2

5.3 Setup for the Second Case Study

The mesh for case 2 had 181250 cells, $D \times z = 85$ m $\times$ 50 m, with max $\frac{\Delta}{d_g} = 4.17$ and min $\frac{\Delta}{d_g} = 16.06$ assuming a 4 mm inlet bubble diameter. The inlet was modeled as the whole 0.3 m diameter circular plate. The mesh is shown in Figure 5.5.

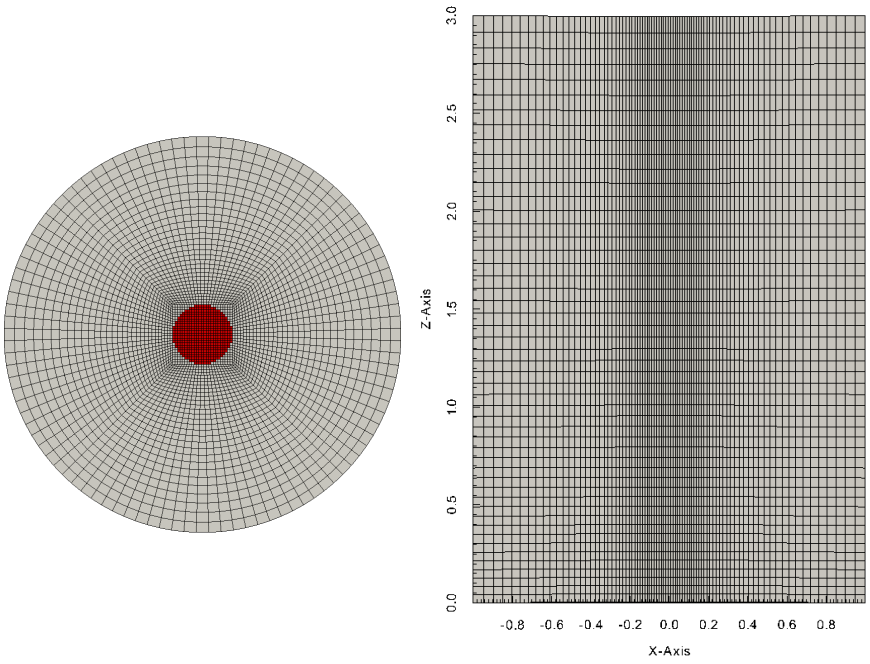

Figure 5.5: The computational domain for the case 2 simulation of the experiments of Simiano (2005). Top view (left) and cross-section (right).

The initial field conditions for the second case are specified in Table 5.3. The turbulent dissipation rate and the turbulent kinetic energy were set to low values to avoid division by zero.

Table 5.3: Initial field conditions for case 2

Temperature		**Phase Fraction**		**Velocity**		**Modified Pressure**	**Interfacial Curvature**	**Turbulent Dissipation Rate**	**Turbulent Kinetic Energy**
gas	liquid	gas	liquid	gas	liquid				
293 K	293 K	0	1	$(0, 0, 0.71)$ m/s	$(0, 0, 0)$ m/s	1×10^5 Pa	Varies	1×10^{-3} m^2/s^3	1×10^{-3} m^2/s^2

The boundary conditions for the second case are given in Table 5.4. The inlet gas flow rate was 30 NL/min in the experimental study, and the velocity was calculated based on the whole needle plate as the inlet (i.e. superficial velocity). Again, the inlet flowrate was not adjusted for temperature and pressure. The phase fraction was

set to a low value in this case, unlike in the previous case where the phase fraction was initially high. The phase fraction was set to a lower value than in the first case, approximately corresponding to the mean phase fraction at the four locations in the vessel where it was experimentally measured.

Table 5.4: Boundary conditions for case 2

		Walls	**Oulet**	**Bottom**	**Inlet**
Temperature	Gas	`zeroGradient`	`zeroGradient`	`zeroGradient`	293 K
	Liquid	`zeroGradient`	`zeroGradient`	`zeroGradient`	293 K
Phase Fraction	Gas	`zeroGradient`	`zeroGradient`	`zeroGradient`	0.01
	Liquid	`zeroGradient`	`zeroGradient`	`zeroGradient`	0.99
Velocity	Gas	$(0, 0, 0)$ m/s	`zeroGradient`	$(0, 0, 0)$ m/s	$(0, 0, 0.71)$ m/s
	Liquid	$(0, 0, 0)$ m/s	slip	$(0, 0, 0)$ m/s	$(0, 0, 0)$ m/s
Modified Pressure		`zeroGradient`	1×10^5 Pa	`zeroGradient`	`zeroGradient`
Interfacial Curvature		`zeroGradient`	`zeroGradient`	`zeroGradient`	Varies
Turbulent Kinetic Energy		`zeroGradient`	`inletOutlet` 0.001	`zeroGradient`	1×10^{-3} m^2/s^2
Turbulent Dissipation Rate		`zeroGradient`	`inletOutlet` 0.001	`zeroGradient`	1×10^{-3} m^2/s^3
Turbulent Thermal Diffusivity		`calculated`	`calculated`	`calculated`	`calculated`
Turbulent Viscosity		`calculated`	`calculated`	`calculated`	`calculated`

5.4 Results and Discussion

The first case was done to verify that the hydrodynamics of the Dhotre and Smith (2007) study could be replicated with `twoPhaseEulerFoam`. As previously noted, the same parameters and force models were used as in the 3-D Dhotre and Smith (2007) simulation. The turbulence model of Simonin and Viollet (1988) with the altered parameters of Sheng and Irons (1993) was used consistently for all the cases discussed in this chapter. The second case was divided into two sections. The first section used the same parameters as the first case, but also included the implementation of the IATE model. The second section used the turbulence dissipation model of Lopez de Bertodano (1998) along with the IATE model, with all the other parameters the same as the previous case. The fluid properties from Chapter 4 for an air-water system

were used (Table 4.1). The results that were obtained are reported in this section.

5.4.1 Case 1

The comparison between the current study and the study of Dhotre and Smith (2007) is given in this section. The liquid axial velocity across the radius of the plume at 35 cm is shown in Figure 5.6. Although 35 cm is fairly far from the inlet, the axial liquid velocity is almost three times as large as the measured value at the centreline for all three meshes. The results also do not match that found by Dhotre and Smith (2007), and were almost double their reported centreline value.

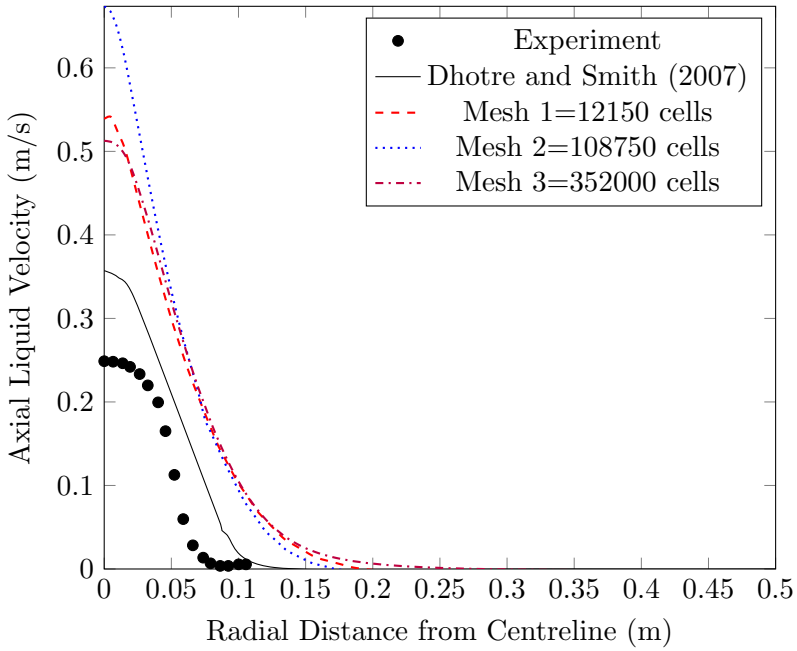

Figure 5.6: Comparison of experimental and simulation results for the axial liquid velocity at $z = 0.35$ m.

The liquid axial velocity across the radius of the plume at 75 cm is shown in Figure 5.7. At this height from the inlet, the results for all the meshes are much closer to the results obtained by the Dhotre and Smith (2007) study and the experiment. Mesh 1 and mesh 3 gave a better prediction for the centreline value for both the Dhotre and Smith (2007) study and the experimental result, but had the most unphysical lateral spread. Mesh 2 gave a higher value along the centreline than all the other results.

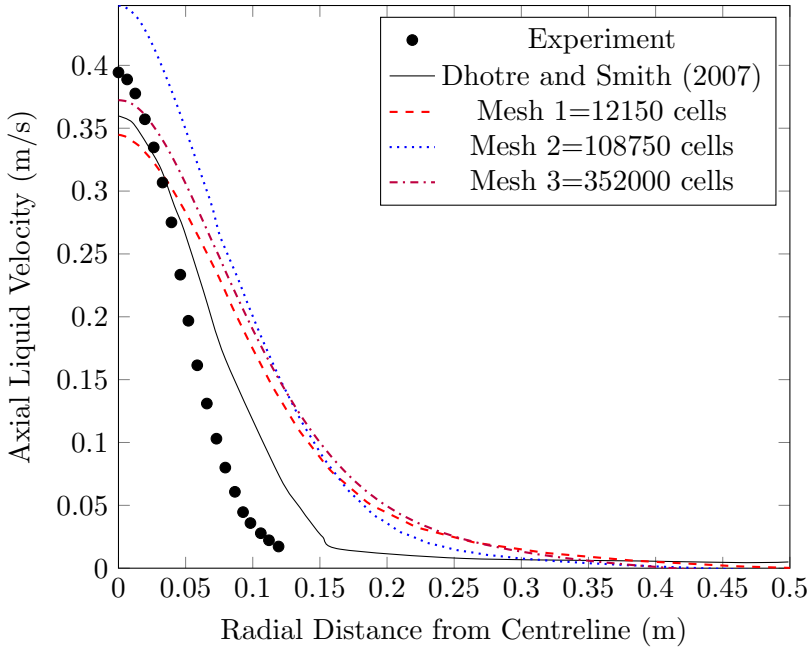

Figure 5.7: Comparison of experimental and simulation results for the axial liquid velocity at $z = 0.75$ m.

The liquid axial velocity across the radius of the plume at 110 cm is shown in Figure 5.8. The first and third meshes underpredicted the liquid axial velocity, while the second mesh still overpredicted it at this height. None of the simulations gave a result at this height which matched that of Dhotre and Smith (2007).

The axial gas velocity across the radius of the plume at 35 cm is shown in Figure 5.9. The high value at the centreline caused by mesh 2 is consistent with the high liquid axial velocity value previously noted at this point in the plume. Mesh 3 gave the closest trend to the experimental data, but was still much higher at the centreline and along the radius. The values along the centreline for all the meshes are almost twice the measured value, and are significantly higher than the value obtained by Dhotre and Smith (2007).

The axial gas velocity across the radius of the plume at 75 cm is shown in Figure 5.10. Similarly to the axial liquid velocity, the two simulation values and the measured values are significantly closer to the measured value than at 35 cm. The centreline value is matched by the simulation with mesh 1 and 3, but the axial gas velocity past $r = 0.07$ m begins to diverge, with higher values for all three meshes than the experimental result.

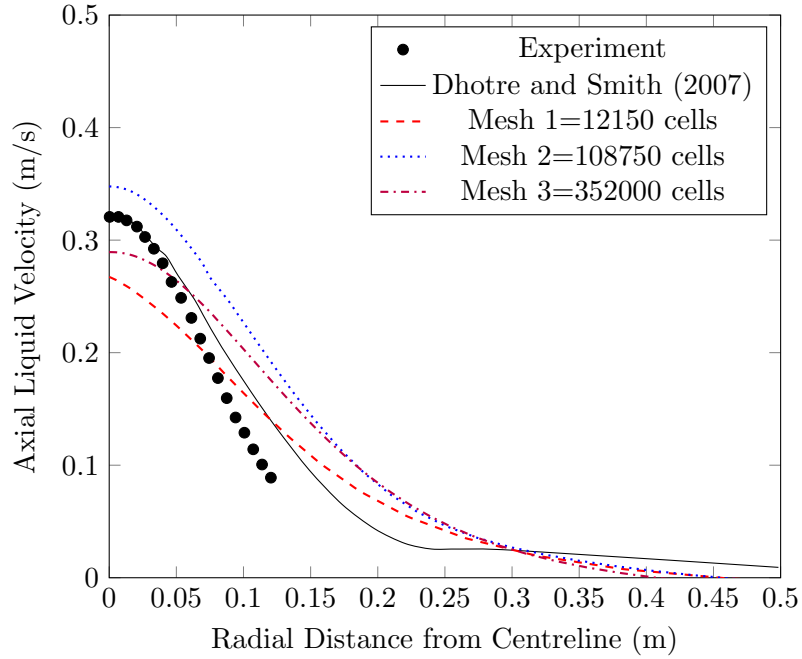

Figure 5.8: Comparison of experimental and simulation results for the axial liquid velocity at $z = 1.10$ m.

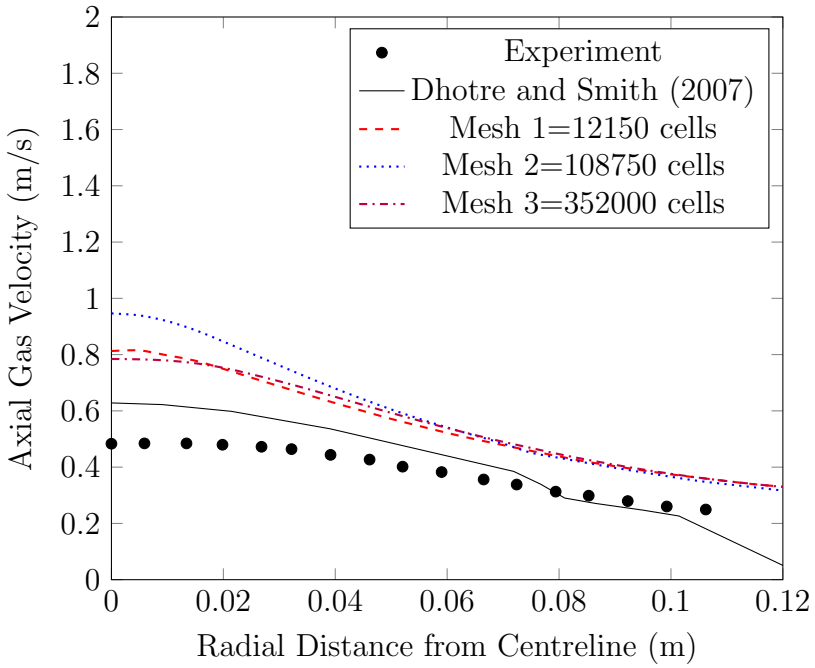

Figure 5.9: Comparison of experimental and simulation results for the axial gas velocity at $z = 0.35$ m.

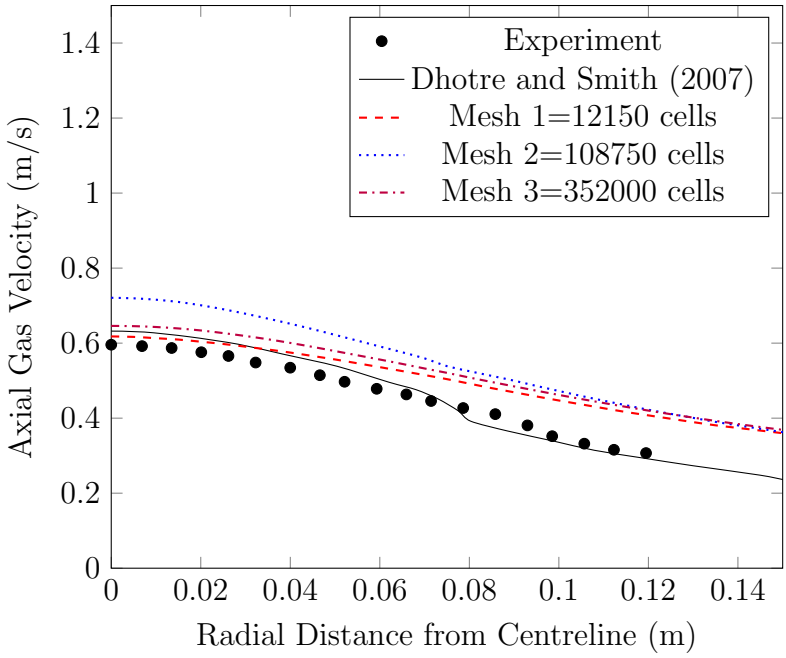

Figure 5.10: Comparison of experimental and simulation results for the axial gas velocity at $z = 0.75$ m.

The axial gas velocity across the radius of the plume at 110 cm is shown in Figure 5.11. The gas velocity at the centreline for mesh 2 is much closer to that obtained in the study of Dhotre and Smith (2007) as well as the experiment. Although mesh 3 produced the correct centreline value at 75 cm height, it underpredicts it slightly at this height. Mesh 2 obtained a very close result to the measured values. Mesh 1 was the farthest from the measured values of all the simulations.

Perhaps the most surprising result is the turbulent kinetic energy across the radius of the plume at 35 cm, shown in Figure 5.12. The turbulent kinetic energy at this height is overpredicted by a large margin by all the meshes. This could account for the inaccurate values for the velocities at this height, as well as the overprediction of the spread. The general trend appears to be correct, but the value at $r \sim 0.075$ m for the current study is almost three times as high as the measured quantity for mesh 2, and even higher for mesh 1. Mesh 3 and mesh 2 give similar results at the centreline at this height, although the level of refinement is significantly higher for mesh 3.

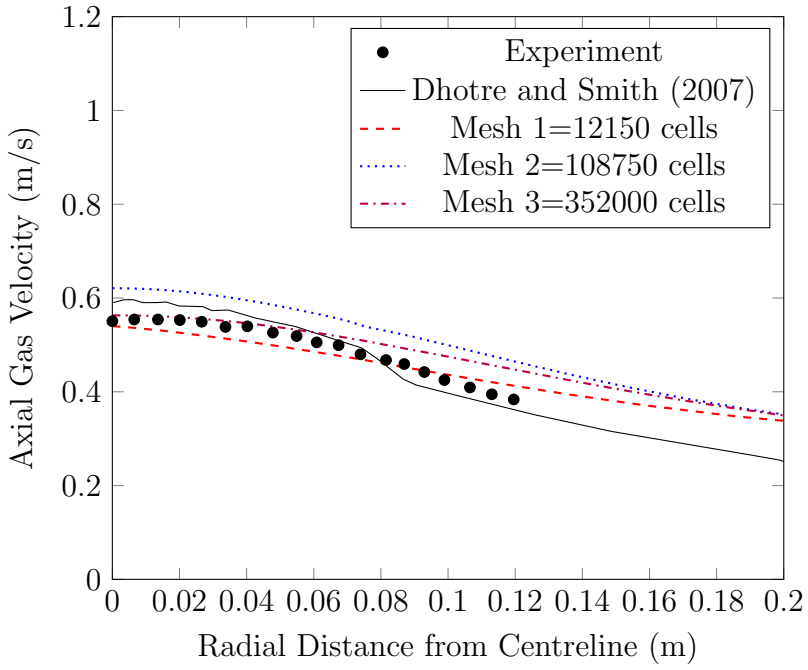

Figure 5.11: Comparison of experimental and simulation results for the axial gas velocity at $z = 1.10$ m.

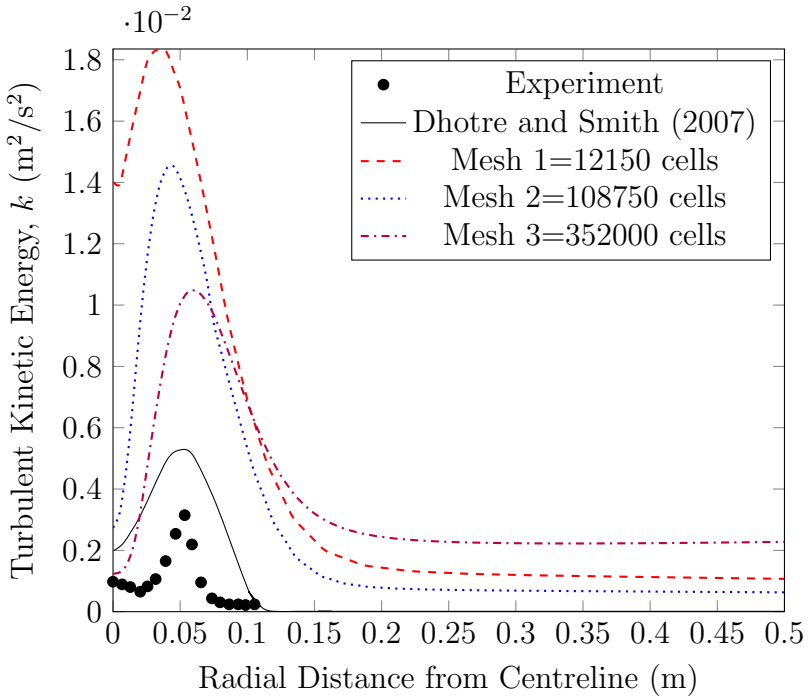

Figure 5.12: Comparison of experimental and simulation results for the turbulent kinetic energy at $z = 0.35$ m.

The turbulent kinetic energy across the radius of the plume at 75 cm is shown in Figure 5.13. Like with the velocities, at this level in the vessel, the turbulent kinetic energy predictions for all three meshes appear to be closer to the experimental values as well as those obtained by Dhotre and Smith (2007). All meshes overpredict the experimental value at this height and resulted in very close results to each other.

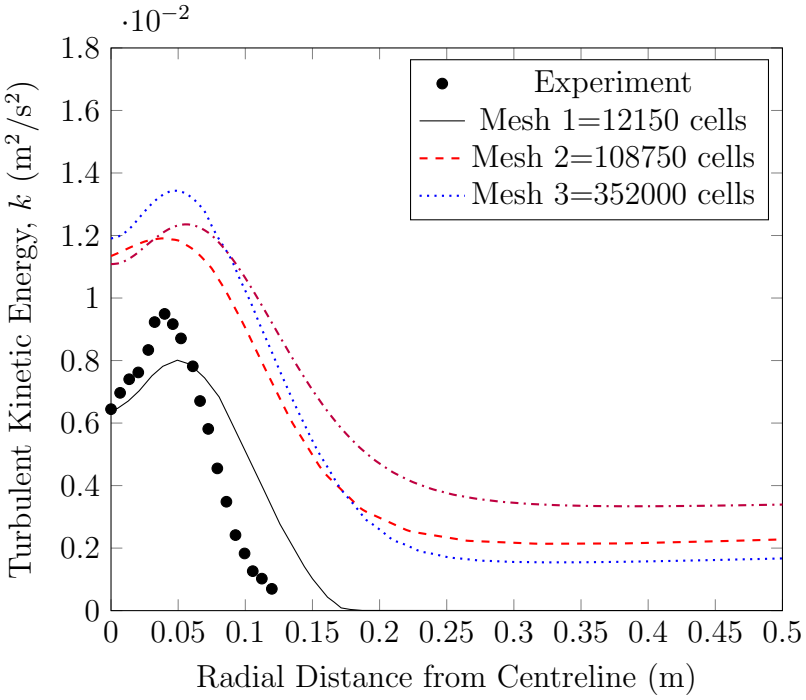

Figure 5.13: Comparison of experimental and simulation results for the turbulent kinetic energy at $z = 0.75$ m.

The turbulent kinetic energy across the radius of the plume at 110 cm is shown in Figure 5.14. The Dhotre and Smith (2007) prediction underpredicts the turbulent kinetic energy at this height while the simulation with mesh 2 and 3 overpredict it. Mesh 1 has a very close centreline value to that of the experiment, but has a higher spread. Mesh 3 gave the least accurate prediction at this height.

The phase fraction across the radius of the plume at 35 cm is shown in Figure 5.15. It is important to note that mass was conserved, although it does not look like it at first glance. The area of the cylinder must be taken into account at all radii. The measured phase fraction at this height is more than double the values obtained along the centreline for all the meshes. Mesh 1 gave a lower result than mesh 2 and mesh 3 at this height. Mesh 3 was closest to the measured result, but was still off along the centreline by a significant margin. All three meshes overpredict the lateral

spread, which could be because of the overprediction of the turbulent kinetic energy at this height.

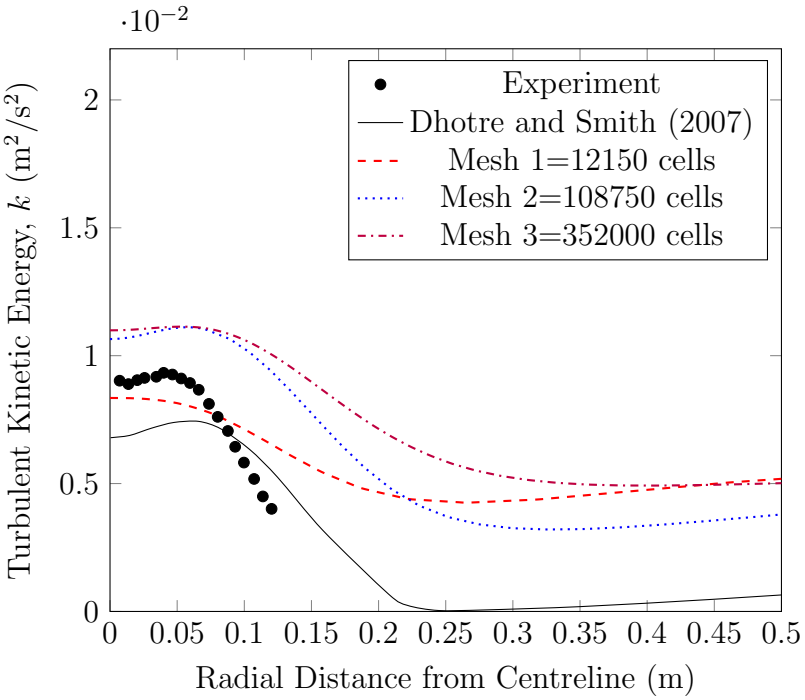

Figure 5.14: Comparison of experimental and simulation results for the turbulent kinetic energy at $z = 1.10$ m.

The gas phase fraction across the radius of the plume at 75 cm is shown in Figure 5.16. The predictions obtained by the three meshes are still significantly lower than the experimental results as well as the study of Dhotre and Smith (2007). This is most likely caused by the overprediction of the turbulent kinetic energy which is still evidenced at this height. The turbulent kinetic energy prediction would also account for the large amount of spreading of the phase fraction at this height.

The phase fraction across the radius of the plume at 110 cm is shown in Figure 5.17. The phase fraction is still underpredicted at this height. Even though the gas and liquid velocities at this height are much closer to the experimental value for all the meshes, the phase fraction appears to remain low for mesh 1. This is not consistent with the turbulent kinetic energy at this height, as it was very close to the measured value at the centreline at this height. Mesh 3 was the closest to the measured value at this height but was still spread out too far laterally, like the other meshes.

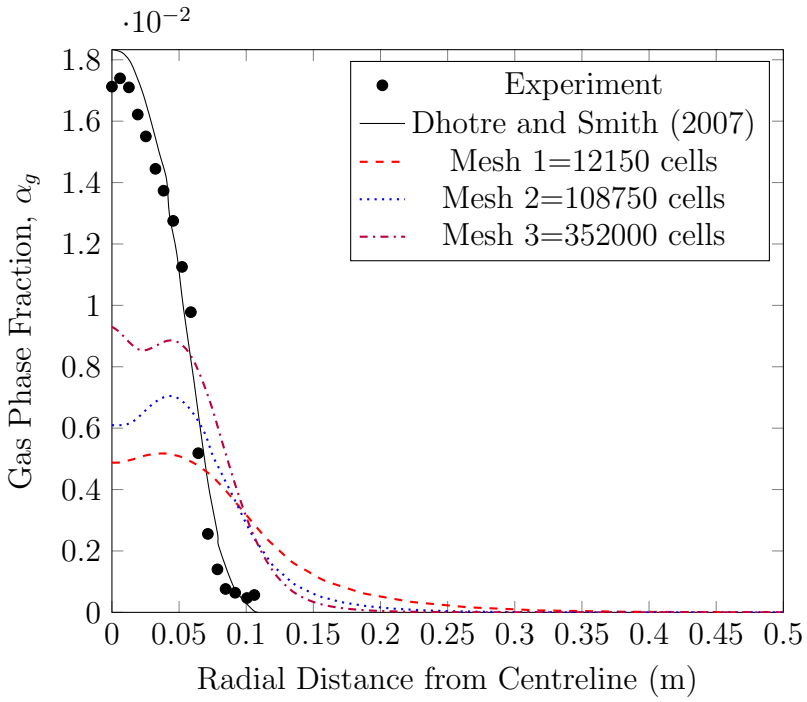

Figure 5.15: Comparison of experimental and simulation results for the phase fraction at $z = 0.35$ m.

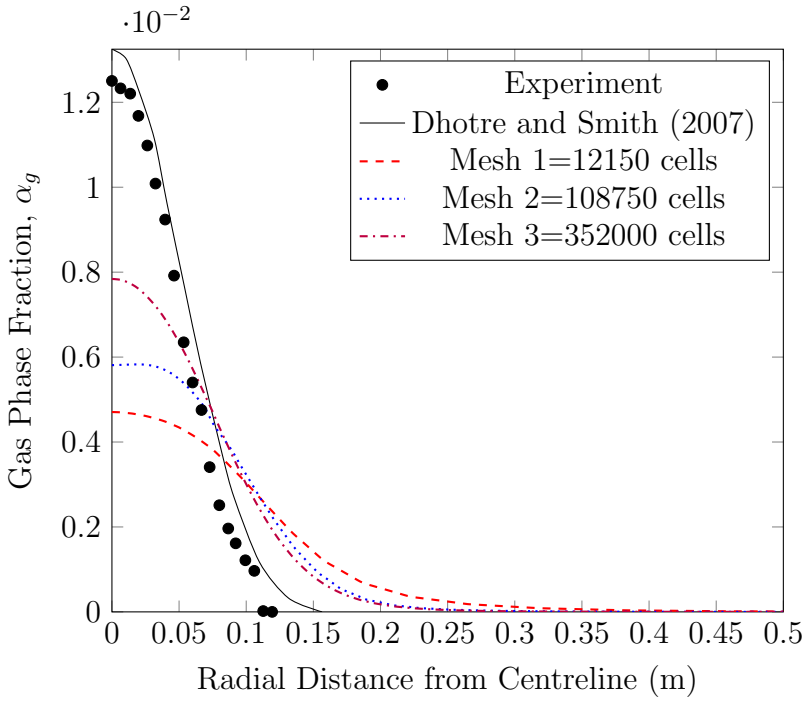

Figure 5.16: Comparison of experimental and simulation results for the phase fraction at $z = 0.75$ m.

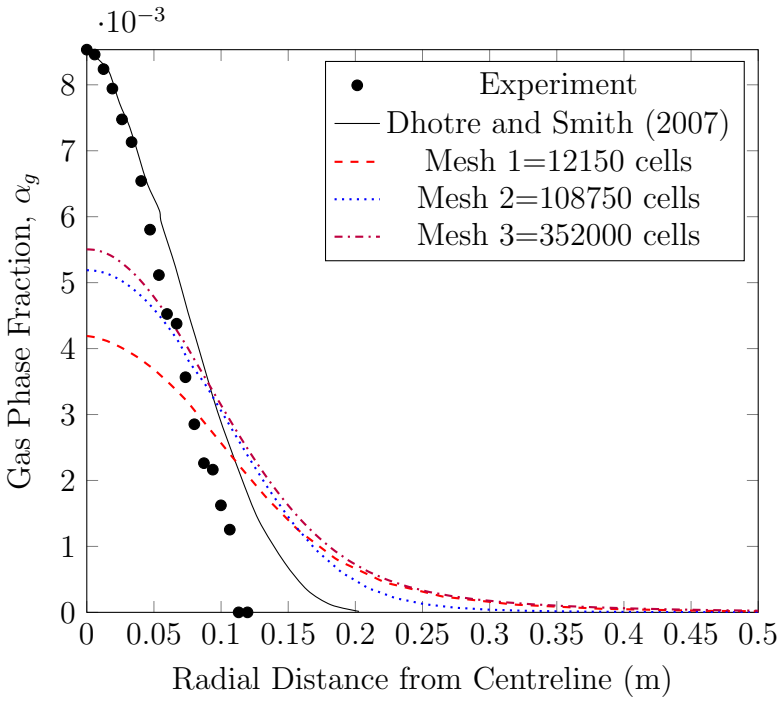

Figure 5.17: Comparison of experimental and simulation results for the phase fraction at $z = 1.10$ m.

It appears to be the case, based on the obtained results, that the simulations in this study and those of Dhotre and Smith (2007) are not comparable, despite having the same tuning parameters, using the same sub-models, and using the same mesh. At higher locations in the vessel, the results for the velocities and the turbulent kinetic energy appear to be closer to the study of Dhotre and Smith (2007) for the meshes, but the simulations never gave exactly the same result. Convergence for the three mesh simulations, in both the inner and outer PIMPLE loops was achieved, and steady state had been reached, so this could not be the reason for the discrepancy.

The spread of the phase fraction near the inlet is unlike the experimental data, and improves only slightly at higher locations in the domain. The effect of the turbulent kinetic energy at the inlet is likely to be the cause - it spread the gas out initially so that it could not recover at other heights. This could also be why the cases in Chapter 4 resulted in inaccurate predictions for the phase fraction. If the inlet conditions are not correctly predicted, the inaccuracy propagates through the rest of the simulation. This is problematic for obtaining a mass transfer prediction of a full-scale gas well blowout. The mass transfer is highly dependent on the phase fraction and the relative velocity, so if either is incorrectly predicted near the inlet of the domain, the amount of transfer could be seriously over- or under-predicted as well.

The results indicate that the combination of sub-models and their tuning parameters, boundary conditions and numerical settings could not achieve an accurate result for each of the three meshes. The second mesh gave increasingly better predictions as the height was increased, while the same was not true for the first or third meshes. The first experiment of Simiano (2005) has results at higher elevations in the vessel, so it is possible that at these heights the accuracy of the current model is good enough to test the effectiveness of the IATE model. It is also possible that the settings need to be tweaked for any subtle differences between the code used by Dhotre and Smith (2007) and `twoPhaseEulerFoam`.

5.4.1.1 Effect of the Inlet Condition

Dhotre and Smith (2007) found that the choice of inlet phase fraction had almost no effect in their simulations. Reproduction of this result was attempted. Two separate inlet phase fractions were compared: $\alpha = 0.5$ and $\alpha = 1$ on the fine mesh (Mesh 3). Both cases were adjusted to give the correct superficial velocity in accordance with the phase fraction.

The contours from all the cases with a phase fraction inlet condition of $\alpha = 0.5$ looked quite similar. This inlet condition was applied to the fine mesh and the result for the velocity vectors and the phase fraction at steady state are shown in Figure 5.18. The phase fraction field has a similar look to that reported by Dhotre and Smith (2007) but it is much different in magnitude, as evidenced by the low values noted along the centreline. The large velocity vectors at the bottom are not present in their case either. The recirculation pattern at the bottom is counter to the flow when it should be in line with the flow. The recirculation at the top is also closer to the plume than the result of Dhotre and Smith (2007).

Figure 5.19 shows the velocity vectors and phase fraction field for the inlet condition of $\alpha = 1$. The velocity vectors are much closer to that obtained by Dhotre and Smith (2007), although there is still much more spreading in the current case. The high velocity vectors are no longer observed near the inlet, and the recirculation pattern at the bottom is in line with the flow. This should have caused the plume to pinch in toward the centreline, but this behaviour does not appear to have occurred. The phase fraction appears to be inhibited, with the higher fractions staying near the inlet instead of spreading upward, as expected.

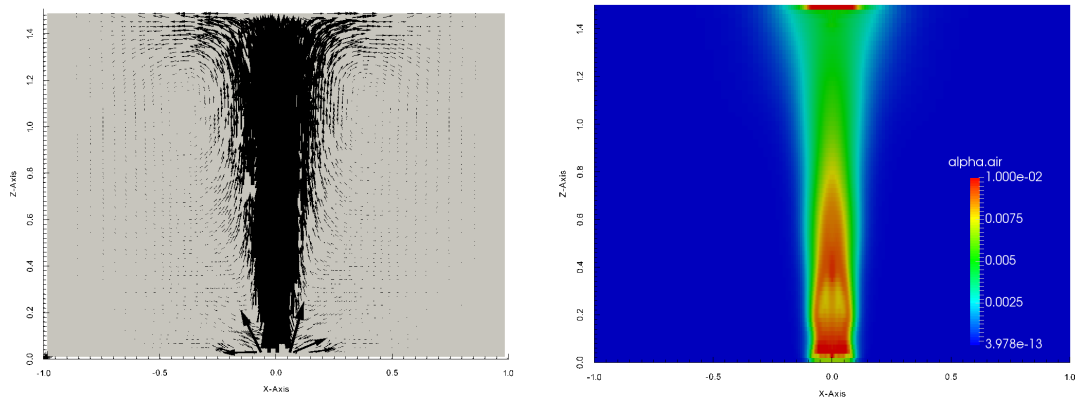

Figure 5.18: The liquid velocity vector plot (left) and phase fraction field for the case with an inlet of $\alpha = 0.5$ and the finest mesh.

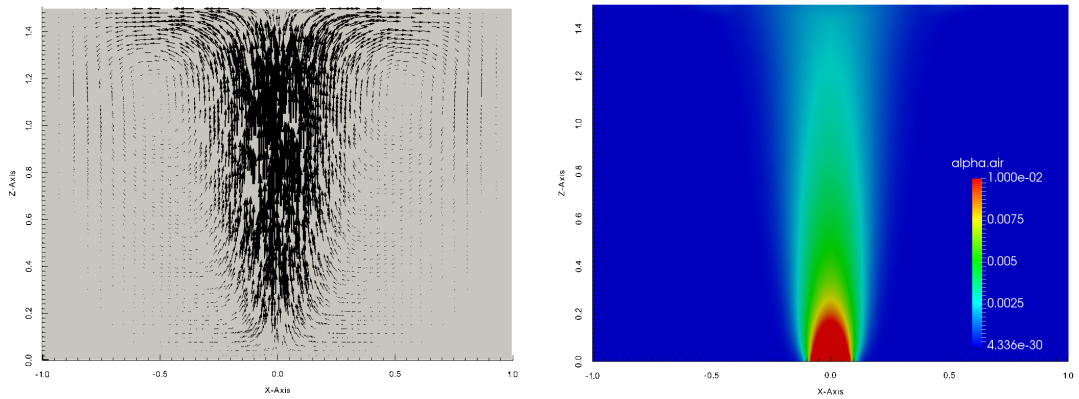

Figure 5.19: The liquid velocity vector plot (left) and phase fraction field for the case with an inlet of $\alpha = 1$ for the finest mesh.

Comparing the inlet turbulent kinetic energy in Figure 5.20 for the inlet condition of $\alpha = 1$, it can be seen that the turbulent kinetic energy is much closer to the measured value in general at $z = 0.35$ m, but does not exhibit the bump at 0.075 m caused by the edges of the inlet. The inlet condition of $\alpha = 0.5$ does have this effect, but it is overly exaggerated.

The phase fraction along the radial direction is compared between the two simulations in Figure 5.21. The spread in the simulation with an inlet condition of $\alpha = 1$ is greater than that of $\alpha = 0.5$, despite the high velocity vector near the inlet not being in evidence. Neither simulation comes close to the measured values or that which was simulated by Dhotre and Smith (2007) away from the inlet, but that of $\alpha = 0.5$ is closer along the centreline. The slight bump in the measured data is not given by the simulation of $\alpha = 1$ at the inlet.

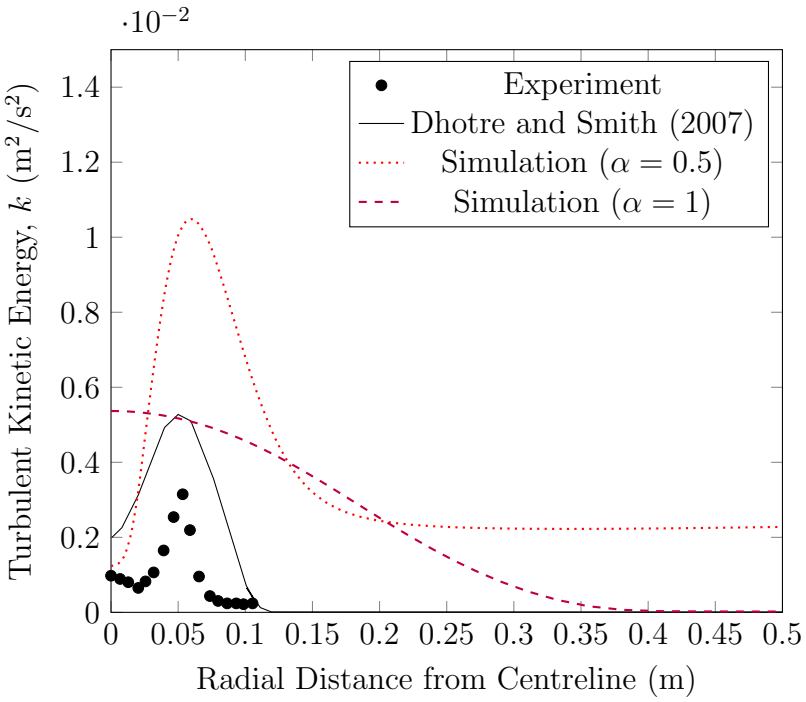

Figure 5.20: Comparison of experimental and simulation results for the turbulent kinetic energy at $z = 0.35$ m with inlet conditions on the phase fraction of $\alpha = 0.5$ and $\alpha = 1$.

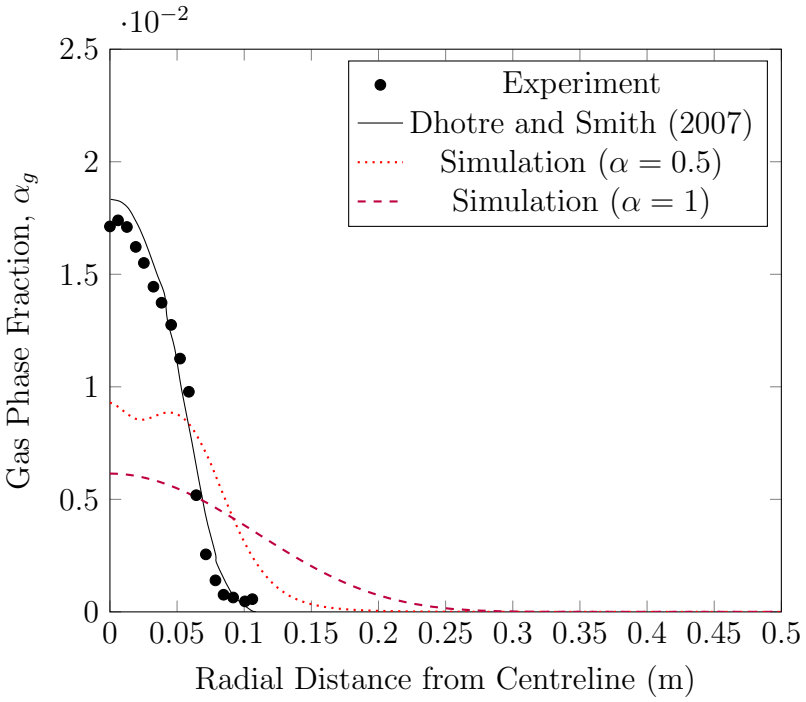

Figure 5.21: Comparison of experimental and simulation results for the phase fraction at $z = 0.35$ m with inlet conditions of $\alpha = 0.5$ and $\alpha = 1$.

The choice of inlet condition clearly has an effect on the velocity vectors near the inlet. The behaviour at the inlet is ultimately responsible for the spreading of the plume throughout the duration of the simulation at all heights. Although the inlet condition of $\alpha = 1$ gave a better prediction for these vectors, it did not produce accurate results for the phase fraction or the turbulent kinetic energy. The conclusion of Dhotre and Smith (2007) that the inlet phase fraction is inconsequential could not be reproduced with `twoPhaseEulerFoam`. This is likely due to the pressure profile produced near the inlet due to the change in phase fraction. Dhotre and Smith (2007) used a constant density, while the current work allowed density to change according to the ideal gas law, which may have been partially responsible.

5.4.1.2 Effect of Wall Functions

The wall functions described in Chapter 3 were applied to the coarsest and finest meshes of Section 5.4.1 (Mesh 1 and 3) along the walls and bottom of the domain. The $y+$ value for the case gave the distance from the wall of the first cell well above the value for $y+ = 30$ for both meshes. The results with and without wall functions were compared in this section. Figure 5.22 shows the axial liquid velocity at 0.35 m for the four cases compared to the experimental result and the result of Dhotre and Smith (2007). Without wall functions, mesh 1 is quite far from the measured value along the centreline, but with wall functions the radial profile is very similar to that obtained by Dhotre and Smith (2007) at this height. Similarly, Mesh 3 with wall functions is closer to the measured value along the centreline and has a similar profile to the experimental result. The two meshes with wall functions gave very similar results. The inlet fields for both meshes appear to have been significantly affected by the application of wall functions at the bottom of the domain.

The radial liquid axial velocity profiles at 0.75 m obtained are shown in Figure 5.23. At this height, the cases without wall functions appear to be significantly closer to the experimental data along the centreline than the cases which had wall functions. Mesh 1, which was the coarser mesh, was still fairly close to the result of Dhotre and Smith (2007) at this height. Mesh 3 was the least accurate for the liquid axial velocity along the centreline and in its radial profile at 0.75 m.

The radial profiles for the axial liquid velocities obtained at 1.10 mthrough the experiment and the simulations are shown in Figure 5.24. The cases without wall functions and with wall functions all came quite close to the measured values along the centreline. Farther from the centreline, mesh 1 and 3 with wall functions appear

to acquire a similar profile to the result of Dhotre and Smith (2007), but nearer to the centre their profiles are much different. The results with wall functions were again very close to each other.

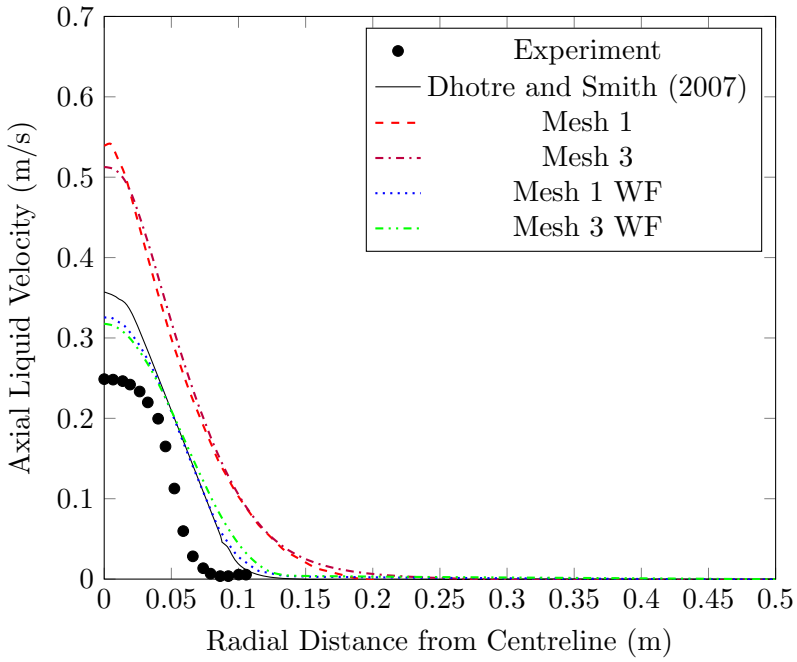

Figure 5.22: Comparison of experimental and simulation results for the axial liquid velocity at $z = 0.35$ m between the cases with and without wall functions.

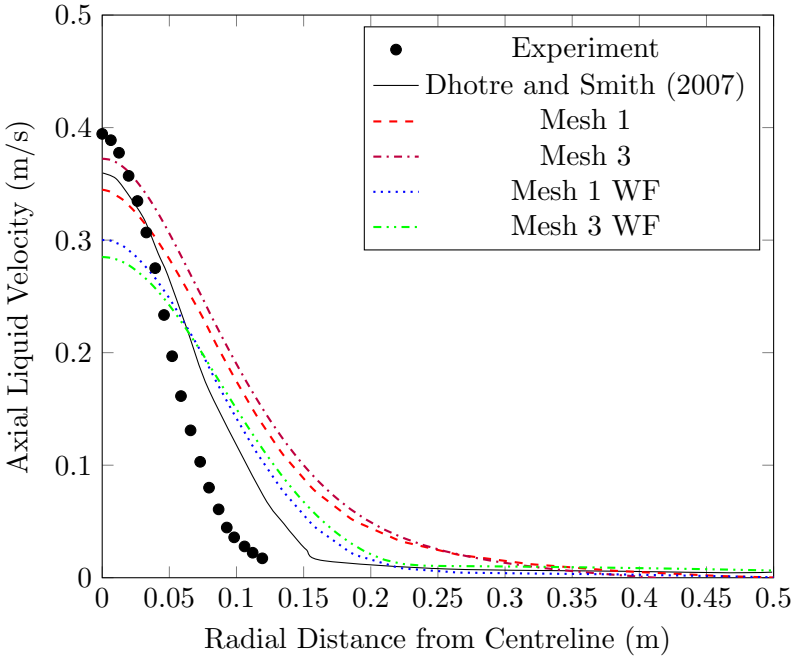

Figure 5.23: Comparison of experimental and simulation results for the axial liquid velocity at $z = 0.75$ m between the cases with and without wall functions.

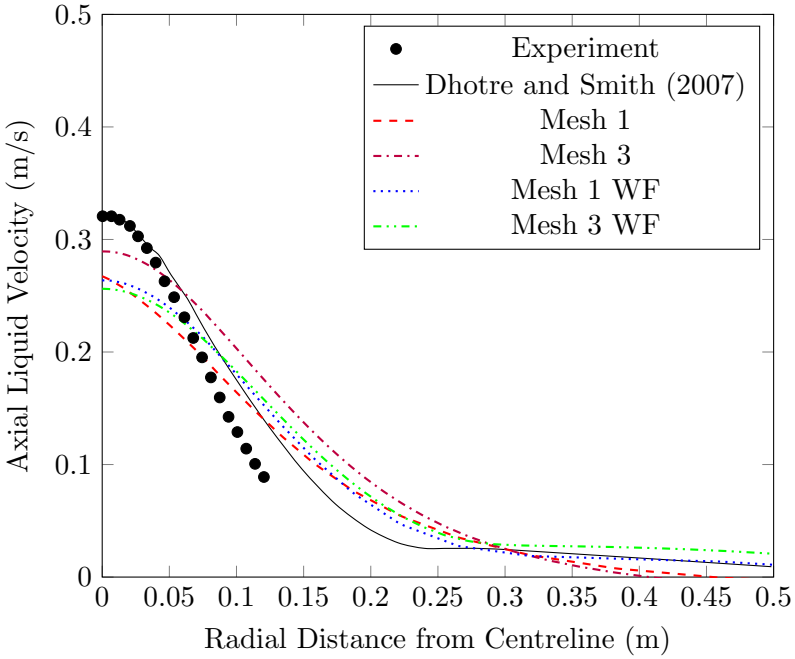

Figure 5.24: Comparison of experimental and simulation results for the axial liquid velocity at $z = 1.10$ m between the cases with and without wall functions.

Figure 5.25 shows the measured and simulation results for the axial gas velocity

at 0.35 m. Mesh 1 and 3 with wall functions are very close to the result obtained by Dhotre and Smith (2007) along the radial profile, diverging around 0.08 m from the centre. The two cases without wall functions are significantly less accurate than the cases with wall functions at this height.

The radial profiles of the axial gas velocity for the experiment and simulations are shown in Figure 5.26 at a height of 0.75 m. The finest mesh is the least accurate at this height at the centreline, while the other results are fairly similar. Mesh 1 with wall functions was the closest to the measured result at the centreline, but deviated from the experimental radial profile further away from the centre. Mesh 1 and mesh 3 with wall functions gave practically the same result at this height.

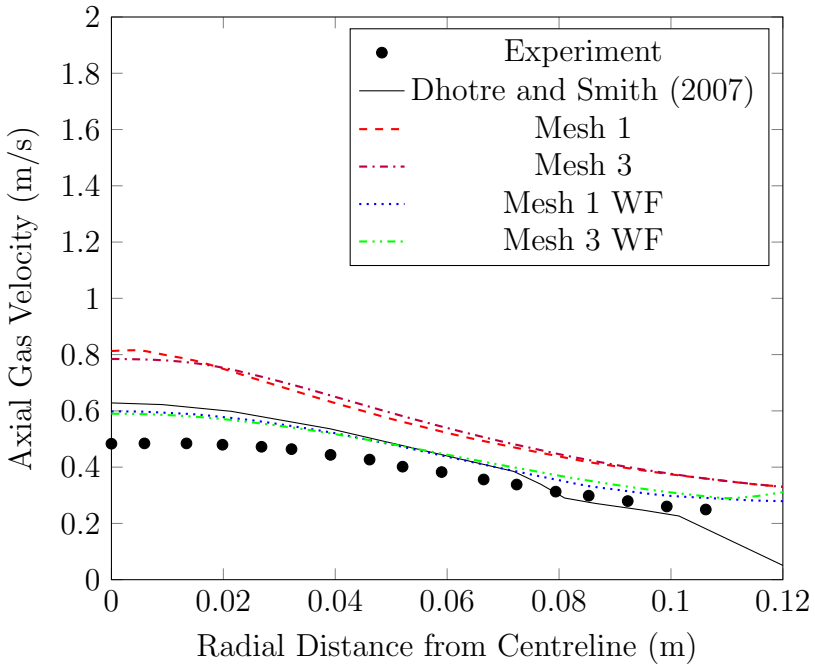

Figure 5.25: Comparison of experimental and simulation results for the axial gas velocity at $z = 0.35$ m between the cases with and without wall functions.

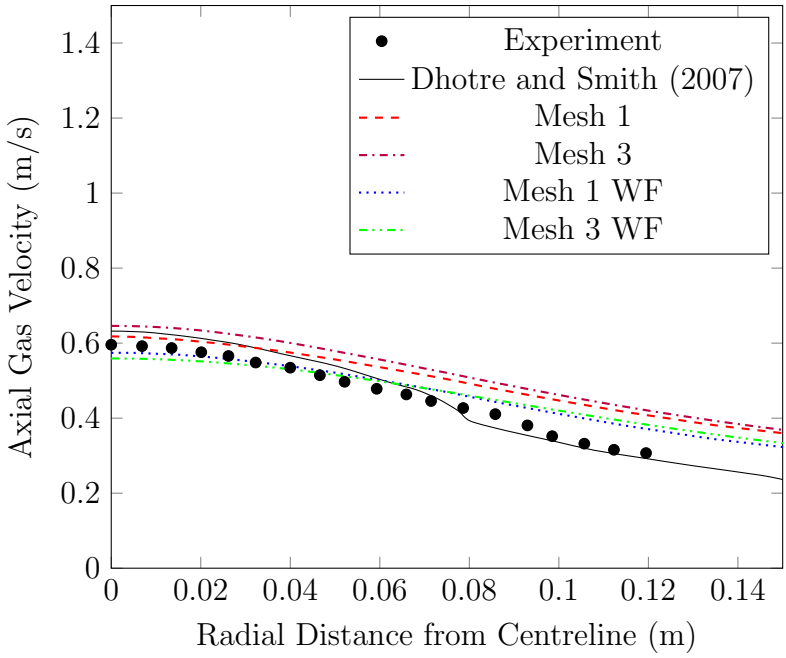

Figure 5.26: Comparison of experimental and simulation results for the axial gas velocity at $z = 0.75$ m between the cases with and without wall functions.

The radial axial gas velocity profiles for the simulations and experiment are shown in Figure 5.27 at a height of 1.10 m up the vessel. All of the simulations appear to come very close to the measured result along the centreline.

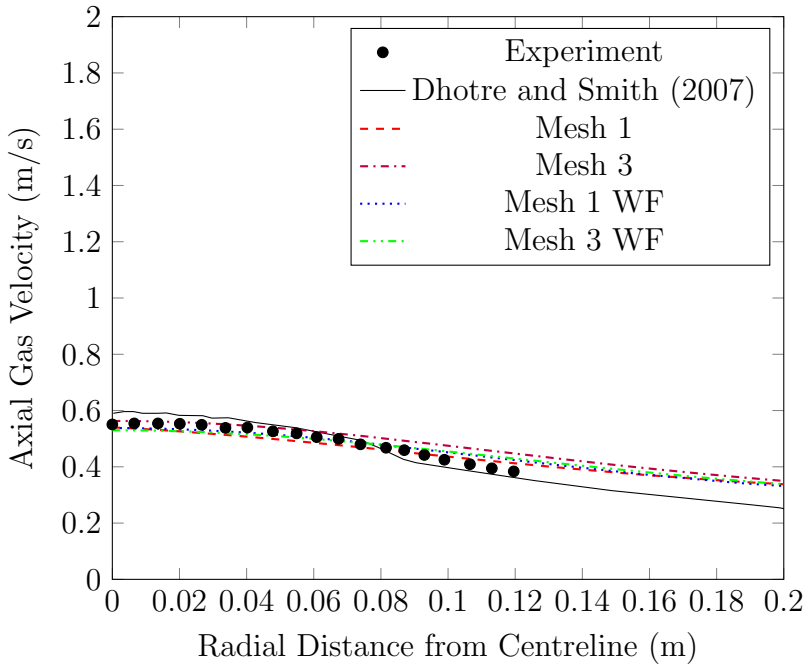

Figure 5.27: Comparison of experimental and simulation results for the axial gas velocity at $z = 1.10$ m between the cases with and without wall functions.

The radial profiles of the turbulent kinetic energy for the simulations and experiment are shown in Figure 5.28 at a height of 0.35 m up the vessel. Mesh 3 without wall functions obtained the closest centreline value to the experiment at this height. With wall functions, mesh 1 was the closest in magnitude to the experiment along the radius of the domain, and was quite close to the result obtained by Dhotre and Smith (2007).

At a height of 0.75 m, none of the simulations could obtain an accurate centreline value for the turbulent kinetic energy, as shown in Figure 5.29. At this height, meshes 1 and 3 with wall functions came the closest to the centreline value, but did not exhibit the exaggerated bump around 0.075 m caused by the inlet nozzle.

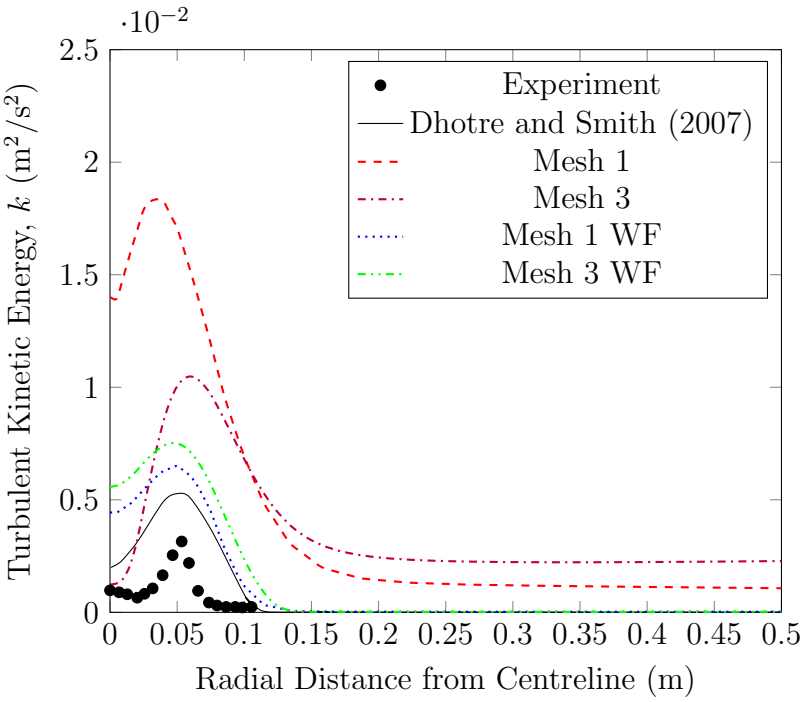

Figure 5.28: Comparison of experimental and simulation results for the turbulent kinetic energy at $z = 0.35$ m between the cases with and without wall functions.

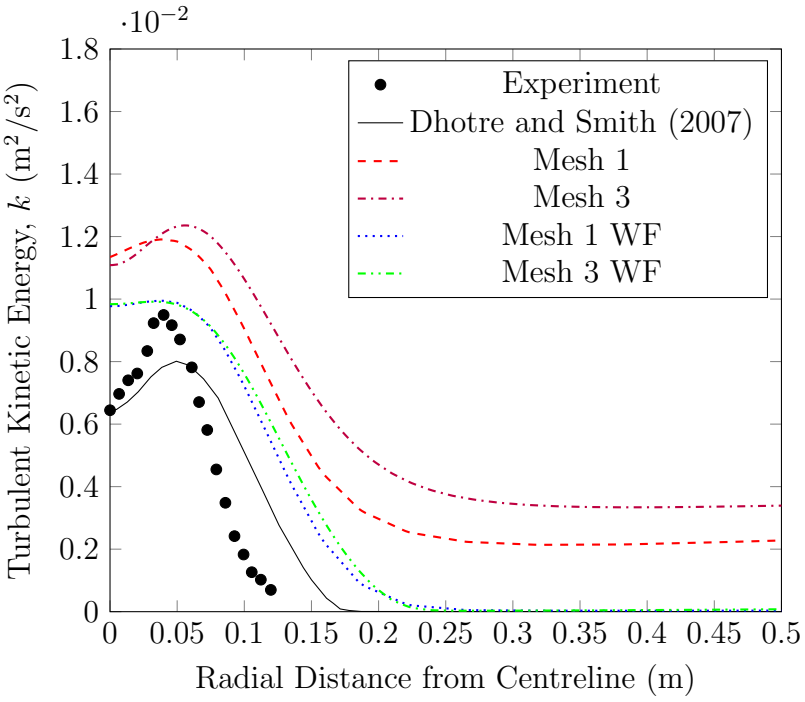

Figure 5.29: Comparison of experimental and simulation results for the turbulent kinetic energy at $z = 0.75$ m between the cases with and without wall functions.

The radial profiles of the turbulent kinetic energy at a height of 1.10 m for the simulations and experiment are shown in Figure 5.30. Meshes 1 and 3 with wall functions came the closest to replicating the radial profile at this height. Mesh 3 without wall functions was the farthest from the experimental result.

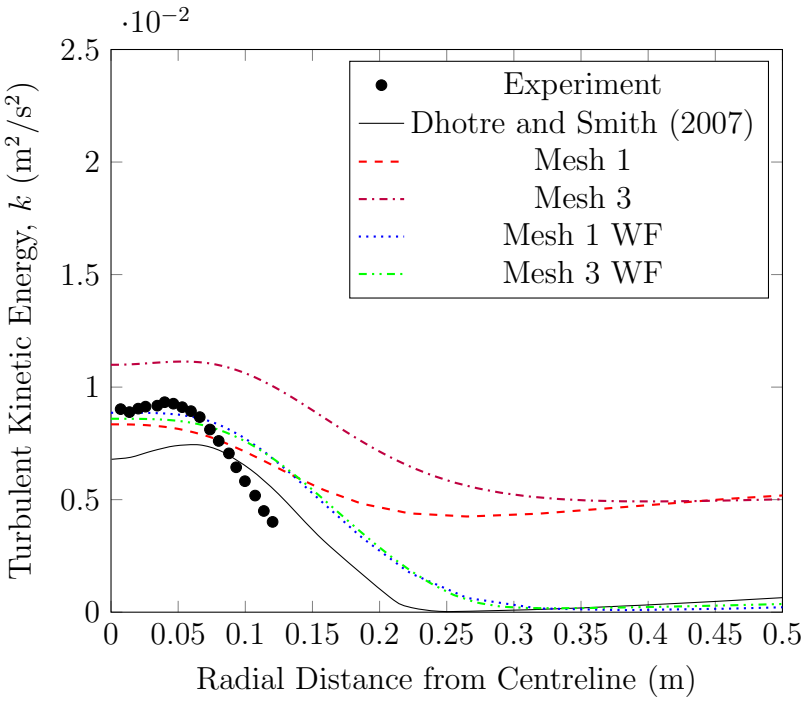

Figure 5.30: Comparison of experimental and simulation results for the turbulent kinetic energy at $z = 1.10$ m between the cases with and without wall functions.

The gas phase fraction was underpredicted by the two simulations without wall functions, but overpredicted by the two simulations with wall functions at a height of 0.35 m. The results for the gas phase fraction at this height are shown in Figure 5.31. The radial trend for the two simulations with wall functions were quite similar to that of Dhotre and Smith (2007).

The gas phase fraction along the radius of the vessel is shown in Figure 5.32 at a height of 0.75 m. Again, the simulations performed in the chapter all resulted in underpredictions of the gas phase fraction at this height along the centreline. At this height, meshes 1 and 3 with wall functions came the closest to the measured centerline value, and generally followed the experimental results well along the radius.

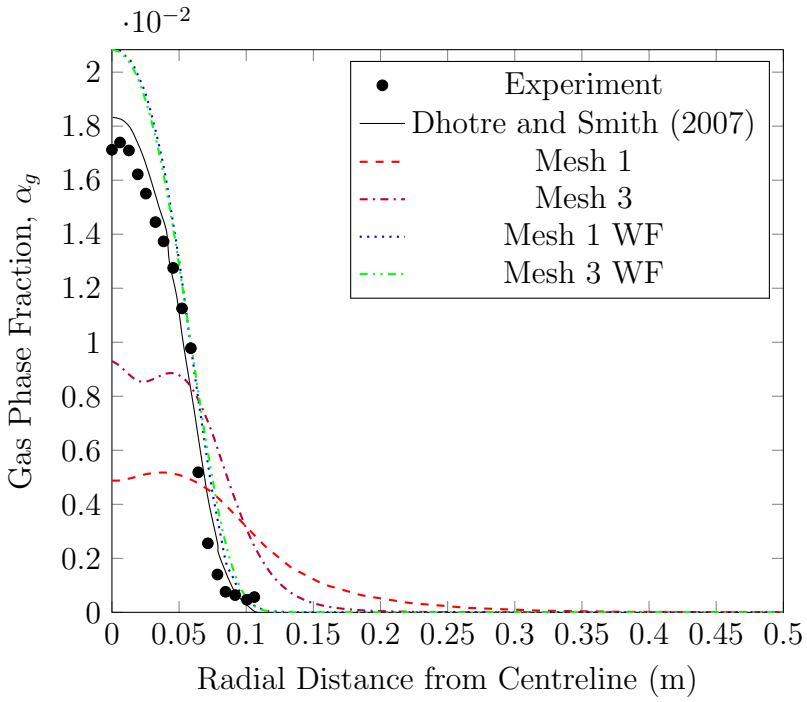

Figure 5.31: Comparison of experimental and simulation results for the phase fraction at $z = 0.35$ m between the cases with and without wall functions.

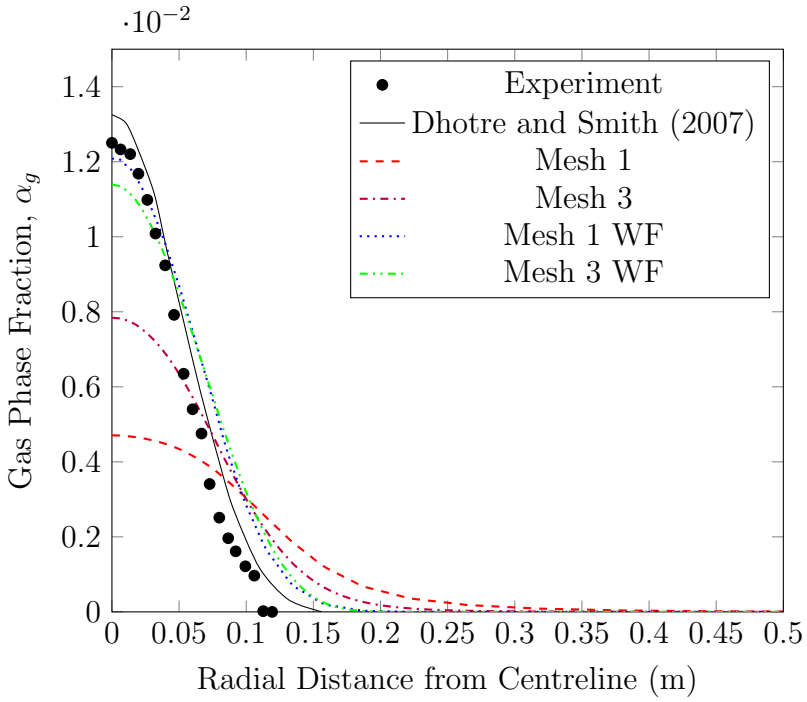

Figure 5.32: Comparison of experimental and simulation results for the phase fraction at $z = 0.75$ m between the cases with and without wall functions.

The radial profiles for the gas phase fraction at a height of 1.10 m in the vessel are shown in Figure 5.33. Meshes 1 and 3 with wall functions came the closest to the measured value at the centreline but exhibited more spread than the experiment at this height due to the high turbulent kinetic energy prediction. The other two results were still underpredictions of the gas phase fraction along the centreline and did not come close to the same profile along the radius.

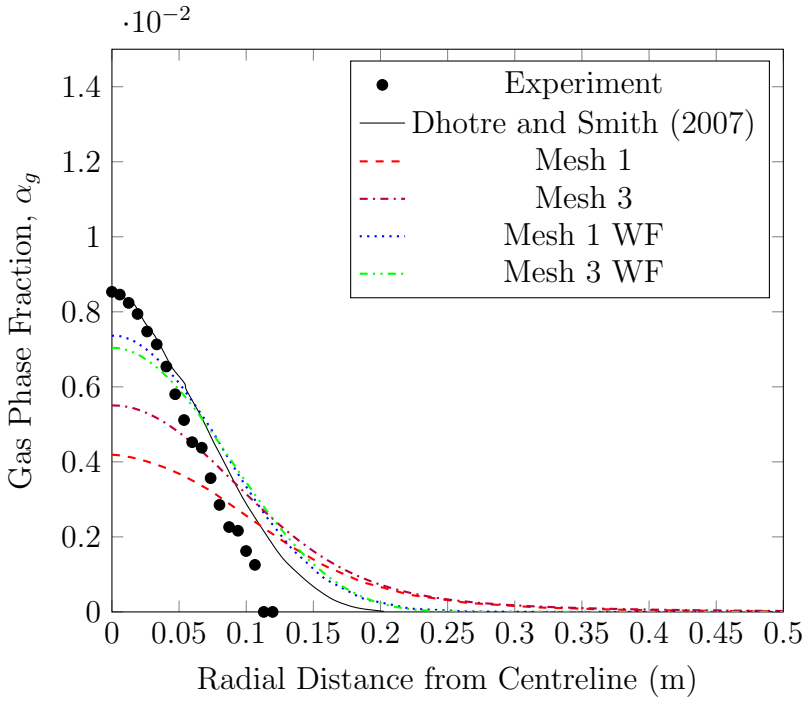

Figure 5.33: Comparison of experimental and simulation results for the phase fraction at $z = 1.10$ m between the cases with and without wall functions.

It appears to be the case that the application of wall functions has a large effect on the simulation results. Meshes 1 and 3 with wall functions seemed to be closer to the experimental data at heights nearer to the inlet and generally at all heights. The two simulations without wall functions were fairly accurate in the axial gas and liquid velocities, but were not very accurate in the turbulent kinetic energy or gas phase fraction at all heights in the plume.

An interesting thing to note is that the third and first mesh with wall functions could not obtain the exaggerated bump in the radial profile predicted at $z = 0.75$ m in the simulation of Dhotre and Smith (2007) and the result obtained through the experiment. The bump in the curve at $r = 0.075$ m along the radius is most likely caused by the distributor, and it would be expected that it would be primarily

caused in the simulations by the mesh. Considering the meshes were kept the same, this result indicates that the wall functions smoothed out some of the turbulent inlet effects near the centreline and away from the distributor that was observed in the experiment and other simulations, while enforcing the turbulent effect near the inlet.

5.4.2 Case 2 with the Turbulent Dispersion Force of Davidson (1990)

Since it was shown in case 1 that the far-field results seemed to be reasonably close to the experimental data for the second mesh, application to an experiment with more data at higher elevations could allow for evaluation of the IATE model. The first experiment of Simiano (2005) was used for this purpose. The case was simulated with both a constant diameter of 4 mm as well as the IATE model with an initial bubble diameter of 4 mm. All the parameters and models for case 1 were also used in these simulations, but wall functions were omitted.

The inlet vectors for the liquid velocity are shown in Figure 5.34. The phase fraction chosen, $\alpha = 0.01$, for the simulations did not produce the circulation pattern or high velocities at the inlet which were observed in the previous case. The vectors displayed similar behaviour for all the simulations of case 2.

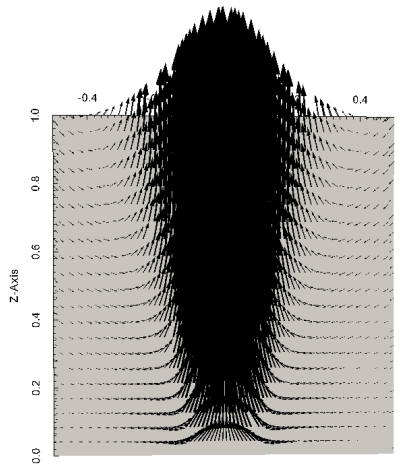

Figure 5.34: The liquid velocity vectors near the inlet for case 2.

The results for the axial liquid velocity at 0.6 m are shown in Figure 5.35. The constant and IATE model bubble diameters gave exactly the same result for the liquid axial velocity. In both cases the simulations underpredicted at the centreline at this elevation.

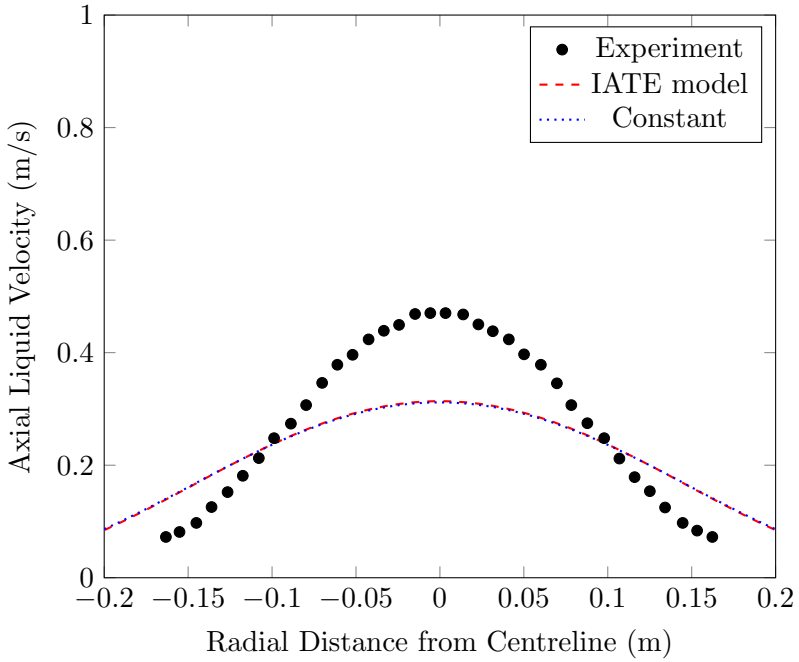

Figure 5.35: Comparison of experimental and simulation results for the axial liquid velocity at $z = 0.6$ m for an initial bubble size of 4 mm.

The results for the axial gas velocity at 0.6 m are shown in Figure 5.36. The two simulations were again identical, and the velocity was predicted rather well at the centreline. The trend of the simulation results seems to be closer to the experiment for the axial gas velocity.

The phase fractions for both simulations and the interfacial area concentration predictions for the IATE model are given in figures 5.37-5.40 for four heights in the vessel. The phase fractions for both simulations are once again identical, and appear to maintain a trend close to that of the experimental data for all heights. At all heights, the centreline prediction of the phase fraction was lower than the measured data. This difference appeared to increase at higher locations in the vessel. The interfacial area was also underpredicted for all heights, but as with the phase fraction prediction, appeared to follow the correct trend. The interfacial area concentration appeared to be primarily influenced by the phase fraction as it produced a similar trend to the phase fraction at all heights.

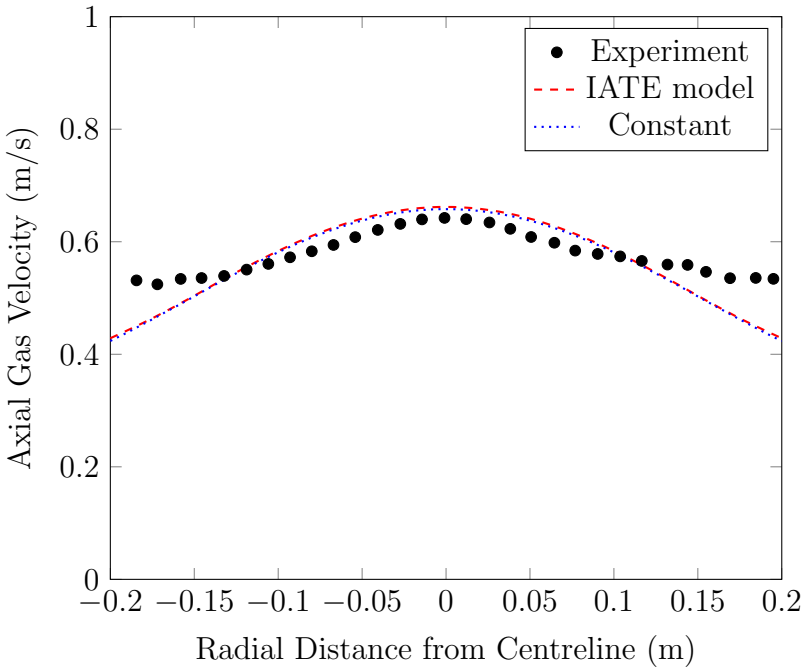

Figure 5.36: Comparison of experimental and simulation results for the axial gas velocity at $z = 0.6$ m for an initial bubble size of 4 mm.

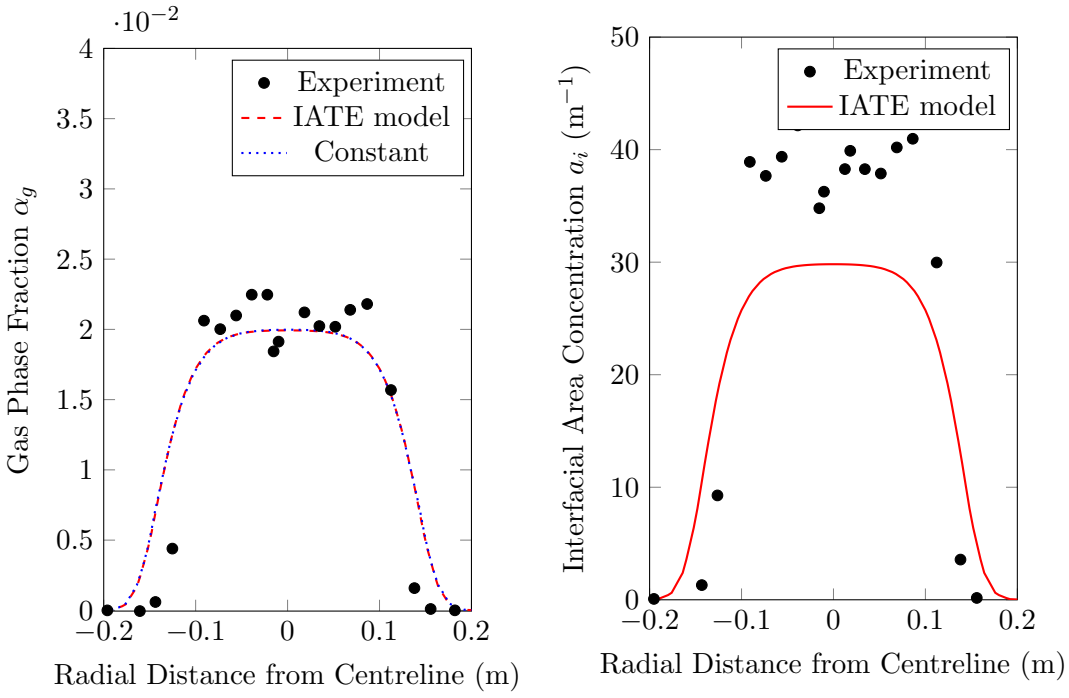

Figure 5.37: Comparison of experimental and simulation results for the phase fraction (left) and interfacial area concentration (right) at $z = 151$ mm for an initial bubble size of 4 mm.

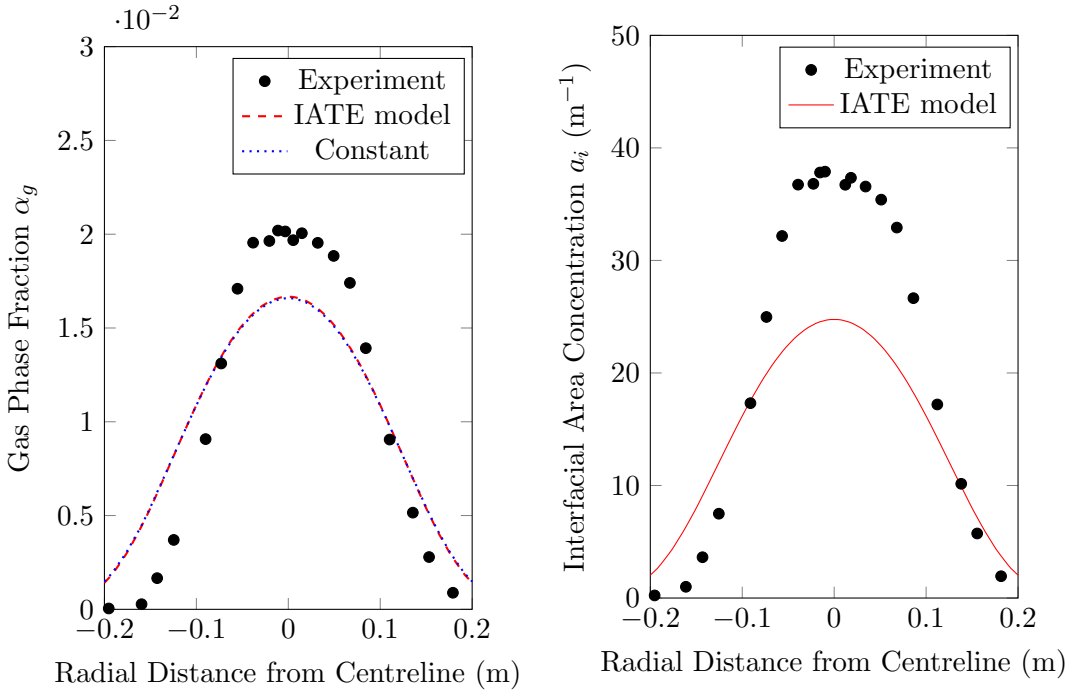

Figure 5.38: Comparison of experimental and simulation results for the phase fraction (left) and interfacial area concentration (right) at $z = 552$ mm for an initial bubble size of 4 mm.

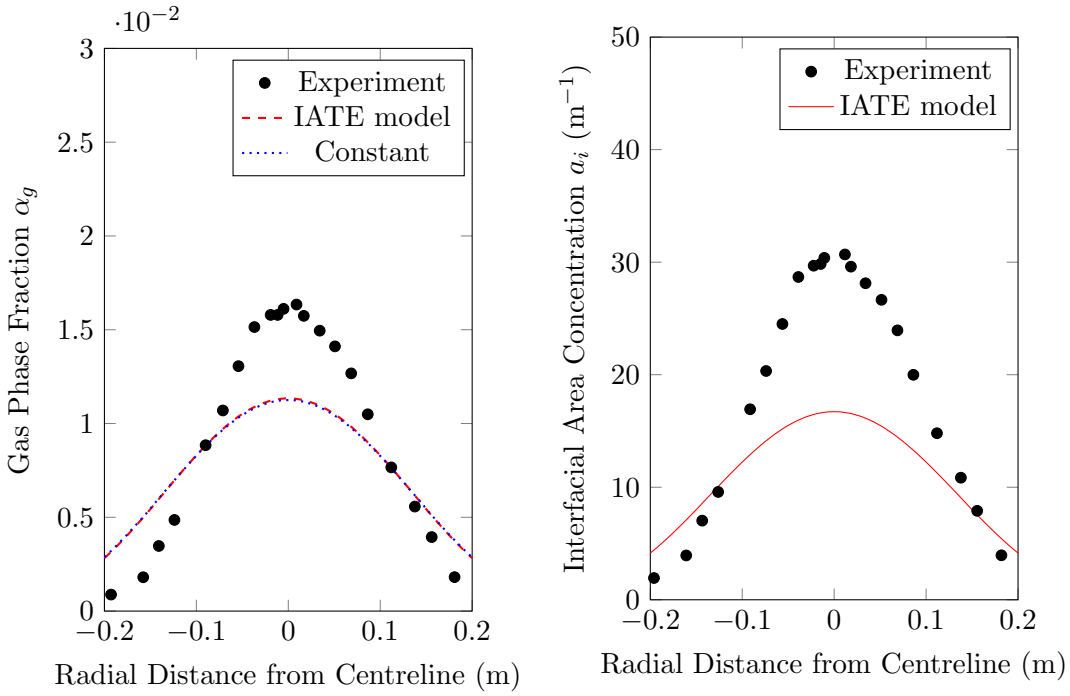

Figure 5.39: Comparison of experimental and simulation results for the phase fraction (left) and interfacial area concentration (right) at $z = 978$ mm for an initial bubble size of 4 mm.

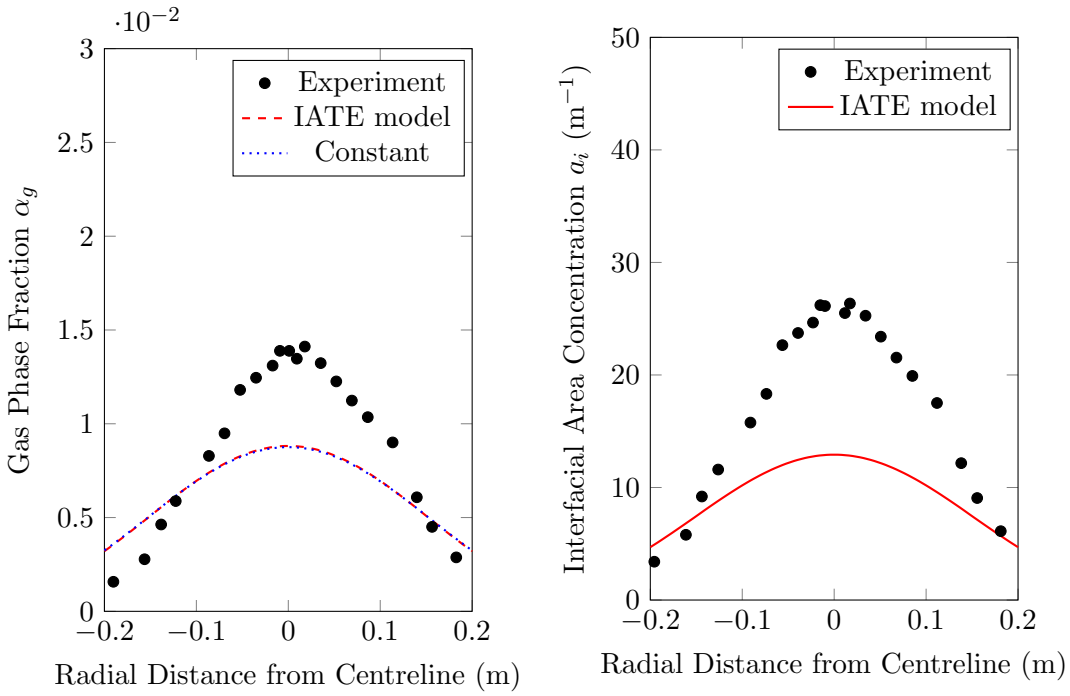

Figure 5.40: Comparison of experimental and simulation results for the phase fraction (left) and interfacial area concentration (right) at $z = 1.291$ m for an initial bubble size of 4 mm

Clearly the tuning of the first case was not applicable to the second case, because none of the predictions obtained in case 2 were close to the measured quantities in the far-field or near-field except the axial gas velocity. In fact, at greater heights, the discrepancy between the measured and simulated results became more pronounced. It is possible that with the addition of wall functions or a better condition for pressure at the inlet, these problems would be minimized.

The IATE model, despite having underpredicted all the experimental values, did have the correct response at different heights in the plume, decreasing the interfacial area concentration as the height increased. This could indicate that some coalescence was predicted by the model, or that it was very dependent on the value of the phase fraction. Based on the fact that the IATE model gave the same hydrodynamic prediction as when using a constant bubble size, the latter explanation is more likely. This result could potentially have been improved if the hydrodynamics had been correctly predicted, so no conclusion can be drawn about the IATE model at this point. It is also unclear that the initial bubble size selected, 4 mm, gave the optimal result for the simulation.

5.4.3 Case 2 with the Turbulent Dispersion Force of Lopez de Bertodano (1998)

In this section of case 2, the drag model was changed to the Kolev (2012) model as suggested in Lou and Zhu (2013b) for cases with gas-mixing. In this section, the use of the Lopez de Bertodano (1998) model for the turbulent dispersion force was tested to attempt to get a closer prediction to the experimental result of Simiano (2005). The IATE model was also implemented so that any change in the IATE model caused by the change in sub-model could be observed. Five initial bubble diameters were selected. The turbulent dispersion coefficient was also tuned to attempt to optimize the result.

The liquid axial velocity obtained through the simulations was compared to the experimental result for each of the five initial bubble diameters, as shown in Figure 5.41 at a height of 0.6 m. The 15 mm and 5 mm initial bubble sizes yielded the closest values to the experimental velocities, but all of the cases underpredicted the liquid velocity near the centre of the plume. In the simulations of Dhotre and Smith (2007), they used the same turbulence model and lift coefficient, but they obtained much more satisfactory results. The underprediction of the liquid velocity is consistent with what was observed in Chapter 4, as the Simonin and Viollet (1988) model underpredicted the velocity in the ladle case as well in conjunction with the Lopez de Bertodano (1998) turbulent dispersion model.

The axial gas velocity at the same height for the same range of bubble sizes as before are shown in Figure 5.42. As the initial bubble size is increased, the gas velocity increased in all cases. The 15 mm initial bubble diameter produced a much higher gas velocity than any of the other initial diameters, but still ended up producing a lower liquid velocity than the 5 mm case. The profile of the experimental values was not reproduced well by any of the simulations, and none of the simulations could reproduce the gas velocity.

The phase fraction and the interfacial area concentrations from the experiment and the simulations were compared at a range of heights and initial bubble sizes in Figures 5.43-5.46. At lower heights in the vessel, the 3 mm initial bubble size appears to give better results. As the bubbles moved upward, it can be seen that the amount of coalescence induced by the IATE model was not enough to match the experimental values. In general, the 4 mm initial bubble size was relatively close to the experimental values for interfacial area concentration and phase fraction for all vessel heights, which was not the case for the other sizes.

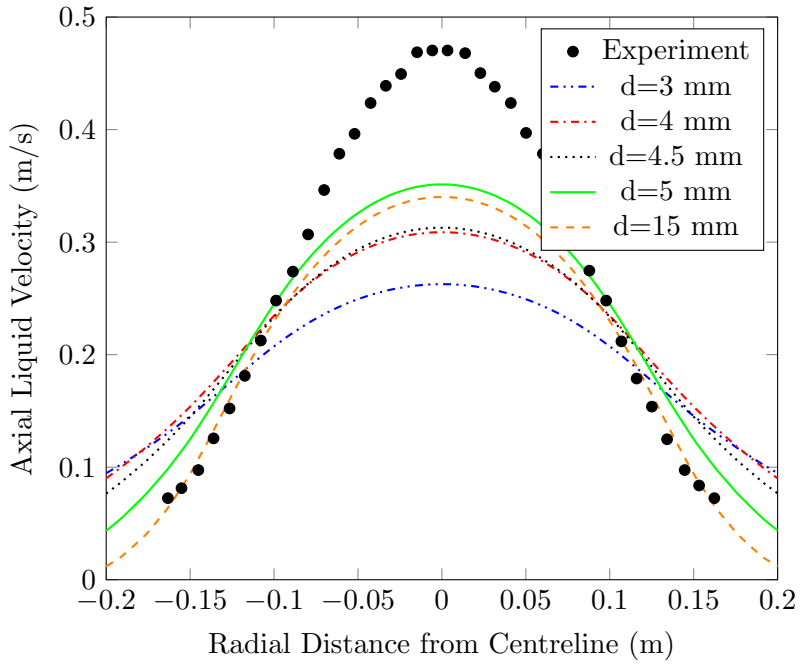

Figure 5.41: Comparison of experimental and simulation results for the axial liquid velocity at $z = 0.6$ m for a range of initial bubble sizes.

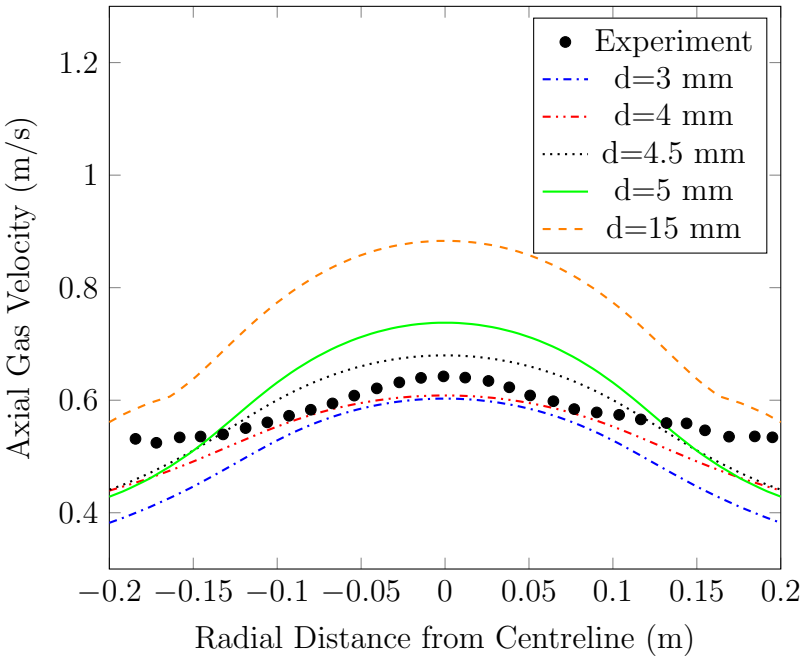

Figure 5.42: Comparison of experimental and simulation results for the axial gas velocity at $z = 0.6$ m for a range of initial bubble sizes.

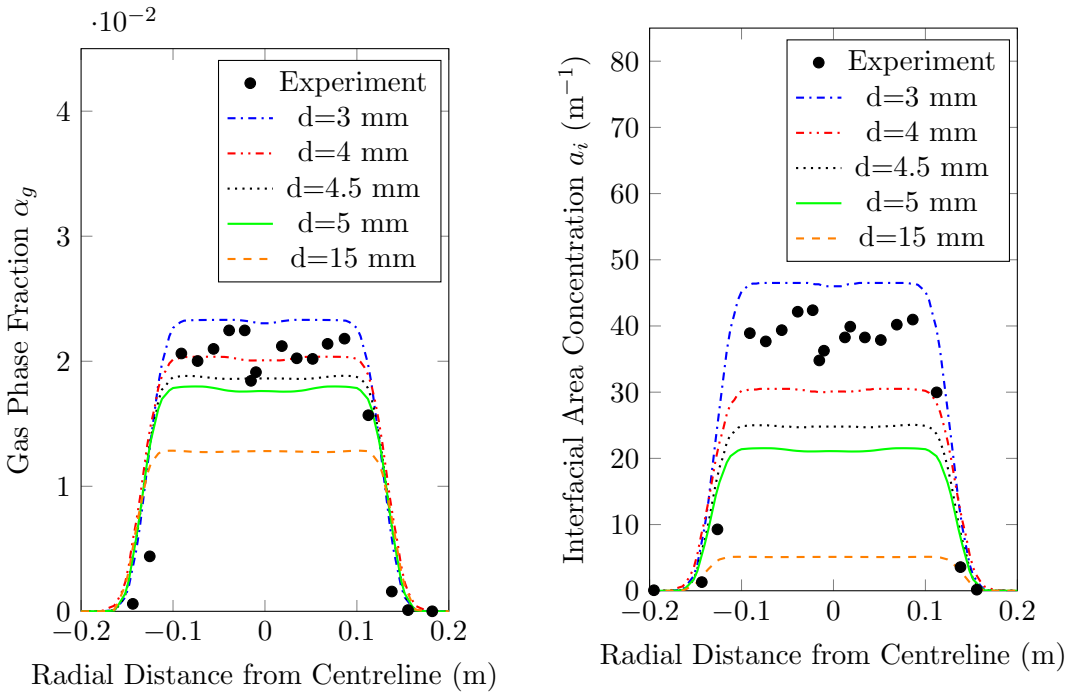

Figure 5.43: Comparison of experimental and simulation results for the phase fraction (left) and interfacial area concentration (right) at $z = 151$ mm for a range of initial bubble sizes.

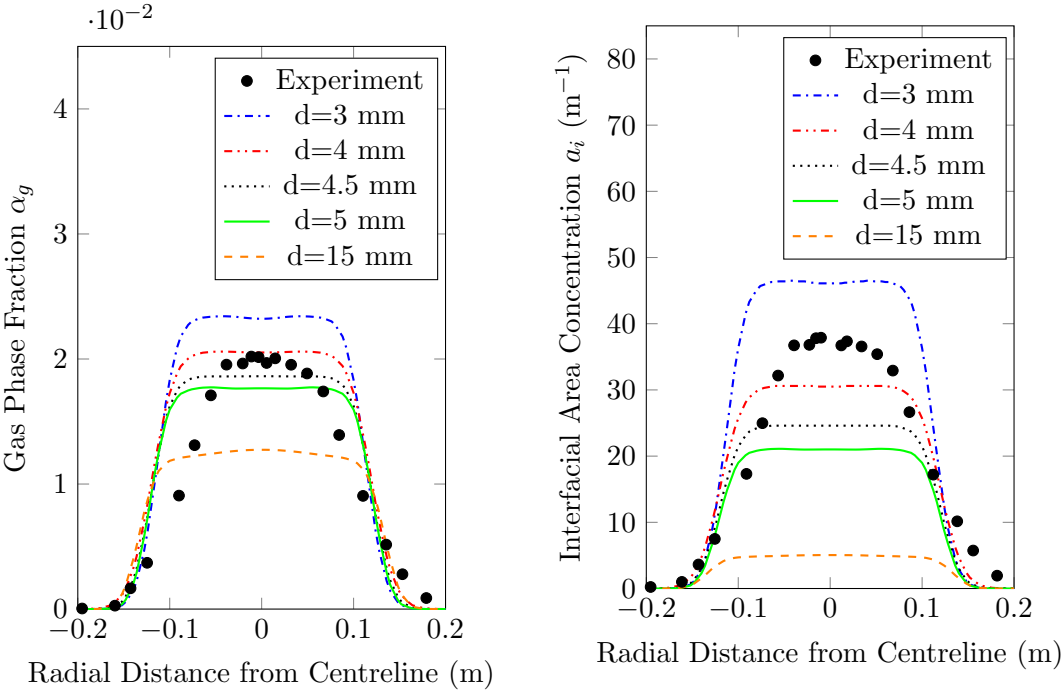

Figure 5.44: Comparison of experimental and simulation results for the phase fraction (left) and interfacial area concentration (right) at $z = 552$ mm for a range of initial bubble sizes.

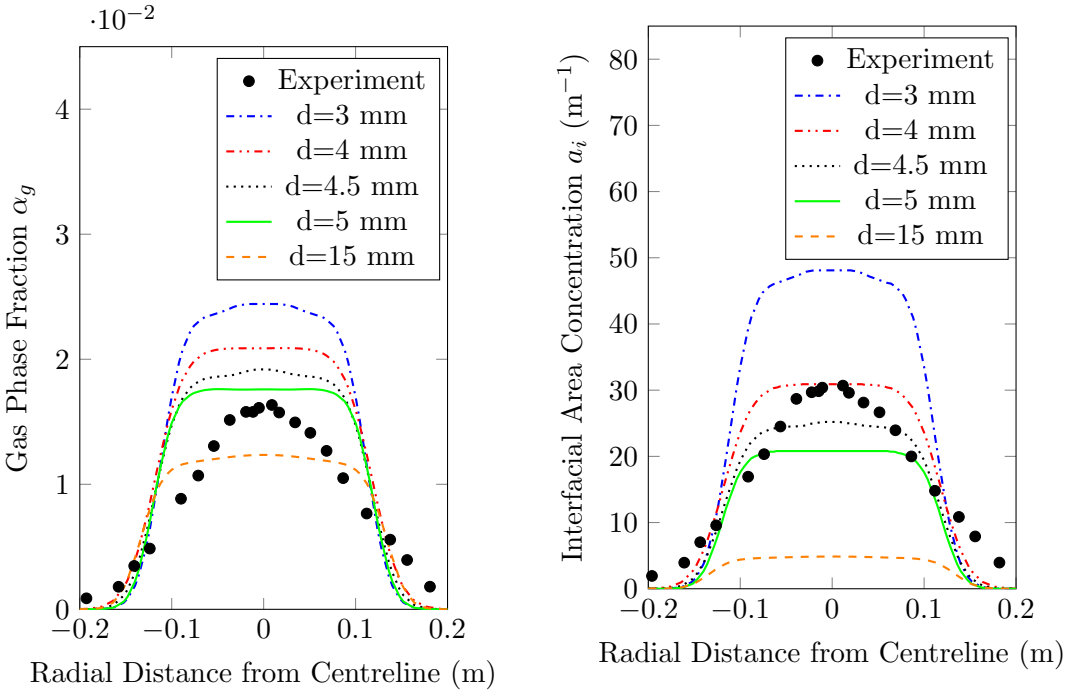

Figure 5.45: Comparison of experimental and simulation results for the phase fraction (left) and interfacial area concentration (right) at $z = 978$ mm for a range of initial bubble sizes.

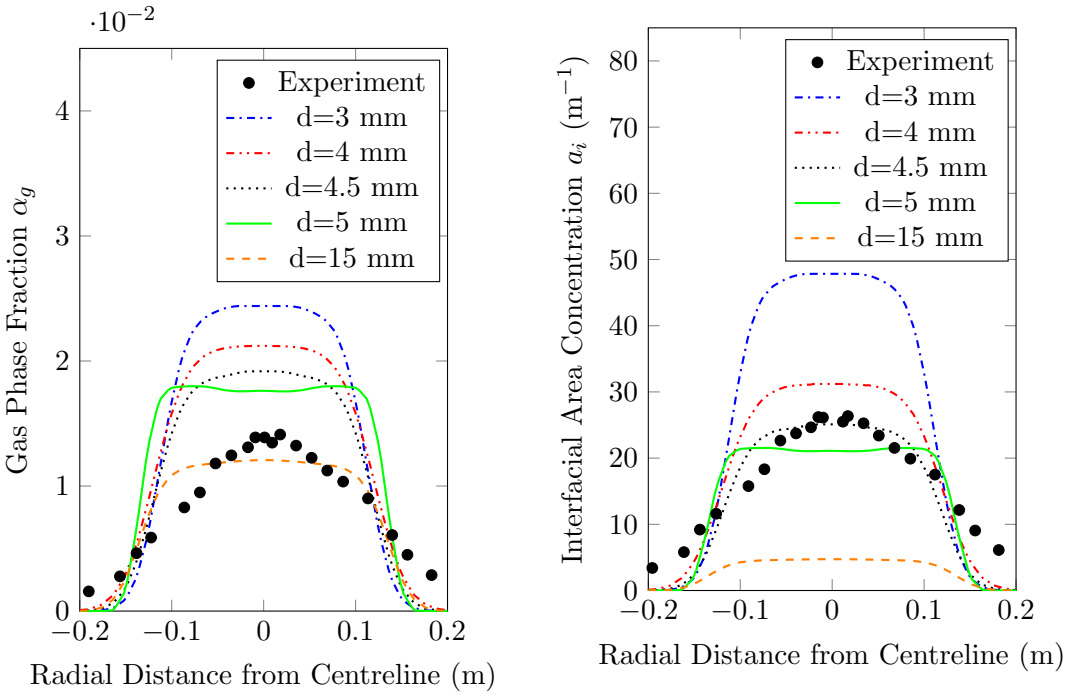

Figure 5.46: Comparison of experimental and simulation results for the phase fraction (left) and interfacial area concentration (right) at $z = 1.291$ m for a range of initial bubble sizes.

The initial bubble size guess had large effect on the predictions for all the properties. Without information about the inlet bubble size in the physical case, guessing it for simulations which use the IATE model is probably not prudent. In the full-scale gas well blowout, the inlet bubble diameter could not be known, and would be more likely to be a distribution of bubble sizes in lieu of a single inlet size. A really good prediction with the IATE model was probably not feasible, considering the hydrodynamics of the simulations do not seem to match the experimental data very well.

Since the Simonin and Viollet (1988) turbulence model underpredicted the liquid axial velocity and the turbulent kinetic energy in Chapter 4, it could be one of the causes for the incorrectly predicted hydrodynamics in the present case. As was noted in Chapter 4, the turbulent kinetic energy was underpredicted, which was not observed in the simulations of Dhotre and Smith (2007) or in Sheng and Irons (1993). As previously discussed, the simulation parameters of Dhotre and Smith (2007) and the present study were the same aside from the drag and turbulent dispersion forces, but whether they used wall functions is unknown. The reason for the major difference in results between these two studies is not entirely clear because the equations and sub-models are so coupled that any change in one equation could cause a large effect in another.

5.4.3.1 Turbulent Dispersion Force Effects

The underprediction of the turbulent kinetic energy produces feedback with the turbulent dispersion force in the momentum equation as well as the phase continuity equation. A separate study was necessary to determine whether it was the underprediction of the turbulent kinetic energy and not the magnitude of the turbulent dispersion force that was causing the vast discrepancies between the hydrodynamic predictions of the current study and the experimental results of Simiano (2005).

Since the 4 mm initial bubble diameter produced the closest results overall for the liquid axial velocity, gas velocity, phase fraction and interfacial area concentration, it was the case which was used to compare a range of turbulent dispersion coefficients. Figure 5.47 shows the experimental and simulation results for the liquid axial velocity at 0.6 m up the vessel for a range of turbulent dispersion coefficients. The $C_{TD} = 0.1$ case produced the highest liquid velocity, and $C_{TD} = 0.2$ the lowest, but the other two coefficients were virtually identical in their prediction. Changing this parameter does not appear to have a large effect on the hydrodynamic prediction in the liquid,

which could be due to the velocity and turbulent kinetic energy near the inlet.

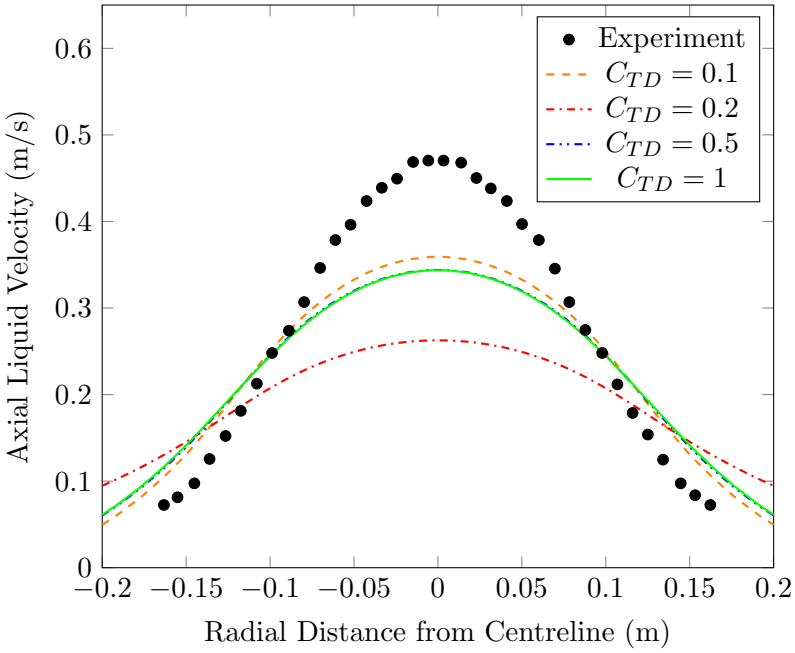

Figure 5.47: Comparison of experimental and simulation results for the axial liquid velocity at $z = 0.6$ m for a range of turbulent dispersion coefficients.

Figure 5.48 shows the gas velocity at 0.6 m for the same turbulent dispersion coefficients. The experimental results on the graph are not matched well in shape by the simulations, as before. For all the turbulent dispersion coefficients except $C_{TD} = 0.2$, the gas velocity was still overpredicted. The turbulent dispersion coefficient of $C_{TD} = 0.2$ gave the result closest to the experimental values for the axial gas velocity.

Although there were no experimental results reported at 0.6 m for the phase fraction or interfacial area concentration, the values were compared to see if there was any significant effect. Figure 5.49 shows a comparison between a range of turbulent dispersion coefficients. Clearly changing the magnitude of the turbulent dispersion force did not have a great impact on the phase fractions or the interfacial area concentrations in this case.

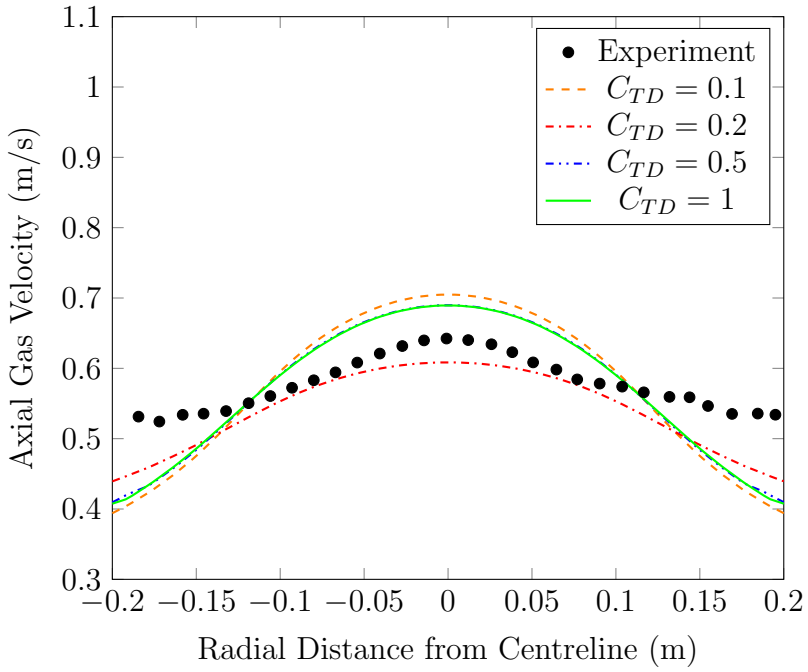

Figure 5.48: Comparison of experimental and simulation results for the axial gas velocity at $z = 0.6$ m for a range of turbulent dispersion coefficients.

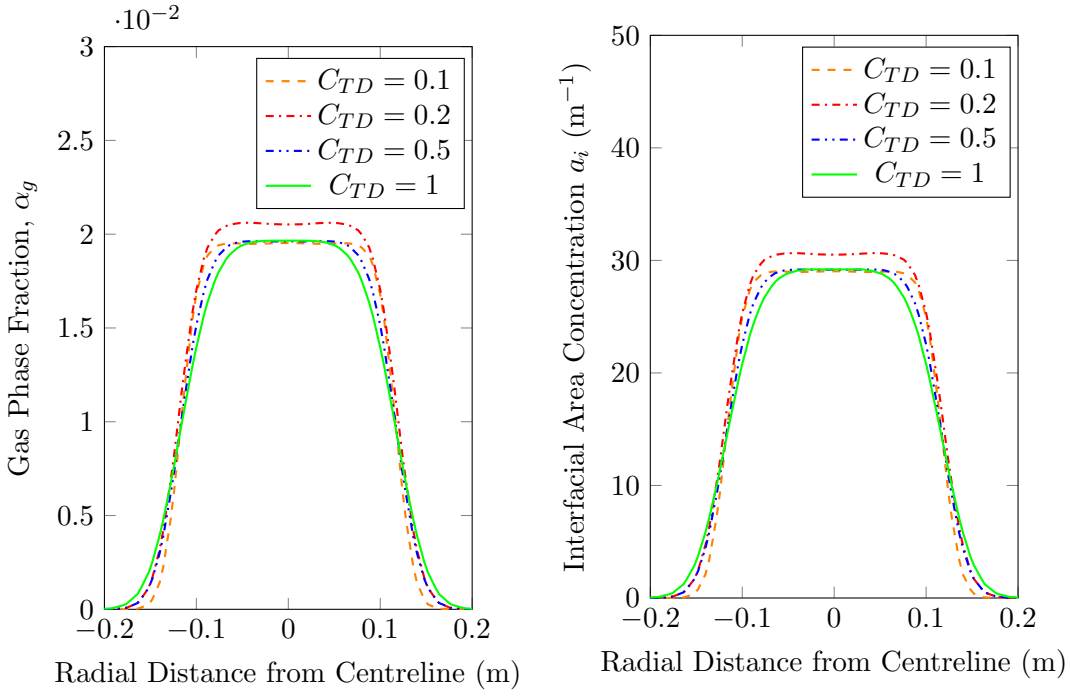

Figure 5.49: Comparison of simulation results for the phase fraction (left) and interfacial area concentration (right) at $z = 0.6$ m for a range of turbulent dispersion coefficients for the 4 mm initial bubble size.

The underprediction of the turbulent kinetic energy by the turbulence model of Simonin and Viollet (1988) with the coefficient changes of Sheng and Irons (1993) is likely to be one of the causes for the poor prediction of the hydrodynamics. This is concluded because increasing the magnitude of the turbulent dispersion had a minimal effect on the results of the simulation. The current formulation of the IATE model was also unable to predict the coalescence interactions in the present study, but there may not have been much coalescence in the experiment to begin with.

5.5 Summary

The following two sections detail the overall results and conclusions that have been drawn from the simulations of this chapter.

5.5.1 Hydrodynamics

The simulations in the first case showed that the near-field predictions, with the tuning parameters and models used successfully in the study of Dhotre and Smith (2007), were not accurate with the `twoPhaseEulerFoam` solver. The phase fraction was underpredicted throughout the vessel for the three meshes. Further, the velocity vectors at the inlet appeared to be highly dependent on the inlet condition. One of the parameters which could not be investigated in depth is the effect of the boundary conditions, although wall functions were tested. Application of wall functions appeared to improve the results, but it is not clear that they didn't just help to replicate the conditions of the inlet distributor. Since few boundary conditions were given by Dhotre and Smith (2007), the exact case could not be reproduced. The current simulations also did not model the free surface, which could have contributed to the discrepancy in the results. The inlet phase fraction was changed to a higher value, which improved the liquid velocity vector map, but did not improve the hydrodynamic prediction. This is not consistent with the conclusion reported by Dhotre and Smith (2007) that the phase fraction at the inlet did not cause significant changes to the simulation.

In the first section of the second case, which used the same sub-models and parameters as the first case, the velocity in both the liquid and the gas phase was underpredicted. The phase fraction was more accurate in the near-field than the far-field, which is a contrary result to the first case. This indicates that the tuning and sub-model choices of the first case do not necessarily provide a consistent result when applied to a similar case with a different phase fraction inlet.

Applying different sub-models in the second section of the second case still resulted in an underprediction of the liquid velocity along the centreline for all initial bubble diameters. The gas velocity was highly dependent on the initial bubble size selected by the IATE model, as expected. The hydrodynamic prediction was not improved by changing the magnitude of the turbulent dispersion force of Lopez de Bertodano (1998).

5.5.2 IATE Model

The first section of case 2 showed that using the IATE model gave the exact same prediction as using a constant bubble diameter. This suggests that the IATE model was more dependent on the value of the phase fraction than on the IATE model itself. This explains the similar trendlines between the phase fraction and the interfacial area concentration seen in the first case. Since the velocity in the liquid was inaccurate, no real conclusion about the effectiveness of the IATE model can be made. There also may not have been much breakup or coalescence in the experimental study, however.

In section 2 of the second case, the IATE model predictions obtained using five different inlet bubble sizes were compared. The hydrodynamic predictions of the 4 mm initial bubble size gave the best result overall, but the result was neither consistent with the interfacial area concentration predicted by the first section of case 2, or with the measured values. No conclusions about the fitness of the IATE model for a larger-scale simulation can be given based on this result either.

Chapter 6

Mass Transfer Modeling

The major changes to the basic `twoPhaseEulerFoam` algorithm were the addition of a species equation and mass transfer capability, so those new aspects of the solver had to be tested. Even though the hydrodynamic predictions could not be tuned to reproduce the results from Chapter 4 or 5, the additions that were made to the solver for mass transfer should still behave properly for a stationary case and for a case where the hydrodynamics are properly predicted. This section verifies that the mass transfer algorithm described in Chapter 2 was implemented correctly and is performing as expected.

6.1 Mass Transfer Verification

Two very simple cases were used to verify that the mass transfer algorithm was behaving as expected. The setup for both cases was a 2-D box, $0.1 \times 0.1 \times 0.01$ m with no interphase forces and no gravitational force in order to keep the fluid effectively stationary throughout the duration of the simulation. As mentioned, `twoPhaseEulerFoam` may not handle low flow cases well due to the reliance on the drag term in the flux reconstruction. Since the solution to this particular case relies heavily on the correct pressure prediction, and therefore the correct density prediction, the flux and velocity reconstructions were omitted for the test cases. The drag coefficient was set to zero and the fluxes were calculated by setting $\phi_i = \phi_{i,s}$, the dragless fluxes.
In the first case, the box contained a 50/50 dispersed mix of liquid and gas, with a 50/50 mix of species 1 and species 2 in the gas phase initially. The slim edges allowed pure water into the domain to maintain conservation of mass, but no mass could leave. Since the case was not technically supposed to be a flow case, although there was some flow in from the edges, turbulence was not incorporated into the solution.

The boundary conditions are summarized in Table 6.1.

Table 6.1: Boundary and initial conditions for the stationary mass transfer algorithm verification

	Initial Condition	0.1×0.01 **sides**
Gas Phase Fraction, α_g	0.5	0
Liquid Phase Fraction, α_l	0.5	1
Gas Mass Fraction of Species 1, Y_1	0.5	0
Gas Mass Fraction of Species 2, Y_2	0.5	0
Gas Mass Fraction of Water, Y_{H_2O}	0	`calculated`
Liquid Mass Fraction of Species 1,X_1	0	0
Liquid Mass Fraction of Species 2, X_2	0	0
Liquid Mass Fraction of Water, X_{H_2O}	1	`calculated`
Gas Velocity, U_g	$(0, 0, 0)$ m/s	$(0, 0, 0)$ m/s
Liquid Velocity, U_l	$(0, 0, 0)$ m/s	`outletInlet`
Pressure, P	1×10^5 Pa	`calculated`
Modified Pressure, P_{rgh}	1×10^5 Pa	1×10^5 Pa
Gas Temperature, T_g	293.15 K	`zeroGradient`
Liquid Temperature, T_l	293.15 K	`zeroGradient`

The second case was identical to the first case, but it only incorporated one species (species 1 of the first case). The case used the same boundary conditions as the first case, but with a `zeroGradient` condition for the gas mass fraction instead of a fixed value, and the equilibrium values were calculated in a similar way. The second case used two inner correctors, ten outer correctors, and two non-orthogonal correctors in the PIMPLE loop. The species, continuity, and pressure equations were all relaxed by a factor of 0.7. The two tests were to determine that the algorithm was calculating the phase fraction equation, which was modified, and species fraction equations, which were added, properly based on the given inputs to the solver. The mesh consisted of four equally sized cells. The continuity and modifed pressure equations were relaxed by a factor of 0.7 and 0.5 respectively. The limited discretization scheme was used for all divergence terms except species, which used limitedLinear, and linear was used for all other schemes except the timestepping, which used explicit Euler. The simulation was run for 50 s at a constant time step of 0.1 s, at which time equilibrium had essentially been reached in the box.

The properties used for the calculation of the diffusion coefficient, molar mass, and mass transfer coefficient are summarized in Table 6.2. These values are fictional and do not represent real-world values. The volume addition was incorporated directly into the solution of the continuity equation to solve for the phase fraction, which is the primary difference between the spreadsheet solution and the `OpenFOAM` solution.

Table 6.2: Species properties for the stationary mass transfer algorithm verification

	Gas Viscosity [kg/s · m]	**Liquid Viscosity** [kg/s · m]	Pr_g	Pr_l	Le_g	Le_l	Sh	**M** [g/mol]	H_i	Sc
Species 1	$9e-6$	$1e-6$	0.713	2.289	100	1	2	28.97	$1.45e-2$	1000
Species 2	$9e-6$	$5e-5$	0.71	2.289	100	1	2	44.01	0.818	1000
H_2O	$2.04e-5$	$5e-5$	0.63	2.289	100	1	2	18.0153	N/A	1000

For comparison, the equilibrium concentrations and volume fractions were calculated, and a transient solution was performed in Excel.

6.1.1 Equilibrium Calculation

To set up the equilibrium calculation, the total mass and the species masses before and after were taken into account. This was because the pressure and the volume of the box were kept constant for the case. Only pure water was allowed to enter the box, to make up for the change in gas volume due to dissolution. Figure 6.1 shows the mass in the box initially and at equilibrium.

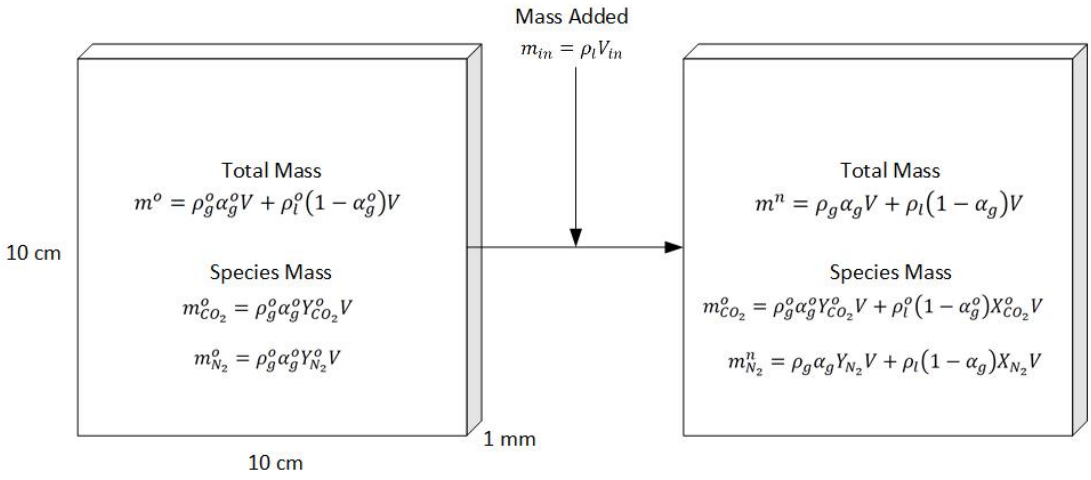

Figure 6.1: Total mass conservation in the box between the initial state (left) and at equilibrium (right).

The equilibrium calculation was a system of seven coupled equations and two extra algebraic equations. The total mass balance is,

$$\rho_l V_{in} + \rho_g^o \alpha_g^o V + \rho_l (1 - \alpha_g^o) V - (\rho_g \alpha_g V + \rho_l (1 - \alpha_g) V) = 0 \tag{6.1}$$

Where the subscript o indicates the initial value, V_{in} is the volume of pure water which entered the domain, and V is the total volume of the box. The species mass

balances are,

$$\begin{aligned} \rho_g^o \alpha_g^o V Y_2^o - \rho_g \alpha_g V Y_2 - \rho_l (1-\alpha_g) V X_2 = 0 \\ rho_g^o \alpha_g^o V Y_1^o - \rho_g \alpha_g V Y_1 - \rho_l (1-\alpha_g) V X_1 = 0 \end{aligned} \tag{6.2}$$

The Henry's Law relations are,

$$\begin{aligned} Y_1 - \frac{X_1 \rho_l}{H_1 \rho_g} = 0 \\ Y_2 - \frac{X_2 \rho_l}{H_2 \rho_g} = 0 \end{aligned} \tag{6.3}$$

The species fractions must sum to unity in both phases,

$$\begin{aligned} \sum_i Y_i - 1 = 0 \\ \sum_i X_i - 1 = 0 \end{aligned} \tag{6.4}$$

The two algebraic equations for the molar mass and the gas density were,

$$\begin{aligned} M_g = \left(\sum_i \frac{Y_i}{M_i} \right)^{-1} \\ \rho_g = \frac{PM}{RT} \end{aligned} \tag{6.5}$$

Where M [kg/mol] is the molar mass, and R $[(\mathrm{Pa} \cdot \mathrm{m}^3)/(\mathrm{mol} \cdot \mathrm{K})]$ is the ideal gas constant.

6.1.2 Transient Excel Calculation

The spreadsheet algorithm for the transient solution involved the calculation of the equations as in the order given to follow. The density was calculated from the molar mass at each time step,

$$M_g = \left(\sum_i \frac{Y_i}{M_i} \right)^{-1} \tag{6.6}$$

$$\rho_g = \frac{PM}{RT} \tag{6.7}$$

The mass transfer coefficients were calculated based on the Sherwood correlation,

$$k_m = a_i D_{i,j} Sh \tag{6.8}$$

The interfacial compositions in the gas phase were calculated using the Henry's law constants given in Table 6.2,

$$Y_i^I = \frac{\rho_g k_{m,g} Y_i + \rho_l k_{m,l} X_i}{\rho_g k_{m,l} H_i + \rho_g k_{m,g}} \tag{6.9}$$

Each gas side mass transfer component was calculated and the two were summed,

$$\frac{\partial m_g}{\partial t} = \rho_g \sum_{i=1}^{n} k_{i,m,g}(Y_i^I - Y_i) \tag{6.10}$$

The mass coming in at each time step was calculated as the difference in density between the current timestep and the last,

$$m_{in} = V(\rho_g^n \alpha_g^n - \rho_g^o \alpha_g^o)\Delta t \tag{6.11}$$

The new gas volume fractions were then calculated,

$$\alpha_g^n = \alpha_g^o + \frac{1}{\rho_g V}(\frac{\partial m_g}{\partial t}\Delta t - \frac{V_i n}{\rho_l}) \tag{6.12}$$

Finally the species fractions were calculated in the gas and liquid,

$$\begin{aligned} Y_i &= \frac{1}{V\rho_g\alpha_g}(\frac{\partial m_i}{\partial t}\Delta t + V\alpha_g^o\rho_g Y_i^o) \\ X_i &= \frac{1}{V\rho_l\alpha_l}(V\alpha_l^o\rho_l X_i^o - \frac{\partial m_i}{\partial t}\Delta t) \end{aligned} \tag{6.13}$$

6.1.3 Results

The results of the comparison between the volume fractions for the first case are shown in Figure 6.2. The Excel calculation clearly behaved correctly, with the final value being equal to the equilibrium value. It can be seen that the two transient cases obtained very similar values until around two seconds, at which point the solutions began to diverge. The discrepancy was not caused by the temporal discretization, but this case did have some problems converging in the pressure equation. The likely reason for the difference in the predictions is that the solver was fundamentally built for cases involving flow. The coupling between the phases is weakened when the majority of the interphase force terms are omitted from the momentum equations. This could cause small errors in the calculation of continuity due to incomplete convergence of

the pressure equation.

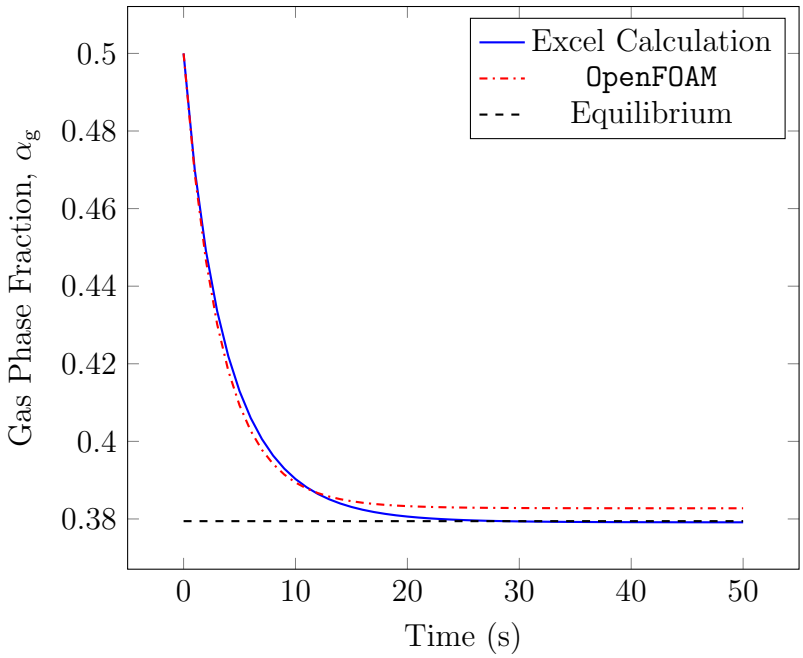

Figure 6.2: Case 1 - Change in gas phase fraction over time.

The volume fractions for the second case are given in Figure 6.3. The error at equilibrium is much smaller for the second case, at 0.016 %. Between the two cases, the temperature at the interface was closer to the initial gas temperature in the second case than in the first case. Slight variations in the temperature at the interface were not incorporated in the hand calculations, which could change the volumetric mass transfer coefficient, through the diffusion coefficient, and could contribute to the error.

The species fractions in the first case were also somewhat different between the `OpenFOAM` result and the hand calculation. In the case of species 2, the species fractions were higher than expected, and in the case of species 1, they were lower, as can be seen in Figure 6.4. This was to be expected because of the volume fraction discrepancy. The error was 2.06 % in species 1 and 4.71 % in species 2 at equilibrium. In the single species case, the gas mass fraction remained at 1.0 as was to be expected.

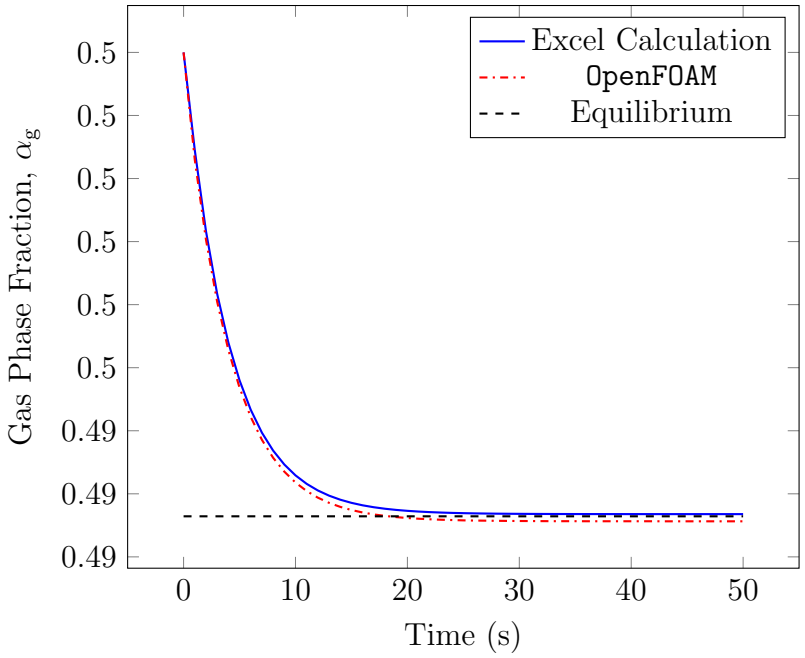

Figure 6.3: Case 2 - Change in gas phase fraction over time.

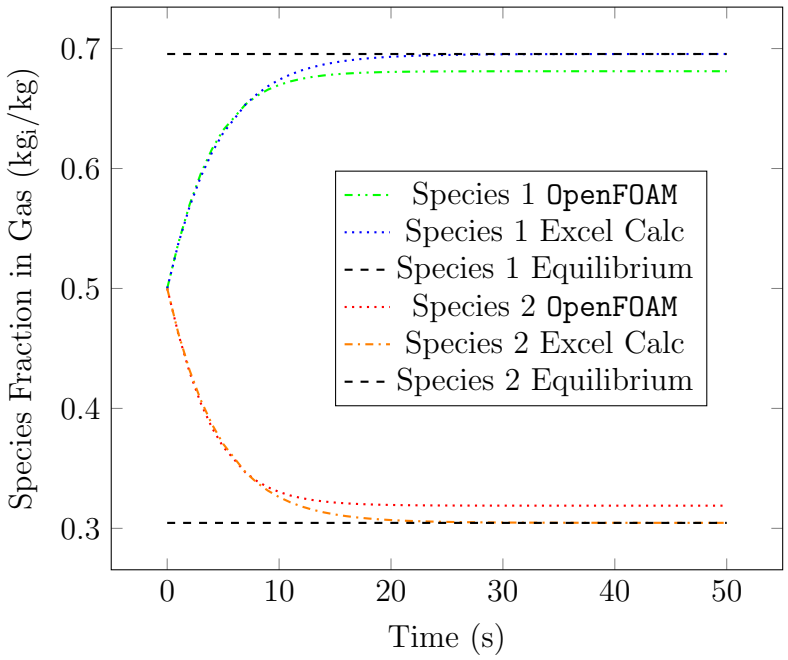

Figure 6.4: Case 1 - Change in species fractions over time.

The pressure field remained constant throughout the duration of the simulation,

but the velocity in the box was on the order of 10^{-3} at the beginning of the simulation. This could have altered the solution of the continuity equation somewhat. Since no fluid was allowed to escape the box, Henry's law should have forced the mass fractions toward the correct equilibrium value, but this did not occur.

Although the diffusive component was left out of the hand calculations and the equilibrium calculation it did not impact the result since the Schmidt numbers were set very high. This was checked by removing the diffusion term from the transport equation.

At present, it is not clear why the simulation does not yield the exact results at equilibrium. There is either too much volume in the first case, or too little volume in the second case allowed to enter through the sides, which is ultimately linked back to the substantial derivative of density. Everything is coupled such that isolating the problem is made more difficult, but it is likely to be the lack of multiphase forces applied. Additional testing must be performed in the future, but the mass transfer predictions obtained with the new `twoPhaseEulerFoam` algorithm are off by less than 5% in the mass fractions and 1% in the volume fraction, which is within a reasonable amount of error.

6.2 Application of the Algorithm to a Large-Scale Bubble Plume

The algorithm described in Chapter 2 was tested to ensure it worked as expected on a hydrodynamic case. Although it was shown in Chapter 5 that the hydrodynamics were inaccurately predicted with `twoPhaseEulerFoam`, case 1 from that chapter was used to ensure the algorithm would work on a case involving flow despite the poor prediction. The experimental study of Simiano (2005) did not include mass transfer data, but the literature does not have many studies of gas-stirred systems that include both detailed hydrodynamic and mass transfer data. Those that do often lack important details for the case setup, and so were unsuitable. This is an area for future research.

All boundary and initial conditions were kept the same as in Chapter 5, except the gas coming in through the inlet was changed to pure oxygen instead of air. The fluid properties used for oxygen can be found in Table 6.3. The mass transfer model used was that of Akita and Yoshida (1974). Mesh 1 from Case 1 of Chapter 5 was used for this study along with all the same sub-models and tuning parameters. It was assumed that aqueous properties for all species were the same and equal to that of water (dilute) as given in 4.2.

Table 6.3: Gas phase species properties

Species	Molecular Weight	Viscosity	Specific Heat Capacity	Prandtl Number	Schmidt Number
O_2	32 g/mol	2×10^{-5} Pa · s	918 J/kg · K	0.82233	0.8

Since no experimental data was available, the only way to verify that the algorithm was calculating correctly was by calculating both sides of the species transport equation for the liquid side and ensuring they gave the same result and mass was conserved. The species transport equation is,

$$\frac{\partial \alpha_l \rho_l X_{O_2}}{\partial t} + \nabla \cdot (\alpha_{f,l} \rho_{f,l} \vec{\phi_l} X_{O_2}) - \nabla^2 \left(\frac{\alpha_{f,l} \nu_{f,l} \rho_{f,l} Y_{O_2}}{Sc_{f,l}} \right) - \nabla^2 \left(\frac{\alpha_{f,l} \nu^t_{f,l} \rho_{f,l} Y_k}{Sc^t_{f,l}} \right) = \frac{\partial m_{O_2,l}}{\partial t} \tag{6.14}$$

Since the only term which adds mass to the liquid volume is the source term, since no liquid was allowed to escape, the mass balance reduces to,

$$\iiint_V \alpha_l \rho_l X_{O_2} dV = \int_0^t \left(\iiint_V \frac{\partial m_{O_2,l}}{\partial t} dV \right) dt \tag{6.15}$$

The integral of the total mass in the liquid at any time in the system with volume (LHS of Equation 6.15) can be calculated from the printed fields as,

$$m^t_{O_2} = \sum_{cells} \alpha_l \rho_l X_{O_2} \Delta V_{cell} \tag{6.16}$$

The total mass transferred to the liquid must be equal to the integral of the source term over time. Using the printed fields from the simulation, the source term integration (RHS of Equation 6.15) was calculated as,

$$m^t_{O_2} = \int_0^t \left(\iiint_V \frac{\partial m_{O_2,l}}{\partial t} dV \right) dt = \int_0^t \left(\iiint_V \rho_l k_{m,l} (X^I_{O_2} - X_{O_2}) dV \right) dt \tag{6.17}$$

Where ρ_L was approximated to be 1000 kg/m^3 throughout. The quantity was multiplied by the time-step and summed for each new time,

$$m^t_{O_2} = \sum_0^t \sum_{cells} \rho_l k_{m,l} (\frac{\rho_g H_{O_2}}{\rho_l} - X_{O_2}) \Delta V_{cell} \Delta t \tag{6.18}$$

The saturation value, $X^I_{O_2}$ was calculated from Henry's law and used an approximate gas density of 1.4 kg/m^3.

The source term was also printed directly from the code. The results of the two

calculations and the printed source term are given in Figure 6.5. The left hand side of the mass balance (calculated mass) and the printed source term from the code are almost identical. The small differences between the three lines is most likely due to the rough integrations of the two quantities.

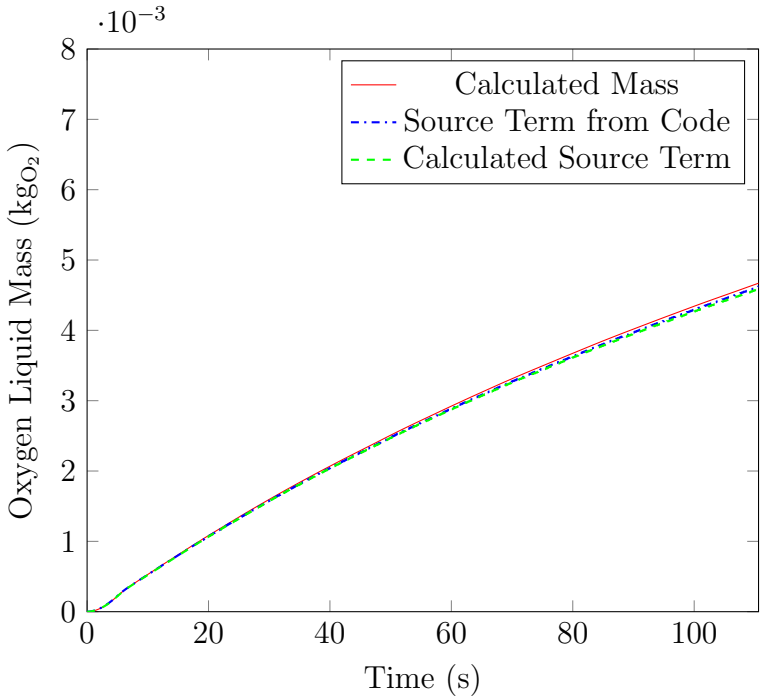

Figure 6.5: Mass of aqueous oxygen in the vessel over time.

The mass transfer algorithm described in Chapter 2 conserves mass for the case in which there is fluid flow. This verifies that the additions to the `twoPhaseEulerFoam` solver are behaving as expected.

Chapter 7

Conclusion

In Chapter 4, five turbulence models were compared to each other by simulating the model ladle of Sheng and Irons (1993). Sheng and Irons (1993) had tuned the Simonin and Viollet (1988) turbulence model specifically for their experimental data, but the result from the present study, which implemented the same model, was that the liquid axial velocity and the turbulent kinetic energy were underpredicted by a large margin. The four other turbulence models which were compared have been used throughout the literature for bubbly flow conditions, yet none of their predictions were close to the experimental data in every property. The mesh resolution and the bubble size estimate were tested in separate studies, but it was concluded that the mesh size and bubble size which had been chosen in the comparison study would have been reasonable. The tuning parameters which were used by Sheng and Irons (1993) were not given, but in a later study of the same ladle by Lou and Zhu (2013b), they were. They used a different turbulence model and turbulent dispersion force model than the current study, but otherwise the parameters were the same. The results between their model and the current work were different. The effect of using wall functions on the cases of Chapter 4 was not studied, but may improve the result based on the study of Chapter 5.

The turbulent dispersion force interactions in conjunction with the turbulence model in the present Euler-Euler model requires future investigation. The two models necessarily have a feedback effect on each other, but the reaction of the flow to any change in the turbulent dispersion force does not seem to be something that can be known *a priori*. The tuning between the turbulence model and the turbulent dispersion force, in addition to the tuning of the lift force and the bubble size, that is required could be one of the greatest impediments to the application of the two-fluid model to the large-scale gas well blowout.

At the bubble size for the ladle simulations, the drag coefficient should have been approximately constant for the assumption of a spherical bubble, and the choice of drag model would probably not have been of great importance, as the constant value only varies very slightly between models. The turbulent dispersion model of

Davidson (1990) relies on the drag force, unlike that of Lopez de Bertodano (1998), which could potentially further couple the momentum equation to the other phase in a superior way. This was tested in Chapter 5, where both were compared in the study of the large-scale bubble plume. The turbulent dispersion model of Davidson (1990) seemed to give a better hydrodynamic prediction at the height of 0.6 m where it was measured.

The study of Dhotre and Smith (2007), who tuned the sub-models to match the experimental data of Simiano (2005) was used in Chapter 5 to attempt to replicate their result, using the exact same tuning parameters. The result obtained in the current research gave a good prediction to the Dhotre and Smith (2007) simulation and experimental results, but only after significant tuning. The boundary conditions of the study of Dhotre and Smith (2007) were not provided, but they simulated the free surface unlike in the current work. As with the model ladle simulations of Chapter 4, including the free surface in the modeled domain did not give satisfactory results with `twoPhaseEulerFoam`. Based on the result of the current study, changing the phase fraction at the inlet had a large effect on the velocity vectors, which is a contrary result to that of Dhotre and Smith (2007). The application of wall functions, originally conceived for single-phase systems, provided what appears to have been a more physically realizable solution near the inlet. In general, more experimental and modeling studies are required to give more guidance for proper tuning of the two-fluid model in unconfined bubbly flow cases. This would potentially provide a baseline tuning strategy for extending the two-fluid model to more complicated scenarios.

The result of the first case of Chapter 5 was considered suitable enough to attempt to apply the IATE model to a second experimental study of Simiano (2005), with the same tuning parameters selected. The phase fraction chosen for the inlet gave a recirculation pattern near the bottom of the domain which was not unreasonable. It was shown that the IATE model did not behave as well as it potentially could have due to the poor hydrodynamic prediction. For this reason a really rigorous analysis of the IATE model's effectiveness could not be done in the current study.

Two different turbulent dispersion models were implemented to determine whether it was the parameter which was responsible for the inaccurate hydrodynamic prediction. Using the model of Lopez de Bertodano (1998) instead of the model of Davidson (1990) gave a worse prediction of the hydrodynamics and, as a result, the IATE model. Changing the turbulent dispersion model coefficient did not alter the results significantly, which indicates that the simulation had more sensitivity to the Simonin and Viollet (1988) turbulence model prediction for the turbulent kinetic energy than the

turbulent dispersion model.

To evaluate what the initial bubble size should be for the IATE model, five separate initial bubble diameters were implemented and simulated. None of the initial bubble diameters resulted in a good prediction for the IATE model or the hydrodynamics. It must be concluded that the IATE model could not be evaluated properly in the current study due to the hydrodynamic results which were obtained. Further study in this area is necessary, as the IATE model does seem like a promising model for bubble plumes because of the direct solution for the interfacial area concentration instead of the bubble diameter, as in other models such as MUSIG. The interfacial area concentration prediction is very important for the heat transfer and mass transfer model predictions, and may be a simpler way to determine the bubble size.

The top boundary of the simulated model ladle of Sheng and Irons (1993) was the effective free surface, as the free surface was not included in the current simulations. The boundary conditions which were applied at the top may not have been completely optimized, but created the most realizable liquid circulation. The pressure condition at the inlet that should be specified is also not entirely clear, but changing it to any other condition type gave unrealistic results for the phase fraction spread and velocity vectors. This is an area that should be investigated in more detail in future work.

The algorithm adjustments which were made for incorporating mass transfer into the base solver worked well for the verification cases in Chapter 6. The algorithm was applied to a no-flow case and gave a maximum error of 5% in the phase fraction and less than 1% in the species fractions when compared to hand calculations. When applied to a flow case, it was confirmed that mass was conserved. With the appropriate hydrodynamic prediction, a prediction of the total dissolved mass in the large-scale gas well blowout scenario would be possible with the additions made in this work. The detailed validation of the mass transfer model itself should be performed in a future work.

Upon reviewing the results of the numerical studies, it is clear that the hydrodynamic prediction obtained by `twoPhaseEulerFoam` is not accurate without significant fine-tuning for the large-scale bubble plume applications in this work. The mesh, boundary conditions, force models, initial bubble size, and model constants must all work in tandem to give a good prediction, but they cannot be optimized if there is no experimental data available to compare the prediction to, such as in the large-scale gas well blowout. Application of the two-fluid model to a bubble plume of a certain scale, using optimized parameters from a study of a different scale, could result in predictions not representative of physical reality. Further work should also be done

to investigate the scaling behaviour of this method for unconfined bubbly flows.

Bibliography

T. Acher. *A Moments Model for the Numerical Simulation of Bubble Column Flows*. PhD thesis, Technische Universität München Institut für Energietechnik, 2015.

K. Akita and F. Yoshida. Bubble size, interfacial area, and liquid-phase mass transfer coefficient in bubble columns. *Industrial & Engineering Chemistry Process Design and Development*, 13(1):84–91, 1974.

A. Behzadi, R. I. Issa, and H. Rusche. Modelling of dispersed bubble and droplet flow at high phase fractions. *Chemical Engineering Science*, 59(4):759–770, 2004.

J. Boussinesq. *Essai sur la Théorie des Eaux Courantes*. Imprimerie Nationale, 1877.

C. H. S. J. Chou. Concise international chemical assessment document 53, 2003.

R. Clift, J. R. Grace, and M. E. Weber. *Bubbles, Drops, and Particles*. Academic Press, 1978. ISBN 012176950X.

T. L. Cook and F. H. Harlow. Virtual mass in multiphase flow. *International journal of multiphase flow*, 10(6):691–696, 1984.

P. D. Coppock and G. T. Meiklejohn. The behavior of gas bubbles in relation to mass transfer. *Trans. Inst. Chem. Eng*, 29(1):75–86, 1951.

J. M. Coulson, J. F. Richardson, J. R. Backhurst, and J. H. Harker. Fluid flow, heat transfer and mass transfer. *Filtration & Separation*, 33(2):102, 1996.

L. K. Dasanayaka and P. D. Yapa. Role of plume dynamics phase in a deepwater oil and gas release model. *Journal of Hydro-Environmenalt Research*, 2(4):243–253, 2009.

L. Davidson. Large-eddy simulation: A dynamic one-equation sub-grid model for three-dimensional recirculating flow. In *11th International Symposium on Turbulent Shear Flow, Grenoble, France*, volume 3, pages 26–1, 1997.

M. R. Davidson. Numerical calculations of two-phase flow in a liquid bath with bottom gas injection: the central plume. *Applied mathematical modelling*, 14(2): 67–76, 1990.

N. G. Deen, T. Solberg, and B. H. Hjertager. Large eddy simulation of the gas–liquid flow in a square cross-sectioned bubble column. *Chemical Engineering Science*, 56 (21):6341–6349, 2001.

M. T. Dhotre and B. L. Smith. CFD simulation of large-scale bubble plumes: comparisons against experiments. *Chemical Engineering Science*, 62(23):6615–6630, 2007.

M. T. Dhotre, B. Niceno, B. L. Smith, and M. Simiano. Large-eddy simulation (les) of the large scale bubble plume. *Chemical Engineering Science*, 64(11):2692–2704, 2009.

M. E. Díaz, A. Iranzo, D. Cuadra, R. Barbero, F. J. Montes, and M. A. Galán. Numerical simulation of the gas–liquid flow in a laboratory scale bubble column: influence of bubble size distribution and non-drag forces. *Chemical Engineering Journal*, 139(2):363–379, 2008.

D. Drew, L. Cheng, and R. T. Lahey. The analysis of virtual mass effects in two-phase flow. *International Journal of Multiphase Flow*, 5(4):233–242, 1979.

D. A. Drew. A turbulent dispersion model for particles or bubbles. *Journal of Engineering Mathematics*, 41(2):259–274, 2001.

T. Frank, P. J. Zwart, J. Shi, E. Krepper, D. Lucas, and U. Rohde. Inhomogeneous MUSIG model-a population balance approach for polydispersed bubbly flows. In *International Conference-Nuclear Energy for New Europe, Bled, Slovenia*, 2005.

N. Frössling. Über die verdunstung fallender tropfen. *Gerlands Beiträge zur Geophysik*, 52:170–215, 1938.

M. Germano, U. Piomelli, P. Moin, and W. H. Cabot. A dynamic subgrid-scale eddy viscosity model. *Physics of Fluids A: Fluid Dynamics*, 3(7):1760–1765, 1991.

D. Gidaspow. Modeling of two phase flow. In *Heat transfer, 1974. Vol. 7*. International Heat Transfer Conference, 1974.

A. D. Gosman, C. Lekakou, S. Politis, R. I. Issa, and M. K. Looney. Multidimensional modeling of turbulent two-phase flows in stirred vessels. *AIChE Journal*, 38(12): 1946–1956, 1992.

R. M. Griffith. Mass transfer from drops and bubbles. *Chemical Engineering Science*, 12(3):198–213, 1960.

R. Hansen. *Computational and experimental study of bubble size in bubble columns*. PhD thesis, Aalborg University, 2009.

A. Harten. High resolution schemes for hyperbolic conservation laws. *Journal of computational physics*, 49(3):357–393, 1983.

M. R. Hestenes and E. Stiefel. Methods of conjugate gradients for solving linear systems. *Journal of Research of the National Bureau of Standards*, 49(1), 1952.

T. Hibiki and M. Ishii. Lift force in bubbly flow systems. *Chemical Engineering Science*, 62(22):6457–6474, 2007.

J. O. Hinze. Momentum and mechanical-energy balance equations for a flowing homogeneous suspension with slip between the two phases. *Applied Scientific Research, Section A*, 11(1):33–46, 1963.

E. O. Hoefele and J. K. Brimacombe. Flow regimes in submerged gas injection. *Metallurgical and Materials Transactions B*, 10(4):631–648, 1979.

G. A. Hughmark. Holdup and mass transfer in bubble columns. *Industrial & Engineering Chemistry Process Design and Development*, 6(2):218–220, 1967.

M. Ishii and T. Hibiki. *Thermo-Fluid Dynamics of Two-Phase Flow*. SpringerLink : Bücher. Springer New York, 2010. ISBN 9781441979858.

M. Ishii and S. Kim. Micro four-sensor probe measurement of interfacial area transport for bubbly flow in round pipes. *Nuclear Engineering and Design*, 205(12):123 – 131, 2001. ISSN 0029-5493.

M. Ishii and S. Kim. Development of one-group and two-group interfacial area transport equation. *Nuclear science and engineering*, 146(3):257–273, 2004.

M. Ishii and N. Zuber. Drag coefficient and relative velocity in bubbly, droplet or particulate flows. *AIChE Journal*, 25(5):843–855, 1979.

M. Ishii, S. Kim, and J. Kelly. Development of interfacial area transport equation. *Nuclear Engineering and Technology*, 37(6):525, 2005.

R. I. Issa. Solution of the explicitly discretised fluid flow equations by operator-splitting. *Journal of Computational Physics*, 62:40–65, 1985.

R. I. Issa. Prediction of turbulent, stratified, two-phase flow in inclined pipes and channels. *International Journal of Multiphase Flow*, 14(2):141–154, 1988.

H. Jasak. *Error analysis and estimation for finite volume method with applications to fluid flow*. PhD thesis, University of London, 1996.

H. Jasak and H. G. Weller. Interface tracking capabilities of the inter-gamma differencing scheme. *Department of Mechanical Engineering, Imperial College of Science, Technology and Medicine*, 1995.

Ø. Johansen. Deepblow–a lagrangian plume model for deep water blowouts. *Spill Science & Technology Bulletin*, 6(2):103–111, 2000.

Ø. Johansen. Development and verification of deep-water blowout models. *Marine Pollution Bulletin*, 47(9):360–368, 2003.

G. Kocamustafaogullari and M. Ishii. Foundation of the interfacial area transport equation and its closure relations. *International Journal of Heat and Mass Transfer*, 38(3):481–493, 1995.

N. I. Kolev. *Multiphase flow dynamics 2: Thermal and mechanical interactions*, volume 2. Springer Science & Business Media, 2007.

N. I. Kolev. *Drag, lift, and virtual mass forces*, pages 31–85. Springer Berlin Heidelberg, Berlin, Heidelberg, 2012. ISBN 978-3-642-20598-9.

A. N. Kolmogorov. The local structure of turbulence in incompressible viscous fluid for very large reynolds numbers. *Dokl. Akad. Nauk SSSR*, 30(4):299–303, 1941.

R. T. Lahey. The simulation of multidimensional multiphase flows. *Nuclear Engineering and Design*, 235(10):1043–1060, 2005.

D. Lakehal, B. L. Smith, and M. Milelli. Large-eddy simulation of bubbly turbulent shear flows. *Journal of Turbulence*, 3(25):1–21, 2002.

B. E. Launder and D. B. Spalding. The numerical computation of turbulent flows. *Computer methods in applied mechanics and engineering*, 3(2):269–289, 1974.

B. E. Launder, G. Jr. Reece, and W. Rodi. Progress in the development of a reynolds-stress turbulence closure. *Journal of fluid mechanics*, 68(03):537–566, 1975.

J. H. W. Lee and V. Cheung. Generalized lagrangian model for buoyant jets in current. *Journal of environmental engineering*, 116(6):1085–1106, 1990.

S. L. Lee, R. T. Lahey, and O. C. Jones. The prediction of two-phase turbulence and phase distribution phenomena using a k-κ model. *Japanese Journal of Multiphase Flow*, 3(4):335–368, 1989.

D. Legendre and J. Magnaudet. The lift force on a spherical bubble in a viscous linear shear flow. *Journal of Fluid Mechanics*, 368:81–126, 1998.

D. Legendre, J. Magnaudet, and G. Mougin. Hydrodynamic interactions between two spherical bubbles rising side by side in a viscous liquid. *Journal of Fluid Mechanics*, 497:133–166, 2003.

R. J. LeVeque. *Finite volume methods for hyperbolic problems*, volume 31. Cambridge university press, 2002.

S. Lo. Application of the MUSIG model to bubbly flows. *AEAT-1096, AEA Technology*, 1996.

M. Lopez de Bertodano. Two fluid model for two-phase turbulent jets. *Nuclear Engineering and Design*, 179(1):65–74, 1998.

M. A. Lopez de Bertodano. *Turbulent Bubbly Two-phase Flow in a Triangular Duct*. PhD thesis, Rensselaer Polytechnic Institute, 1992.

W. Lou and M. Zhu. Numerical simulations of inclusion behavior in gas-stirred ladles. *Metallurgical and Materials Transactions B*, 44(3):762–782, June 2013a. doi: 10.1007/s11663-013-9802-3.

W. Lou and M. Zhu. Numerical simulation of gas and liquid two-phase flow in gas-stirred systems based on Euler-Euler approach. *Metallurgical and Materials Transactions*, 44(5):1251, 2013b.

D. Lucas and A. Tomiyama. On the role of the lateral lift force in poly-dispersed bubbly flows. *International Journal of Multiphase Flow*, 37(9):1178–1190, 2011.

D. L. Marchisio and R. O. Fox. Solution of population balance equations using the direct quadrature method of moments. *Journal of Aerosol Science*, 36(1):43–73, 2005.

D. L. Marchisio and R. O. Fox. *Computational models for polydisperse particulate and multiphase systems*. Cambridge University Press, 2013.

M. Milelli, B. L. Smith, and D. Lakehal. Large-eddy simulation of turbulent shear flows laden with bubbles. In *Direct and Large-Eddy Simulation IV*, pages 461–470. Springer, 2001a.

M. Milelli, B. L. Smith, and D. Lakehal. Subgrid-scale dynamic modelling in les of turbulent bubbly flows. In *TSFP DIGITAL LIBRARY ONLINE*. Begel House Inc., 2001b.

P. Moilanen, M. Laakkonen, O. Visuri, V. Alopaeus, and J. Aittamaa. Modelling mass transfer in an aerated 0.2 m 3 vessel agitated by rushton, phasejet and combijet impellers. *Chemical Engineering Journal*, 142(1):95–108, 2008.

F. Moukalled, L. Mangani, and M. Darwish. *The Finite Volume Method in Computational Fluid Dynamics*. Springer International, 2016.

B. Ničeno, M. Boucker, and B. L. Smith. Euler-Euler large eddy simulation of a square cross-sectional bubble column using the neptune CFD code. *Science and Technology of Nuclear Installations*, 2009, 2008a.

B. Ničeno, M. T. Dhotre, and N. G. Deen. One-equation sub-grid scale (SGS) modelling for Euler–Euler large eddy simulation (EELES) of dispersed bubbly flow. *Chemical Engineering Science*, 63(15):3923–3931, 2008b.

J. E. Olsen and P. Skjetne. Current understanding of subsea gas release: A review. *The Canadian Journal of Chemical Engineering*, 94(2):209–219, 2016a.

J. E. Olsen and P. Skjetne. Modelling of underwater bubble plumes and gas dissolution with an Eulerian-Lagrangian CFD model. *Applied Ocean Research*, 59:193–200, 2016b.

OpenCFD Ltd. OpenFOAM, 2017. URL `http://www.openfoam.com/`.

Q. Q. Pan, J. E. Olsen, J. T. Johansen, M. Reed, and L. R. Sætran. CFD study of surface flow and gas dispersion from a subsea gas release. In *ASME 2014 33rd International Conference on Ocean, Offshore and Arctic Engineering*, pages V007T12A032–V007T12A032. American Society of Mechanical Engineers, 2014.

S.V. Patankar. *Numerical Heat Transfer and Fluid Flow*. Taylor and Francis, 1980.

D. Pfleger and S. Becker. Modelling and simulation of the dynamic flow behaviour in a bubble column. *Chemical Engineering Science*, 56(4):1737–1747, 2001.

Andrea Prosperetti and Grétar Tryggvason. *Computational methods for multiphase flow*. Cambridge university press, 2009.

J. D. Ramshaw and J. A. Trapp. Characteristics, stability, and short-wavelength phenomena in two-phase flow equation systems. *Nuclear Science and Engineering*, 66(1):93–102, 1978.

C. M. Rhie and W. L. Chow. Numerical study of the turbulent flow past an airfoil with trailing edge separation. *American Institute of Aeronautics and Astronautics Journal*, 21(11):1525–1532, 1983.

R. S. Rivlin. The relation between the flow of non-Newtonian fluids and turbulent Newtonian fluids. In *Collected Papers of RS Rivlin*, pages 1941–1944. Springer, 1997.

W. Rodi. *Turbulence models and their application in hydraulics*. IAHR, Monograph Series, 3 edition, 1993.

H. Rusche. *Computational fluid dynamics of dispersed two-phase flows at high phase fractions*. PhD thesis, University of London, 2002.

R. Sander. Compilation of henry's law constants for inorganic and organic species of potential importance in environmental chemistry, 1999.

M. Sano and K. Mori. Bubble formation from single nozzles in liquid metals. *Transactions of the Japan Institute of Metals*, 17(6):344–352, 1976.

Y. Sato and K. Sekoguchi. Liquid velocity distribution in two-phase bubble flow. *International Journal of Multiphase Flow*, 2(1):79–95, 1975.

L. Schiller and A. Naumann. Über die grundlegenden berechnungen bei der schwerkraftaufbereitung. *Zeitchrift des Vereines deutcsher Ingenieure*, pages 318–320, 1933.

F. G. Schmitt. About Boussinesq's turbulent viscosity hypothesis: historical remarks and a direct evaluation of its validity. *Comptes Rendus Mécanique*, 335(9-10): 617–627, 2007.

B. Selma, R. Bannari, and P. Proulx. Simulation of bubbly flows: Comparison between direct quadrature method of moments (DQMOM) and method of classes (CM). *Chemical Engineering Science*, 65(6):1925–1941, 2010.

Y. Y. Sheng and G. A. Irons. Measurement and modeling of turbulence in the gas/liquid two-phase zone during gas injection. *Metallurgical and Materials Transactions B*, 24(4):695–705, 1993.

M. Simiano. *Experimental investigation of large-scale three dimensional bubble plume dynamics*. PhD thesis, ETH Zürich, 2005.

O. Simonin and P. Viollet. On the computation of turbulent two-phase flows in the Eulerian formulation. *EUROMECH*, page 234, 1988.

J. Smagorinsky. General circulation experiments with the primitive equations: I. the basic experiment. *Monthly weather review*, 91(3):99–164, 1963.

T. R. Smith, J. P. Schlegel, T. Hibiki, and M. Ishii. Two-phase flow structure in large diameter pipes. *International Journal of Heat and Fluid Flow*, 33(1):156–167, 2012a.

T. R. Smith, J.P. Schlegel, T. Hibiki, and M. Ishii. Mechanistic modeling of interfacial area transport in large diameter pipes. *International Journal of Multiphase Flow*, 47:1 – 16, 2012b.

S. A. Socolofsky, E. Eric. Adams, C. B. Paris, and D. Yang. How do oil, gas, and water interact near a subsea blowout? *Oceanography*, 29(3):64–75, 2016.

A. Sokolichin, G. Eigenberger, and A. Lapin. Simulation of buoyancy driven bubbly flow: established simplifications and open questions. *AIChE Journal*, 50(1):24–45, 2004.

S. L. Soo. *Fluid dynamics of multiphase systems*. Blaisdell Publishing Company Waltham, Massachusetts, 1967.

C. G. Speziale. On nonlinear k-l and k-ϵ models of turbulence. *Journal of Fluid Mechanics*, 178:459–475, 1987.

C. G. Speziale, S. Sarkar, and T. Gatski. Modeling the rapid pressure–strain correlation of turbulence. *Phys. Fluids*, 84:85–95, 1990.

P. C. Sridher. *Validating sub-sea gas pipeline leaks discharge model for Arabian sea conditions*. PhD thesis, University of Petroleum & Energy Studies, 2012.

X. Sun, S. Kim, M. Ishii, and S. G. Beus. Modeling of bubble coalescence and disintegration in confined upward two-phase flow. *Nuclear Engineering and Design*, 230(1):3–26, 2004.

D. Tian, C. Yan, and L. Sun. Evaluation of interfacial area transport equation in vertical bubbly two-phase flow in large diameter pipes. *Annals of Nuclear Energy*, 75:199–209, 2015.

A. Tomiyama, I. Kataoka, I. Zun, and T. Sakaguchi. Drag coefficients of single bubbles under normal and micro gravity conditions. *JSME International Journal Series B Fluids and Thermal Engineering*, 41(2):472–479, 1998.

A. Tomiyama, G. P. Celata, S. Hosokawa, and S. Yoshida. Terminal velocity of single bubbles in surface tension force dominant regime. *International Journal of Multiphase Flow*, 28(9):1497–1519, 2002a.

A. Tomiyama, H. Tamai, I. Ž, and S. Hosokawa. Transverse migration of single bubbles in simple shear flows. *Chemical Engineering Science*, 57(11):1849–1858, 2002b.

A. A. Troshko and Y. A. Hassan. A two-equation turbulence model of turbulent bubbly flows. *International Journal of Multiphase Flow*, 27(11):1965–2000, 2001.

B. Van Leer. Towards the ultimate conservative difference scheme. II. monotonicity and conservation combined in a second-order scheme. *Journal of computational physics*, 14(4):361–370, 1974.

G. B. Wallis. *One-dimensional two-phase flow*. McGraw-Hill, 1969.

Q. Wu, S. Kim, M. Ishii, and S. G. Beus. One-group interfacial area transport in vertical bubbly flow. *International Journal of Heat and Mass Transfer*, 41(8-9): 1103–1112, 1998.

P. D. Yapa and Z. Li. Simulation of oil spills from underwater accidents I: Model development. *Journal of Hydraulic Research*, 35(5):673–688, 1997.

P. D. Yapa, L. Zheng, and K. Nakata. Modeling underwater oil/gas jets and plumes. *Journal of Hydraulic Engineering*, 125(5):481–491, 1999.

D. Zhang. *Eulerian modeling of reactive gas-liquid flow in a bubble column*. PhD thesis, University of Twente, 2007.

D. Zhang, N. G. Deen, and J. A. M. Kuipers. Numerical simulation of the dynamic flow behavior in a bubble column: A study of closures for turbulence and interface forces. *Chemical Engineering Science*, 61(23):7593–7608, 2006.

L. Zhao, M. C. Boufadel, K. Lee, T. King, N. Loney, and X. Geng. Evolution of bubble size distribution from gas blowout in shallow water. *Journal of Geophysical Research: Oceans*, 121(3):1573–1599, 2016.

Appendix A

Electronic Supplement

The electronic supplement to this document is available on DalSpace and contains the modified `twoPhaseEulerFoam` solver which was used in this work.